

THE EVOLUTION OF CATAclysmic VARIABLES AS REVEALED BY THEIR DONOR STARS

CHRISTIAN KNIGGE

School of Physics & Astronomy, University of Southampton, Southampton SO17 1BJ, UK

ISABELLE BARAFFE

School of Physics, University of Exeter, Exeter EX4 4QL, UK

AND

JOSEPH PATTERSON

Department of Astronomy, Columbia University, 550 West 120th Street, New York, NY 10027, USA
Submitted to ApJ Supplement Series

ABSTRACT

We present an attempt to reconstruct the complete evolutionary path followed by cataclysmic variables (CVs), based on the observed mass-radius relationship of their donor stars. Along the way, we update the semi-empirical CV donor sequence presented in Knigge (2006), present a comprehensive review of the connection between CV evolution and the secondary stars in these system, and reexamine most of the commonly used magnetic braking (MB) recipes, finding that even conceptually similar ones can differ greatly in both magnitude and functional form.

The great advantage of using donor radii to infer mass-transfer and angular-momentum-loss (AML) rates is that they sample the longest accessible time scales and are most likely to represent the true secular (evolutionary average) rates. We show explicitly that if CVs exhibit long-term mass-transfer-rate fluctuations, as is often assumed, the expected variability time scales are so long that other tracers of the mass-transfer rate – including white dwarf (WD) temperatures – become unreliable.

We carefully explore how much of the radius difference between CV donors and models of isolated main-sequence stars may be due to mechanisms other than mass loss. The tidal and rotational deformation of Roche-lobe-filling stars produces $\simeq 4.5\%$ radius inflation below the period gap, and $\simeq 7.9\%$ above. A comparison of stellar models to mass-radius data for non-interacting stars suggests a real offset of $\simeq 1.5\%$ for fully convective stars (i.e. donors below the gap) and $\simeq 4.9\%$ for partially radiative ones (donors above the gap). We also show that donor bloating due to irradiation is probably smaller than, and at most comparable to, these effects.

After calibrating our models to account for these issues, we fit self-consistent evolution sequences to our compilation of donor masses and radii. In the standard model of CV evolution, AMLs below the period gap are assumed to be driven solely by gravitational radiation (GR), while AMLs above the gap are usually described by a MB law first suggested by Rappaport, Verbunt & Joss (1983). We adopt simple scaled versions of these AML recipes and find that these are able to match the data quite well. The optimal scaling factors turn out to be $f_{GR} = 2.47 \pm 0.22$ below the gap and $f_{MB} = 0.66 \pm 0.05$ above (the errors here are purely statistical, and the standard model corresponds to $f_{GR} = f_{MB} = 1$). This revised model describes the mass-radius data significantly better than the standard model.

Some of the most important implications and applications of our results are as follows. (1) The revised evolution sequence yields correct locations for the minimum period and the upper edge of the period gap; the standard sequence does not. (2) The observed spectral types of CV donors are compatible with both standard and revised models. (3) A direct comparison of predicted and observed WD temperatures suggests an even higher value for f_{GR} , but this comparison is sensitive to the assumed mean WD mass and the possible existence of mass-transfer-rate fluctuations. (4) The predicted absolute magnitudes of donor stars in the near-infrared form a lower envelope around the observed absolute magnitudes for systems with parallax distances. This is true for all of our sequences, so any of them can be used to set firm lower limits on (or obtain rough estimates of) the distance toward CVs based only on P_{orb} and single-epoch near-IR measurements. (5) Both standard and revised sequences predict that short-period CVs should be susceptible to dwarf nova (DN) eruptions, consistent with observations. However, both sequences also predict that the fraction of DNe among long-period CVs should decline with P_{orb} above the period gap. Observations suggest the opposite behaviour, and we discuss the possible explanations for this discrepancy. (6) Approximate orbital period distributions constructed from our evolution sequences suggest that the ratio of long-period CVs to short-period, pre-bounce CV is about $3\times$ higher for the revised sequence than the standard one. This may resolve a long-standing problem in CV evolution.

Tables describing our donor and evolution sequences are provided in electronically readable form.

Subject headings: novae, cataclysmic variables, stars: fundamental parameters

TABLE OF CONTENT

1	Introduction	3
2	CV Evolution And Donor Stars	4
2.1	Angular Momentum Loss and Mass Transfer in CVs	4
2.2	The Response of a Low-Mass Star to Mass Loss	5
2.2.1	Basic Physics	5
2.2.2	The Radius Adjustment Time Scale: Sensitivity to Mass-Loss History	5
2.2.3	M_2 - L_2 and M_2 - $T_{eff,2}$ Relations	7
2.3	The Connection between CV Donors and Evolution	7
2.3.1	Magnetic Braking	7
2.3.2	The Period Gap	9
2.3.3	The Period Minimum and the Period Spike	9
3	The Semi-Empirical Donor Sequence Revisited	10
4	Reconstructing Secular Evolution in the Presence of \dot{M}_2 Fluctuations	13
4.1	The Historical Case for Long-Term \dot{M}_2 Fluctuations	14
4.2	Physical Causes of Long-Term \dot{M}_2 Fluctuations	14
4.2.1	Varying R_2 : Irradiation-Driven Mass-Transfer Rate Fluctuations	14
4.2.2	Varying R_L : Nova-Induced Cycles and Hibernation	15
4.3	Averaging Time Scales Associated with Observational Tracers of \dot{M}_2	16
4.3.1	Accretion Light	16
4.3.2	White Dwarf Temperatures	16
4.3.3	Donor Radii	16
4.4	A Direct Comparison of Variability and Observational Averaging Time Scales	16
4.4.1	The Observational Case for Long-Term \dot{M}_2 Fluctuations: An Update	17
5	CV Evolution From Donor Properties	18
5.1	Overview of the Method	18
5.2	Apparent Donor Bloating Unrelated to Mass Loss	18
5.2.1	Larger-Than-Expected Radii in Non-Interacting Low-Mass Stars	18
5.2.2	Tidal and Rotational Deformation	20
5.2.3	Irradiation	22
5.3	Settling on the Form of J_{sys}	23
5.4	Constructing the Final Track	23
6	A Complete, Semi-Empirical, Donor-Based CV Evolution Track	24
6.1	Physical and Photometric Properties	26
6.2	The Locations of Period Bounce and Period Gap	28
6.3	Donor Spectral Types	32
6.4	White Dwarf Temperatures	33
7	Implications and Applications	35
7.1	Donor-Based Photometric Parallax	35
7.2	Disk (In)stability: The Parameter Space of Dwarf Novae	37
7.2.1	Motivation and Observational Background	37
7.2.2	Critical vs. Secular Mass-Transfer Rates	37
7.2.3	Reconciling Theory and Observation	37
7.2.4	Coda: The Surprising Decline of Dwarf Novae in the Period Gap	40
7.3	Orbital Period Distributions	40
7.3.1	Motivation and Construction	40
7.3.2	Basic Results	40
7.3.3	Normalization and Space Densities	42
7.3.4	The Shapes of the Period Distribution and the Spike at the Lower Gap Edge	42
7.3.5	The Spectre of Mass-Transfer-Rate Fluctuations	43
8	Discussion	43
8.1	A Comparison to Littlefair et al. (2008)	43
8.2	A Comparison to Sirotkin & Kim (2010)	44
8.3	Sensitivity to Non-Mass-Loss-Related Donor Bloating	44
8.4	Other Biases and Limitations	45
8.5	Is Enhanced AML below the Gap Plausible?	46
9	Summary	46
A	A Compendium of Magnetic Braking Recipes	59
A.1	Verbunt & Zwaan (1981)	59
A.2	Rappaport, Verbunt & Joss (1983)	60
A.3	Kawaler (1988)	60
A.4	Mestel & Spruit (1987)	60
A.5	Andronov et al. (2003)	61
A.6	Ivanova & Taam (2003)	61
B	A Compilation of Masses and Radii for Non-Interacting Low-Mass Stars	62

LIST OF FIGURES

1	The dependence of stellar radius on mass-loss rate for two representative stellar masses	6
2	A comparison of all angular-momentum-loss recipes discussed in Appendix A	8
3	The ratios of the approximation to the Roche-lobe radius used in this paper to those suggested by Paczyński (1971) and Eggleton (1983)	10
4	The mass-radius relation of CV donor stars	12
5	Several key time scales as calculated along a standard-model CV evolution track	17
6	The mass-radius relationship of non-interacting low-mass stars	19
7	The effect of tidal and rotational deformation on the equilibrium stellar radius of a Roche-lobe-filling star	21
8	The expected amount of radius inflation due to irradiation along a standard-model CV evolution track	22
9	Self-consistent model fits to the observed properties of CV donors	25
10	The run of physical donor properties as a function of orbital period along standard and revised evolution tracks	27
11	The evolution of key binary parameters as a function of orbital period along our self-consistent model tracks	28
12	The evolution of key binary parameters as a function of time along our self-consistent model tracks	29
13	The evolution of the absolute magnitudes of both binary components as a function of orbital period along our self-consistent evolution tracks	30
14	Predicted and observed locations of the critical periods along a CV evolution track	31
15	Observed vs. predicted spectral types of CV donors as a function of orbital period	33
16	Predicted and observed WD temperatures as a function of orbital period	34
17	Infrared absolute magnitudes of CVs as a function of P_{orb}	36
18	The orbital period distribution of non-magnetic CVs and the associated dwarf nova fraction	38
19	A comparison of the predicted mass-transfer rates along our self-consistent evolution sequences and the critical rates for the occurrence of dwarf nova eruptions	39
20	Approximate period distributions calculated for the standard model and the revised best-fit model	41
21	The sensitivity of the inferred angular-momentum-loss rates to the assumed amount of non-mass-loss-related donor bloating	45

LIST OF TABLES

1	Coefficients for the Roche-lobe approximation (Equation 15) and the tidal/rotation deformation factor (Equations 27 and Equations 28) as functions of the effective polytropic index	11
2	The updated semi-empirical broken-power-law donor sequence for CVs	13
3	Binary and evolution parameters along the standard model track	52
4	Binary and evolution parameters along the revised (optimal) model track	53
5	Physical and photometric donor properties along the standard model track	54
6	Physical and photometric donor properties along the revised (optimal) model track	55
7	White dwarf properties along the standard model track	56
8	White dwarf properties along the revised (optimal) model track	57
9	Mean offsets (and associated dispersions) between observed absolute near-IR magnitudes of CVs with trigonometric parallaxes and predicted absolute magnitudes for CV donors	58
10	Statistics of the approximate period distributions shown in Figure 20	58
B1	Mass and radius measurements for non-interacting low-mass stars	62

1. INTRODUCTION

Cataclysmic variables (CVs) are interacting binary stars in which a white dwarf (WD) accretes material from a low-mass, near-main-sequence companion star. The long-term evolution of CVs is driven by angular momentum losses (AMLs). In what may be called the “standard model” of CV evolution, the dominant AML mechanism in long-period systems ($P_{orb} \gtrsim 3$ hrs) is “magnetic braking” (MB), whereas short-period CVs ($P_{orb} \lesssim 2$ hrs) are assumed to be driven by AML associated with the emission of gravitational radiation (GR).

The original motivation for the development of this standard model was the need to explain the dearth of active CVs in the period range $2 \text{ hrs} \lesssim P_{orb} \lesssim 3 \text{ hrs}$, the famous CV *period gap*. The standard model accomplishes this by assuming that when the donor star in a CV becomes fully convective – which happens at around $P_{orb} \simeq 3$ hrs – MB will abruptly shut off. At this point in its evolution, the donor star has been driven slightly out of thermal equilibrium and is therefore somewhat oversized for its mass. When the sudden cessation of MB reduces the mass-loss rate, the secondary contracts, causing it to lose contact with the Roche lobe altogether. The system then evolves towards shorter periods as a detached binary, driven only by GR. The Roche lobe eventually catches up with the donor again at $P_{orb} \simeq 2$ hrs. At this point mass transfer restarts, and the system re-emerges as an active CV at the bottom of the period gap.

The second key feature of the observed orbital period distribution of CVs is a sharp cut-off at $P_{min} \simeq 80$ min. In the standard model, the existence of this minimum period is again associated with the secondary’s mass-loss-induced loss of thermal equilibrium. More specifically, the donor’s thermal time scale below the gap ($\tau_{kh} \sim GM_2^2/L_2R_2$) increases faster than the time scale on which it loses mass ($\tau_{\dot{M}_2} \sim M_2/\dot{M}_2$). The secondary is therefore driven further and further from thermal equilibrium, to the point where its radius no longer shrinks at all in response to mass loss (and potentially even grows because of partial degeneracy). In this limit, the size of the binary orbit must increase again in order to accommodate the secondary, so there must be a change in the direction of the system’s period evolution. Systems that have passed beyond P_{min} are evolving back towards longer periods and are often called *period bouncers*. In principle (barring selection effects), P_{min} should stand out clearly in the P_{orb} distribution of CVs, not just as an abrupt drop in numbers, but as a narrow spike with a sharp, short-period cut-off.

The basic disrupted MB scenario described above was conceived more than 25 years ago (Rappaport et al. 1982, 1983; Spruit & Ritter 1983). It has survived as the standard model for CV evolution, primarily because it accounts for the existence of the period minimum and the period gap.¹ However, it has been recognized for some time now that there may be problems with this picture. Three issues, in particular, have often been noted as se-

rious challenges for the standard model.

First, the theoretically predicted minimum period ($P_{min} \simeq 65$ min)² is substantially shorter than the observed one. Until recently, the latter was usually estimated to be around $P_{min} \simeq 75$ min, based on the observed cut-off in the period distribution of the then available CV sample (e.g. Knigge 2006, hereafter K06). However, Gänsicke et al. (2009, hereafter G09) recently located the period spike at $P_{min} \simeq 82$ min in the SDSS CV sample, which makes this discrepancy even worse. Second, the standard model predicts that the Galactic CV population should be completely dominated by short-period systems and period bouncers. More specifically, the model predicts intrinsic abundances ratios of roughly 1:30:70 for long-period CVs, short-period pre-bounce CVs and period bouncers, respectively (e.g. Kolb 1993). Such a small ratio of long-period CVs to short-period (pre-bounce) CVs does not seem compatible with observations (Patterson 1998), even taking into account selection effects (Pretorius et al. 2007a; Pretorius & Knigge 2008a,b). Third, as discussed in more detail in Section 8.5, there is substantial evidence from non-interacting low-mass stars that fully convective objects (and perhaps even brown dwarfs) can sustain significant magnetic fields (e.g. Reiners 2009; Basri 2009; Donati & Landstreet 2009) and experience at least some spin-down due to MB (e.g. Barnes 2003; Reiners & Basri 2008). Whether the MB torque experienced by these objects is strong enough to matter in a CV setting is currently still an open question.

Taken at face value, all three of these issues can be viewed as pointing to an AML mechanism acting in addition to GR below the period gap (Patterson 1998; Pretorius et al. 2007a). So long as there remains at least a significant reduction in the AML loss rate at $P_{orb} \simeq 3$ hrs, such a modification would not destroy the model’s ability to account for the existence of the gap. However, there have also been other, more radical suggestions for changes to the standard model. These range from drastic reductions in the AML rate associated with MB (Andronov et al. 2003; Ivanova & Taam 2003), to the hypothesis that most CVs are too young to have reached the theoretical period minimum (in which case the observed short-period cut-off is simply an age effect; King & Schenker 2002).

Against this background, the goal of the present paper is to construct a new, comprehensive, semi-empirical CV evolution track based exclusively on the properties of their donor stars. This is a promising pursuit, since the secular evolution of a CV is intricately tied to – and in some sense controlled by – the properties of its secondary star. However, the main advantage of our method is this: it is likely to yield a valid estimate of the *secular* mass-transfer rate, i.e. the long-term average \dot{M}_2 that drives CV evolution. This is crucial, because the mass-transfer and accretion rates in a CV can vary on a wide range of shorter-than-evolutionary time scales. Methods based on observational tracers of \dot{M}_2 that are sensitive to such variations will therefore produce noisy estimates of the secular $\dot{M}_2(P_{orb})$ at best and misleading ones at worst.

¹ Actually, it is interesting to note that these original studies were careful to point out that the existence of the period gap suggested a sharp *reduction* in the strength of MB for fully convective stars, not necessarily a complete *cessation*.

² Note, however, that this is the value *before* any of the corrections discussed in Section 5.2.

³ In fact, the two most promising alternative methods – which are based on time-averaged accretion light (Patterson 1984; Warner 1987; Patterson 2009) and on the effective temperature of the accreting WD (Townesley & Bildsten 2002, 2003, 2004; Townesley & Gänsicke 2009), respectively – are both sensitive to variations in \dot{M}_2 on time scales that are much shorter than those produced by the most likely types of long-term mass-transfer-rate fluctuations (see Section 4).

In principle, it is quite simple to construct a donor-based CV evolution track: at fixed mass, the radius of a donor star in a CV is set primarily by the rate at which it loses mass (since this determines its degree of thermal disequilibrium). Thus, modulo the effects discussed in Section 5.2, *the amount by which a donor is bloated, relative to an isolated star of the same mass, is a measure of \dot{M}_2* . Given a set of empirically determined donor masses and radii spanning the full range of orbital periods, we can therefore infer how \dot{M}_2 (and hence the systemic AML that drives it) must vary with P_{orb} .

In practice, there are, of course, several obstacles to overcome before this program can be carried out. However, a good deal of the groundwork was already laid by K06, who used the sample of donor masses and radii presented by Patterson et al. (2005, hereafter P05) to construct a semi-empirical donor sequence for CVs. This sequence is built around a broken-power-law approximation to the donor mass-radius relation and provides a useful take-off and comparison point for the present study.

Apart from the obvious hope that our donor-based evolution track will turn out to be a reasonable description of reality, our main motivation for constructing it is to provide a new benchmark for work on CV evolution. As an empirically-based alternative to the standard model, our revised evolution sequence should provide a useful reference point for everything from theoretical population synthesis studies to detailed work on individual systems. In order to enable such uses, we will make the complete track (including physical and photometric parameters) available to the community, both as a simple “recipe” and as a set of tables in convenient electronic form.

The overall plan of this paper is as follows. We will begin in Section 2 by reviewing the links between the secular evolution of a CV and the properties of its donor star. This will include a comparison of some of the most popular MB prescriptions in the literature. In Section 3, we will then revisit and update the K06 semi-empirical donor sequence to take into account new results that have appeared since its construction. In Section 4 we will discuss how long-term mass-transfer-rate fluctuations can affect observational tracers of CV evolution, including accretion light, WD temperatures and donor radii. In Section 5, we will describe the construction of a complete, self-consistent CV evolution track that optimally fits the observed donor mass-radius relation. Along the way, we will explain how we deal with several calibration issues that slightly complicate the interpretation of donor inflation as a measure of \dot{M}_2 . In Section 6, we will present the resulting revised CV evolution sequence.

³ Misleading estimates will result, for example, if bright CVs in temporary high- \dot{M}_2 states have a substantially higher discovery probability.

More specifically, we will show the full range of binary and donor properties along this optimal evolution track and check its consistency with observed CV properties other than donor radii. In Section 7, we will consider some of the most important implications and applications of our track. Finally, in Sections 8 and 8, respectively, we will discuss our results and summarize our main conclusions.

2. CV EVOLUTION AND DONOR STARS

Since the ultimate goal of our study is to infer a global picture of CV evolution from the properties of the donor stars in these systems, it is worth reviewing the underlying physics. In the following sections, we will therefore briefly describe the link between AML and mass transfer in CVs, the response of a low-mass star to mass loss, and the close connection between donor properties and secular CV evolution.

2.1. Angular Momentum Loss and Mass Transfer in CVs

The evolution of CVs is driven entirely by AMLs. In particular, as long as the donor stays in contact with its Roche lobe, any systemic angular momentum loss at a rate $\dot{J}_{sys} < 0$ will drive a ML rate from the secondary that is given by (e.g. King & Kolb 1995)

$$\frac{\dot{M}_2}{M_2} = \frac{\dot{J}_{sys}}{JD} < 0. \quad (1)$$

In this evolution equation, J is the angular momentum of the binary system

$$J = M_1 M_2 \left(\frac{Ga}{M} \right)^{1/2} \quad (2)$$

and D is given by ⁴

$$D = \left(\frac{5}{6} + \frac{\zeta}{2} \right) - \frac{M_2}{M_1} + \alpha \left(\frac{M_2}{M_1} - \frac{1}{3} \frac{M_2}{M} \right) - \nu. \quad (3)$$

Here and throughout, M_1 denotes the mass of the WD primary, $M = M_1 + M_2$ the combined mass of the system, a the binary separation, and $\zeta = d \ln R_2 / d \ln M_2$ is the mass-radius index of the donor evaluated along its evolution track.

The parameter α that appears in the evolution equation is given by

$$\alpha = \frac{\dot{M}}{\dot{M}_2} \quad (4)$$

and measures the fraction of the mass lost from the secondary that is ultimately also lost from the system. In the case of conservative mass transfer, where all of the mass lost from the secondary is permanently accreted by the primary, $\alpha = 0$. Similarly, the parameter

$$\nu = \frac{\dot{J}_{CAML}/J}{\dot{M}_2/M_2} \quad (5)$$

⁴ The form of D in Equation 3 assumes Paczyński’s (1971, Equation 11) approximation for the Roche-lobe radius. For most other purposes in this paper, we will use the more precise approximation given by Equation 15. However, Paczyński’s approximation greatly simplifies the evolution equation and causes only a minor loss of accuracy (at the level of a few percent) in the calculation of \dot{M}_2 . This is entirely acceptable for our purposes.

measures the amount of *consequential* AML (CAML) that is associated with the mass-transfer process (King & Kolb 1995). Note that this is in addition to the systemic \dot{J}_{sys} , so the total AML rate from the system is

$$\dot{J} = \dot{J}_{sys} + \dot{J}_{CAML}. \quad (6)$$

Throughout this study, we will make the usual assumption that all of the material accreted by the primary is ejected again during nova eruptions, taking with it the specific angular momentum of the primary. This is consistent with the lack of a clear orbital period dependence in the measured WD masses for CVs (K06; also see Section 3) and implies $\alpha = 1$ and $\nu = \dot{M}_2^2/(M_1\dot{M})$.

2.2. The Response of a Low-Mass Star to Mass Loss

2.2.1. Basic Physics

As briefly noted in the Section 1, the reaction of a low-mass star to ML depends on two time scales. The first is the time scale on which the donor is losing mass ($\tau_{\dot{M}_2} \sim M_2/\dot{M}_2$); the second is the thermal (or Kelvin-Helmholtz) time scale on which thermal equilibrium is established ($\tau_{kh} \sim GM_2^2/L_2R_2$).

If $\tau_{\dot{M}_2} \gg \tau_{kh}$, ML is slow, and the donor is always able to maintain thermal equilibrium. In this limit, the secondary is indistinguishable from an isolated main-sequence (MS) star of the same mass. The mass-radius index, ζ , along its evolution track is then set by the equilibrium mass-radius relation of lower-MS stars ($R \simeq M^{0.8}$), i.e. $\zeta = \zeta_{eq} \simeq 0.8$. By contrast, if $\tau_{\dot{M}_2} \ll \tau_{kh}$, ML is fast (adiabatic), and the donor is completely unable to maintain thermal equilibrium. In this paper, we are mainly concerned with essentially unevolved CV donors with $M_2 \lesssim 0.6 M_\odot$, i.e. low-mass stars with a significant convective envelope. The response of such stars to adiabatic ML is to grow in size. The effective mass-radius index in this limit is $\zeta = \zeta_{ad} \simeq -1/3$ (e.g. Rappaport et al. 1982).

As it turns out, almost all models for CV evolution suggest that the donor stars in these systems find themselves in the intermediate regime, $\tau_{\dot{M}_2} \sim \tau_{kh}$ (see, for example, Figure 23 in Patterson (1984)). Thus (pre-bounce) CV secondaries are almost, *but not quite*, able to maintain thermal equilibrium. They should therefore be somewhat oversized relative to isolated MS stars, with an effective mass-radius index close to, but slightly below, the equilibrium value. This theoretical expectation has been confirmed empirically by P05 and K06, who found that CV donors are indeed up to 20%-30% larger than MS stars of the same mass. Moreover, the observed mass-radius relation for the secondaries in pre-bounce systems suggests $\zeta \simeq 0.65$ both above and below the period gap, which is indeed comparable to, but smaller than, the equilibrium value.

This radius inflation is the main observable effect of the ongoing ML on the donor star in a CV. It is this effect we will exploit in constructing our semi-empirical CV evolution track. As already explained in Section 1, the basic idea is to use the degree of donor bloating as a measure of the mass-loss rate from the donor.

2.2.2. The Radius Adjustment Time Scale: Sensitivity to Mass-Loss History

If we are going to use the radius of the secondary to reconstruct CV evolution, it is clearly important to ask how quickly the donor adjusts its radius to the prevailing mass-loss rate. In order for the radius to be a good tracer of the secular \dot{M}_2 , we would ideally like this time scale, τ_{adj} , to be comparable to the evolutionary time scale, i.e. the time scale on which the key system parameters evolve:

$$\tau_{ev} \sim \frac{J}{\dot{J}_{sys}} \sim \frac{M_2}{\dot{M}_2} \sim \frac{P_{orb}}{\dot{P}_{orb}}. \quad (7)$$

However, in order for CVs to even *have* a unique evolution track, it is actually required that $\tau_{adj} \ll \tau_{ev}$. If this were not the case, donors characterized by the same present-day mass and mass-loss rate, but starting from different initial conditions, could have very different radii. This would destroy the sharp edges of the period gap and the well-defined cut-off in the CV distribution at P_{min} . Thus, in practice, the best we can hope for is that τ_{adj} should be long compared to all other relevant time scales.

An analytical estimate of τ_{adj} for stars with a substantial convective envelope has been derived by Stehle et al. (1996) as ⁵

$$\tau_{adj} \simeq 0.05\tau_{kh,eq}. \quad (8)$$

Here, $\tau_{kh,eq}$ is the Kelvin-Helmholtz time scale the star would have if it were in thermal equilibrium. To the extent that $\tau_{ev} \sim \tau_{kh,eq}$ in CVs, τ_{adj} is generally indeed faster than τ_{ev} . As noted by Stehle et al. (1996), this also nicely explains the rapid convergence of CV evolution tracks characterized by different initial conditions, which is always observed in numerical studies (e.g. Paczynski & Sienkiewicz 1983; Kolb & Ritter 1992; Kolb 1993).

The time scale τ_{adj} can be thought of as the averaging time scale for donor radii: the observed radius is a measure of the mass-transfer rate averaged over the preceding few τ_{adj} . Does this mean that donor radii have *no* sensitivity to the mass-loss history on evolutionary time scales? In other words, is a donor radius measurement at given M_2 and P_{orb} a *unique* measure of \dot{M}_2 , irrespective of whether, for example, the star experienced faster or slower mass loss in the past?

If the condition $\tau_{adj} \ll \tau_{ev}$ were strictly satisfied, the answer would be yes. But is this actually true in practice? We try to answer this question in Figure 1, where we plot R_2 vs \dot{M}_2 for $M_2 = 0.1M_\odot$ (left panel) and $M_2 = 0.3M_\odot$ (right panel). The black dots in each panel are model radii obtained from donor evolution sequences of the type described in Section 5, under the assumption of *constant* mass-loss rate as a function of time. By contrast, the red squares correspond to model radii obtained for sequences in which the evolution is driven by standard GR-like (left panel) or MB-like (right panel) AML laws, but with variable normalizations (so as to produce a range of predicted \dot{M}_2 at given M_2). Both of these AML laws yield a decrease in \dot{M}_2 with time, i.e. mass loss was faster in the past than at present. The adopted range of mass-loss rates and AML prescriptions were chosen to

⁵ For reference, we note that Stehle et al. (1996) refer to τ_{adj} as τ_{per} and that they actually give $\tau_{per} \lesssim \tau_{kh,eq}/18$. However, it is easy to show from their work that $\tau_{per}/\tau_{kh,eq}$ is always close to 20, justifying the estimate given in Equation 8.

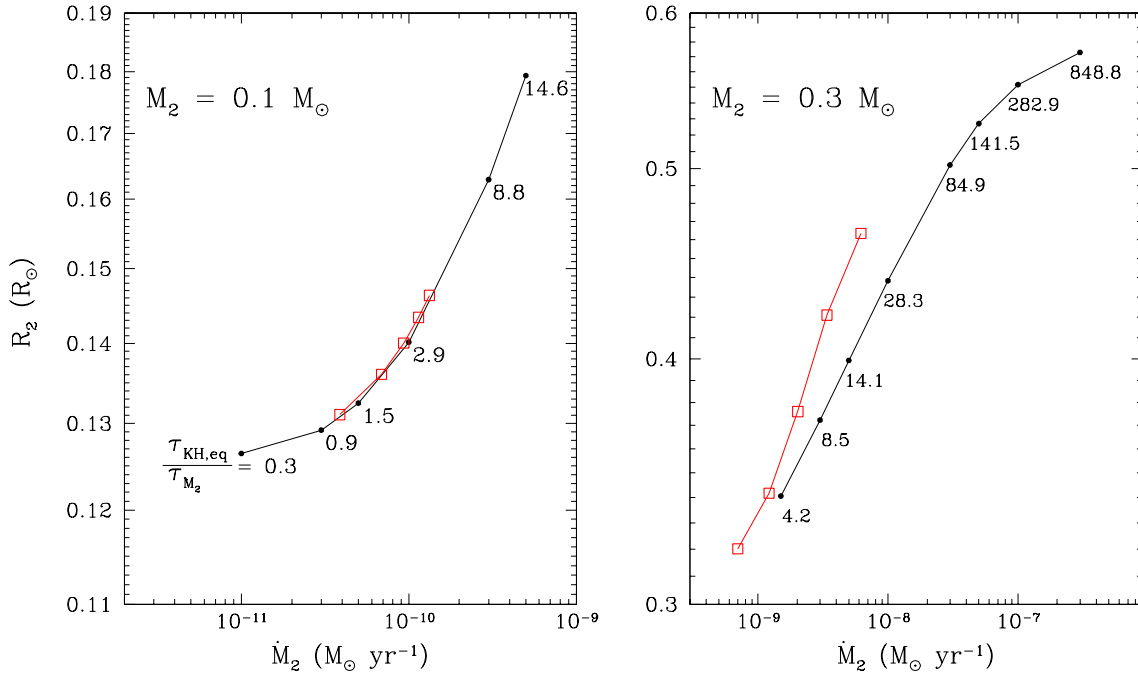


Figure 1. The dependence of stellar radius on mass-loss rate for two representative stellar masses: $M_2 = 0.1 M_\odot$ (left panel; typical of short-period CV donors) and $M_2 = 0.3 M_\odot$ (right panel; typical of long-period CV donors). The black dots connected by solid lines in each panel are model radii obtained from self-consistent donor evolution sequences of the type described in Section 5, under the assumption of *constant* mass-loss rate as a function of time. The red squares connected by dashed lines in each panel correspond to model radii obtained for sequences in which the mass-loss rates decrease with time. More specifically, the mass-loss rates in these sequences are driven by GR-like (Equation 9) or MB-like (Equation A7 with $\gamma = 3$) AML recipes, but adopting a range of different normalizations for each recipe. The numbers below the black points show the ratio of thermal to mass-loss time scales at these locations. The radii shown here do not include any of the corrections discussed in Section 5.2. If mass-loss history had no effect on stellar radii, the red (dashed) and black (solid) sequences should form lie on a single, unique curve.

be roughly appropriate for short-period, pre-bounce CVs (left panel) and long-period CVs approaching the period gap (right panel). If mass-loss history has no effect, all donors with the same present-day mass and mass-loss rate should have the same radius. Thus the red and black dots should fall on a single line.

This is, in fact, what we observe for our low-mass, short-period donors in the left panel, where the differences in donor radii at fixed \dot{M}_2 are always $< 1\%$. However, the long-period donors in the right panel exhibit larger differences, up to 13% at the highest \dot{M}_2 . There are two reasons for this contrasting behaviour. First, mass loss is faster compared to the donor’s thermal time scale above the gap. This is shown explicitly by the numbers below the constant- \dot{M}_2 sequences, which provide estimates of the ratio $\tau_{\text{KH,eq}}/\tau_{\dot{M}_2}$ at the specified points. As expected, we see that the radius difference – i.e. the impact of mass loss history – grows with increasing $\tau_{\text{KH,eq}}/\tau_{\dot{M}_2}$. In the right panel, we actually reach $\tau_{\dot{M}_2} \lesssim \tau_{\text{KH}}/20 \simeq \tau_{\text{adj}}$ for mass-loss rates $\dot{M}_2 \gtrsim 10^{-8}$, so significant sensitivity to mass-loss history is no surprise in this regime. Second, even though \dot{M}_2 decreases with time in both GR-like and MB-like sequences, the *rate* of decrease is faster in the MB-like sequences (see, for example, Figures 11 and 12 in Section 6.1). Thus MB-like sequences will differ more from constant- \dot{M}_2 sequences than GR-like sequences with the same present-day ratio of $\tau_{\text{KH,eq}}/\tau_{\dot{M}_2}$.

It is obvious from Figure 1 that the effect of mass-loss history cannot be safely ignored for long-period sys-

tems. In fact, despite the good agreement seen in the left panel, it cannot even be ignored for all short-period systems. The problem is that, almost by definition, the ratio $\tau_{\text{KH}}/\tau_{\dot{M}_2}$ increases throughout the evolution below the gap. In fact, it is this drop that produces the increasing degree of thermal disequilibrium that ultimately leads to period bounce (see Section 2.3.3). Thus while the impact of mass-loss history may be insignificant at $M_2 \simeq 0.1 M_\odot$ below the gap, it is expected to grow as we approach period bounce. We have verified that this is indeed the case. We therefore conclude that donor radii *can* be sensitive to the *shape* of the assumed AML law, both above the gap and below.⁶

These considerations have practical implications. For example, perhaps the most obvious way to obtain donor-based estimates of \dot{M}_2 for a set of CVs is to compute several constant- \dot{M}_2 sequences and, for each object with given M_2 , find the \dot{M}_2 that produces the best-matching radius. However, the sensitivity to mass-loss history means that the resulting $\dot{M}_2(P_{\text{orb}})$ recipe may not be self-consistent: an evolution sequence constructed with the inferred recipe may not reproduce the same donor radii (and may no longer be a good fit to the data). In practice, we therefore use a simplified method like this only to settle on a basic form for our AML recipe (Sec-

⁶ Note that this does not contradict the observed sharpness of the period gap and period minimum. After all, presumably all CVs actually evolve according to the *same* AML law. What the sharp edges in the period distribution require is insensitivity of donor radii to *initial conditions* for a *given* AML law. This is a weaker requirement than insensitivity to *different forms* of AML.

tion 5.3), but then actually fit the data in detail with self-consistent evolution sequences (Section 5.4).⁷

2.2.3. M_2 - L_2 and M_2 - $T_{eff,2}$ Relations

Since the secondary star is not in thermal equilibrium, it does not obey the mass-luminosity relation of isolated MS stars. Instead, its effective temperature is, to a good approximation, set entirely by M_2 and equal to the equilibrium temperature of a MS star of identical mass, $T_{eff,2} \simeq T_{eff,eq}$ (Baraffe & Kolb 2000; Kolb et al. 2001a). Since the donor is oversized for its mass, but maintains its equilibrium temperature, its luminosity, $L_2 = 4\pi R_2^2 \sigma T_{eff,2}^4$, exceeds the nuclear luminosity generated in the core.

The approximation $T_{eff,2} \simeq T_{eff,eq}$ only breaks down as $P_{orb} \rightarrow P_{min}$ and the donor mass approaches the hydrogen-burning limit, $M_2 \rightarrow M_H$. In the brown dwarf regime, there is no thermal equilibrium configuration, so even the structure and temperature of isolated objects depends strongly on age (Chabrier & Baraffe 2000). In the CV setting, this means that $T_{eff,2}$ will depend on the mass-loss and thermal history of the donor in this regime.

2.3. The Connection between CV Donors and Evolution

2.3.1. Magnetic Braking

Equation 1 shows that the evolution of CVs as semi-detached systems is driven entirely by systemic AMLs: without \dot{J}_{sys} , there would be no mass transfer. Now all close binaries experience AML due to GR, at a rate given by (Paczynski 1967; Webbink 1976)

$$\dot{J}_{GR} = \frac{-32}{5} \frac{G^{7/2}}{c^5} \frac{M_1^2 M_2^2 M^{1/2}}{a^{7/2}}. \quad (9)$$

This acts all the time in every binary system and thus sets a minimum baseline AML rate for every CV. However, it is generally agreed that, at least above the period gap, CVs experience AML rates far in excess of GR. Thus at least one additional AML mechanism is required, which is most usually taken to be magnetic braking.

In general, “magnetic braking” describes any AML associated with a magnetized stellar wind. In the case of CVs, this wind is thought to be driven from the donor star. This leads to the first important connection between donor properties and secular CV evolution: the dominant systemic AML mechanism invoked in virtually all evolution scenarios for long-period CVs is entirely associated with the secondary star in these systems. Moreover, it is the assumed cessation of MB when the donor becomes fully convective that produces the period gap in the standard model of CV evolution.

The basic physics of MB in CVs are easy to understand. Essentially all low-mass stars drive a relatively weak stellar wind. As long as this wind is highly ionized, it is effectively forced to co-rotate with the stellar

magnetic field out to the Alfvén radius and thus exerts a significant spin-down torque on the star. In a CV setting, tidal forces maintain essentially perfect synchronization between the spin of the Roche-lobe-filling donor star and the binary orbit, so the net effect of the wind from the donor star is the extraction of angular momentum from the binary system at a rate of $\dot{J}_{sys} = \dot{J}_{MB} < 0$.

Unfortunately, the conceptual simplicity of MB as an AML mechanism does not mean that it is easy to model. In fact, there have been so many attempts to describe MB in the literature that it can be hard to keep track of the differences between them. We therefore provide brief descriptions of some of the most widely-used MB prescriptions in Appendix A.

In Figure 2, we present a direct comparison of the AML rates predicted by GR and all of the MB recipes described in Appendix A. For the purpose of this simple comparison, we took the stellar parameters from the standard 5 Gyr MS models of Baraffe et al. (1998, hereafter BCAH98) and then used the period-density relation (Equation 12) to calculate the corresponding orbital period. Thus we assume that the donor can be approximated as an ordinary MS star, despite the fact that it fills the Roche lobe and undergoes mass loss. There is then a simple one-to-one relationship between donor mass and orbital period (and no period gap). This would not be an acceptable approximation for self-consistent evolutionary calculations, which should take into account the ML-driven inflation of the donor. However, it is well suited to our present purpose, since it provides for a particularly clean and simple comparison of the different AML laws.

The main point to take away from Figure 2 is that there are *huge* differences between different MB prescription at fixed M_2/P_{orb} . For example, the widely used Kawaler (1988, Appendix A.3, Equation A10) prescription with $n_k = 1.5$ produces approximately 100,000 times stronger braking at $M_2 \simeq 0.3 M_\odot$ than the “saturated” prescriptions suggested by Andronov et al. (2003, Appendix A.5, Equation A16) and Ivanova & Taam (2003, Appendix A.6, Equation A17).⁸ In fact, the saturated prescriptions are not even competitive with GR for $M_2 \lesssim 0.4 M_\odot$.

These are not new results, of course: after all, the saturated prescriptions were *designed* to be weak at high rotation rates. However, Figure 2 also shows that, even among the unsaturated prescriptions, AML rates can differ by at least 3 orders of magnitude. For example, compare the classic Verbunt & Zwaan (1981, Appendix A.1, Equation A6) prescription with $k^2 = 0.1$ to the Kawaler (1988) one with $n_k = 1.5$ at $M_2 \simeq 0.3 M_\odot$. Moreover, the *shapes* of the AML laws (i.e. their dependence of M_2/P_{orb}) vary widely between different MB formulations. Some predict a weakening of MB with decreasing M_2/P_{orb} (e.g. Verbunt & Zwaan 1981 and Mestel & Spruit 1987, Appendix A.4, Equation A13), while others actually predict a strengthening (e.g. Kawaler 1988). Clearly, we cannot rely on the existing MB prescriptions to guide us in defining the functional form and strength

⁷ Throughout this paper, the term “self-consistent” is used only in this restricted sense. It should not be confused with “physically self-consistent”, which is a much stronger condition. For example, the “scaled-GR” models we use to model enhanced AML below the period gap in Sections 5 and 6 are internally self-consistent, but not physically self-consistent.

⁸ We are using the term “saturated” loosely here, to simply refer to MB prescriptions in which AML is suppressed at high stellar rotation rates. In the Ivanova & Taam (2003) recipe, this suppression is accomplished without any actual saturation of the stellar magnetic field.

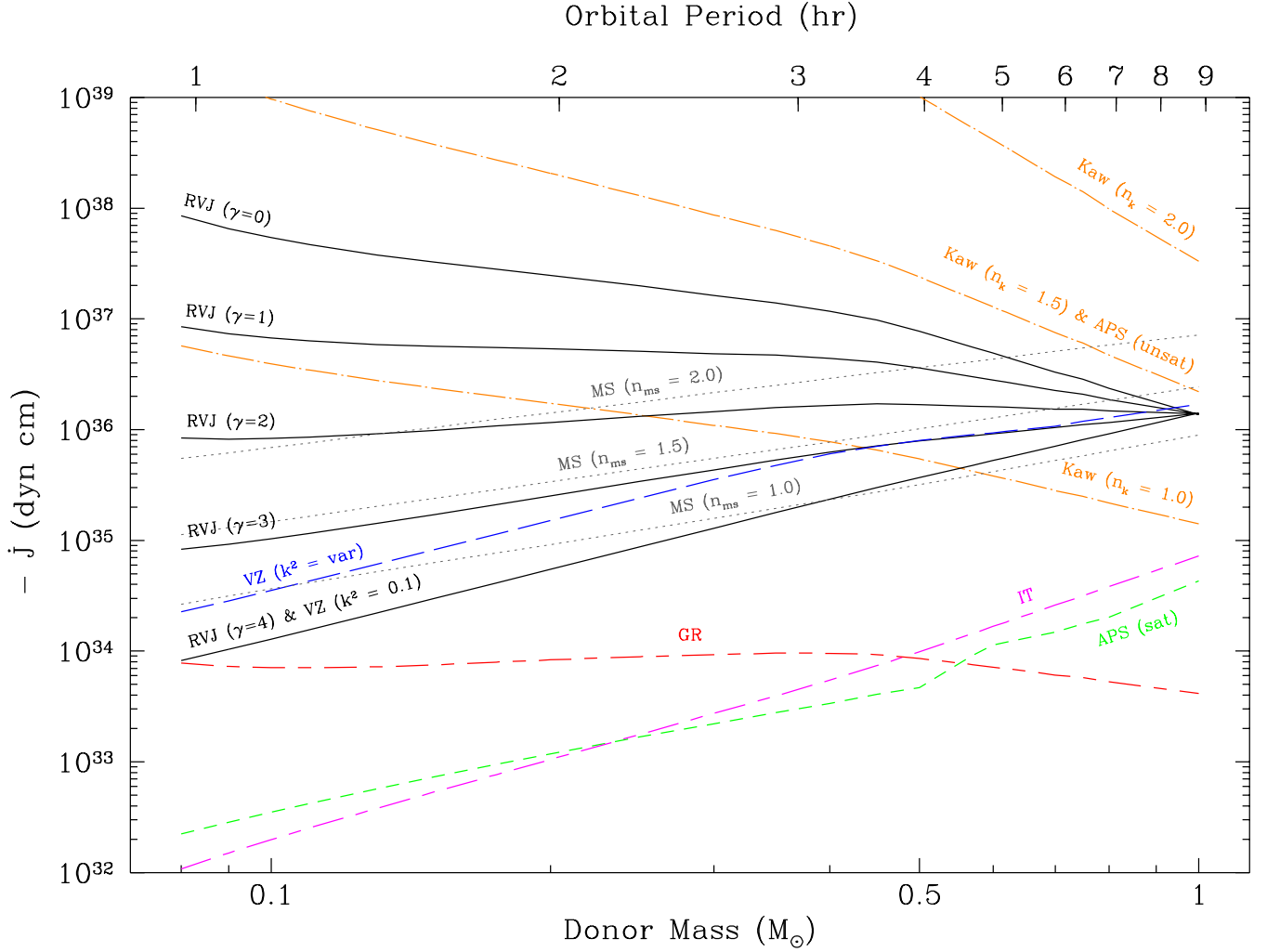


Figure 2. A comparison of all angular-momentum-loss recipes discussed in Appendix A. All AML rates are calculated assuming a $0.75 M_{\odot}$ primary and an unevolved Roche-lobe-filling MS secondary in marginal contact. Thus the secondary is assumed to follow the standard 5-Gyr BCAH98 mass-radius relationship, and the orbital period is calculated from the approximate period-density relation given by Equation 12. None of the corrections discussed in Section 5.2 are included. The red long-dash-short-dash line corresponds to GR-driven AML (Equation 9). The blue long-dashed line shows the classic Verbunt & Zwaan (1981, Appendix A.1, Equation A6) prescription with moment of inertia, k , estimated from stellar models. The solid black lines mark the Rappaport et al. (1983, Appendix A.2, Equation A7) prescription for different power-law indices, γ , as marked. Note that the $\gamma = 4$ recipe is identical to a Verbunt & Zwaan (1981) law with constant $k^2 = 0.1$ by construction. The orange dash-dotted line marks the Kawaler (1988, Appendix A.3, Equation A10) recipe for different power-law indices, n_k , as marked. Grey dotted lines mark the Mestel & Spruit (1987, Appendix A.4, Equation A13) law for different power-law indices, n_{ms} , as marked. The green short-dashed line shows the saturated model suggested by Andronov et al. (2003, Appendix A.5, Equation A16). The unsaturated limit of this model is identical to the Kawaler (1988) recipe with $n_k = 1.5$ by construction. Finally, the saturated AML law suggested by Ivanova & Taam (2003, Appendix A.6, Equation A17) is shown as a long-dashed magenta line. The main thing to take away from this figure is the enormous range in shapes and strengths, even for conceptually similar AML prescriptions.

of AML in CVs. We will therefore adopt the Rappaport et al. (1983, Appendix A.2, Equation A7) parameterization when constructing self-consistent evolution tracks in Section 5.4. This is simply because the strength and shape can be controlled very easily by varying the normalization and the power-law index γ , respectively.

In studies of CV evolution, MB is usually assumed to stop abruptly when the secondary becomes fully convective. In isolated stars, this happens at around $M_2 \simeq 0.35 M_{\odot}$ (Chabrier & Baraffe 1997), but in mass-losing stars, the transition will generally occur at lower masses ($M_2 \simeq 0.2 - 0.3 M_{\odot}$; see Figure 14 in Section 6.2). The conventional argument for the assumed cessation of MB

is that the magnetic field in solar-type, low-mass stars is thought to be anchored at the interface between the radiative core and the convective envelope (the tachocline; e.g. MacGregor & Charbonneau 1997; Charbonneau & MacGregor 1997). Since fully convective stars do not possess such an interface, the magnetic field – and with it MB – is assumed to vanish at this point.⁹ In

⁹ As already noted in Section 1, observations of non-interacting stars do not support this assumption. Indeed, it is quite clear today that fully convective objects are capable of sustaining significant magnetic fields. These are probably generated via a different *type* of dynamo than that responsible for the fields of partly radiative stars. See Section 8.5 for further discussion of this key point.

the standard model, the only remaining AML mechanism is then GR, which operates at a much slower rate $|\dot{J}_{GR}| \ll |\dot{J}_{MB}|$ and thus produces a lower mass-transfer rate $|\dot{M}_{2,GR}| \ll |\dot{M}_{2,MB}|$.

2.3.2. The Period Gap

The precise origin of the period gap in the standard model is now easy to understand. The shutdown of strong MB near $P_{orb} \simeq 3$ hrs leads to a sudden reduction in \dot{J}_{sys} . This in turn causes a drop in \dot{M}_2 (Equation 1) and an increase in the ratio $\tau_{\dot{M}_2}/\tau_{kh}$. This slower ML cannot sustain the existing level of donor of inflation, so the secondary will shrink and lose contact with the Roche lobe altogether. This loss of contact is a fast process, because the Roche-lobe and donor radii are normally equal to within roughly a pressure scale height, H , where $(H/R_2) \sim 10^{-4}$ (e.g. Ritter 1988). Thus the secondary only has to contract by a few scale heights in order to break contact.

At this point, ML ceases entirely, and the CV enters the period gap as a newly detached system. Meanwhile, the donor continues to contract towards its thermal equilibrium state, but the system nevertheless continues to evolve towards shorter orbital periods, since it still loses angular momentum due to GR. Since M_1 , M_2 and M are all constant in a detached system, Equation 2 shows that this AML will cause the binary orbit to decay. At $P_{orb} \simeq 2$ hrs, the shrinking Roche lobe therefore catches up with the donor star again. At this point, mass transfer restarts, and the system re-emerges as an active CV.

Provided that the time it takes a CV to evolve through the period gap is sufficiently long, the secondary will be able to relax completely and emerge from the bottom of the gap with the equilibrium radius appropriate for its mass. Is this condition met? King & Kolb (1995) show that, following the cessation of contact, the donor's radius will relax back to its equilibrium value on a time scale

$$\tau_{relax} = \frac{R_2 - R_{eq}}{(\zeta - \zeta_{ad})R_2} \tau_{\dot{M}_2}, \quad (10)$$

where R_2 , ζ and \dot{M}_2 are evaluated just prior to loss of contact at the upper edge of the gap, and $\zeta_{ad} = -1/3$ for the low-mass stars of interest. We find that τ_{relax} is indeed shorter than the gap-crossing time for all of the models we consider. We therefore expect the secondary to emerge from the bottom of the gap indistinguishable from a MS star of the same mass.

The width of the period gap in this picture is directly determined by the degree of donor inflation above the gap. Combining the Paczyński (1971) approximation for the volume-averaged Roche-lobe radius

$$\frac{R_2}{a} = 0.462 \left(\frac{q}{1+q} \right)^{1/3} \quad (11)$$

(which is valid for mass ratios $q = \frac{M_2}{M_1} \lesssim 0.8$) with Kepler's third law yields the well-known period-density relationship for Roche-lobe-filling stars

$$< \rho_2 > = \frac{3M_2}{4\pi R_2^3} \simeq 107 P_{orb,h}^{-2} \text{ g cm}^3. \quad (12)$$

where $P_{orb,h}$ is the orbital period in units of hours. Now,

according to the disrupted AML scenario, M_2 is the same at the upper and lower edges of the period gap ($P_{gap,\pm}$), so Equation 12 implies that the ratio of the donor radii at the gap edges must satisfy

$$\frac{R_{2,+}}{R_{2,-}} = \left(\frac{P_{gap,+}}{P_{gap,-}} \right)^{2/3}. \quad (13)$$

If the donor emerges from the gap in thermal equilibrium, $R_{2,-} = R_{2,eq}$, the gap width is set entirely by the degree of donor inflation above the gap. K06 estimated $P_{gap,-} = 2.15 \pm 0.03$ hrs and $P_{gap,+} = 3.18 \pm 0.04$ hrs, which implies that the radius of a CV donor entering the gap is about 30% larger than that of an equal-mass MS star.

2.3.3. The Period Minimum and the Period Spike

The existence and location of the period minimum for CVs is also directly related to the properties of their donor stars. The easiest way to see this is to logarithmically differentiate the period-density relation (Equation 12) and use the mass-radius index to substitute for $(\dot{M}_2/M_2) = \zeta^{-1}(\dot{R}_2/R_2)$. This yields the evolution equation for the orbital period of the system

$$\frac{\dot{P}_{orb}}{P_{orb}} = \frac{3\zeta - 1}{2} \frac{\dot{M}_2}{M_2}. \quad (14)$$

Equation 14 shows that the orbital period decreases for $\zeta > 1/3$, but must increase for $\zeta < 1/3$. As noted above, a CV donor emerges from the bottom of the period gap in (or close to) thermal equilibrium, with $\zeta \simeq \zeta_{eq} \simeq 0.8$, but once mass transfer resumes below the gap, the secondary will again struggle to maintain this.

In fact, as the secondary is being whittled down to lower and lower masses, τ_{kh} increases faster than $\tau_{\dot{M}_2}$, even if the mass transfer is driven solely by GR. Thus $\tau_{\dot{M}_2}/\tau_{kh}$ continuously decreases with time, and the cumulative loss of thermal equilibrium accelerates. The mass-radius index ζ must therefore drop away from ζ_{eq} towards $\zeta_{ad} \simeq -1/3$. Note that even if mass loss was very slow, the donor must eventually pass the Hydrogen-burning limit ($M_H \simeq 0.07 M_\odot$ for isolated, solar metallicity stars). Beyond this, thermal equilibrium is, by definition, impossible, since there is no internal energy source. In this limit, ζ will approach the index of the mass-radius relationship for brown dwarfs, which (at fixed age) is also $\zeta \simeq -1/3$ (Chabrier et al. 2009).¹⁰

These considerations show that ζ must inevitably pass through the critical value $\zeta = 1/3$, at which point $\dot{P}_{orb} = 0$ and hence $P_{orb} = P_{min}$. Since ζ depends on $\tau_{\dot{M}_2}/\tau_{kh}$, the exact location of the minimum period depends on \dot{M}_2 and hence \dot{J}_{sys} . For fast ML/AML, P_{min} is generally reached sooner (and is therefore larger) than for slow ML/AML. Note, however, that faster ML and AML does not necessarily imply larger donor masses at P_{min} ; after all, fast ML also decreases M_2 faster than

¹⁰ Actually, as we shall see later, the mass-radius index of CV donors below the Hydrogen-burning limit tends to approach $\zeta \simeq 0$. There are two reasons for this. First, the brown dwarf mass-radius index is not constant, but goes to $\simeq 0$ with decreasing mass. Second, in a CV setting, different donor masses correspond to different ages. More specifically higher-mass sub-stellar donors are younger (and hence relatively larger) than lower-mass donors.

slow ML. For GR-like AML prescriptions (i.e. with the same functional form, but different normalizations; see Section 5.4), faster ML/AML actually corresponds to *lower* M_2 at P_{min} . Thus M_2 will drop below M_H *before* P_{min} is reached. At least in the context of slow, GR-like AML prescriptions, $M_2 < M_H$ is therefore a necessary, but not sufficient condition for identifying period bouncers.

The period minimum should be a prominent feature in the orbital period distribution of the Galactic CV population. In particular, it should not just produce a sharp cut-off in the distribution, but a strong and fairly narrow spike. This is easy to understand: the amount of time a given CV spends in a particular orbital period range ($P_{orb} \rightarrow P_{orb} + \Delta P_{orb}$) is inversely proportional to the average value of \dot{P}_{orb} in that range. Now $\dot{P}_{orb} = 0$ at P_{min} , so systems spend rather a long time there. In a population close to steady-state, this means that many systems will be found near P_{min} at any given time. This produces the period spike that is seen in essentially all CV population synthesis studies (e.g. Kolb 1993; Kolb & Baraffe 1999; Howell et al. 2001; Barker & Kolb 2003) and which has now been clearly detected observationally (G09). However, as already noted in Section 1, the minimum period predicted by the standard model of CV evolution ($P_{min} \simeq 65 \text{ min}^{11}$) is substantially shorter than the observed one ($P_{min} \simeq 82 \text{ min}$). One possible solution to this problem is to allow for AML rates in excess of pure GR below the period gap (e.g. Patterson 1998), another is to assume that CV donors are heavily spotted (Littlefair et al. 2008, hereafter L08).

3. THE SEMI-EMPIRICAL DONOR SEQUENCE REVISITED

In K06 we constructed a complete, semi-empirical donor sequence for CVs, which provided all physical and photometric properties of a typical CV secondary as a function of P_{orb} . The two key ingredients for this donor sequence are (i) a broken-power-law fit to the empirical $M_2 - R_2$ relation and (ii) the theoretically expected MS-like $M_2 - T_{eff}$ relation. These two constraints are sufficient to fully specify the physical parameters of CV donors as a function of P_{orb} ; these can then be used as input to stellar atmosphere models to obtain the predicted photometric properties of the secondaries as well. We will refer to donor sequences constructed in this way generically as “broken-power-law sequences” from here on.

The K06 broken-power-law donor sequence has found fairly widespread use, both for distance estimation and as a benchmark for what constitutes a “normal” CV secondary star at a given P_{orb} . It also provides an obvious and convenient point of comparison for the self-consistent CV evolution tracks presented in Section 6. However, some updates are in order to bring the donor sequence in line with recent observational developments and improve its accuracy. Since the construction of the broken-power-law $M_2 - R_2$ relation and associated donor sequence was explained in some detail in K06, we will limit our discussion here only to *differences* between the data and

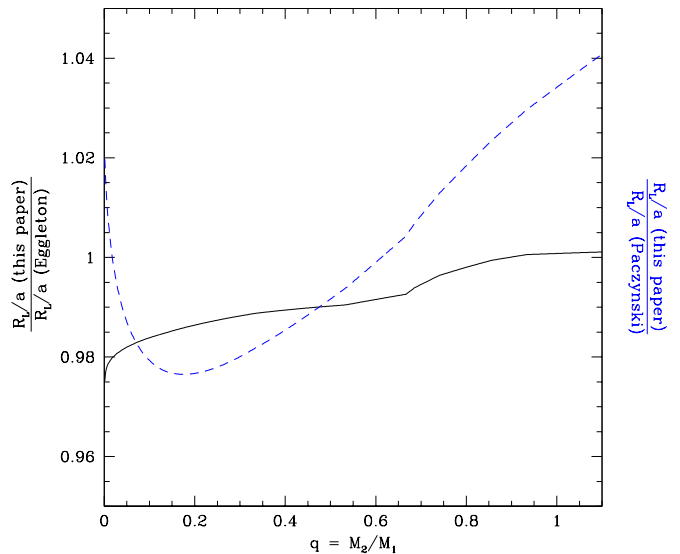


Figure 3. The ratios of the R_L/a approximation used in this paper to those suggested by Paczyński (1971, blue dashed line) and Eggleton (1983, black solid line). The latter two approximations treat the secondary star as a point source in estimating the critical potential, whereas our approximation, which is based on the work on Sirotkin & Kim (2009), treats the donor as a polytrope. The effective polytropic index is itself a function of donor mass (and hence mass ratio) in this prescription, as listed in Table 1.

methods used in this update compared to those used in constructing the original sequence.

Let us begin with the $M_2 - R_2$ relation. First, we have added the system parameters of six of the new, short-period, eclipsing SDSS CVs analysed by L08. We exclude only SDSS J1507, since this is probably a halo CV (Patterson et al. 2008) or possibly a recently born system (Littlefair et al. 2007). However, we do use L08’s revised system parameters for OY Car, which are slightly different from those given in Wood & Horne (1990).

Second, we now adopt the location of the period spike, $P_{min} = 82.4 \pm 0.7 \text{ min}$ (G09), as the best estimate of the minimum period. This effectively sets the location of one of the two breaks in the broken-power-law parameterization (the other is set by the donor mass just above and below the period gap).

Third, we have replaced Paczyński’s (1971) approximation for the volume-averaged Roche-lobe size (Equation 11) with a more precise approximation based on the results of Sirotkin & Kim (2009, hereafter SK09). This new approximation actually goes beyond the pure Roche model, in that it does not represent the donor as a point source in the potential, but as a polytrope with polytropic index n . The functional form adopted for R_L/a is similar to Eggleton’s (1983) improved approximation,

$$\frac{R_L}{a} = \frac{c_1 q^{c_2}}{c_3 q^{c_4} + \ln(1 + q^{c_5})}, \quad (15)$$

but with fit parameters, $c_i(n)$, that depend on the polytropic index of the Roche-lobe-filling star. When using Equation 15 in a CV setting, it is therefore necessary to

¹¹ This “classic” estimate ignores corrections such as those described in Section 5.2.

Table 1

Coefficients for the Roche-lobe approximation (Equation 15) and the tidal/rotation deformation factor (Equations 27 and Equations 28) as functions of the effective polytropic index, n . Data from Sirotkin & Kim (2009) and Sirotkin (private communication).

Coefficient	Eggleton (1983) approximation	Effective Polytropic Index			
		$n = 1.50$	$n = 1.75$	$n = 2.00$	$n = 2.50$
Corresponding Stellar Mass					
$\leq 0.1M_{\odot}$ $0.51M_{\odot}$ $0.56M_{\odot}$ $0.64M_{\odot}$					
Roche lobe coefficients (Equation 15)					
c_1	0.49	0.5126	0.5296	0.5303	0.5310
c_2	$\frac{2}{3}$	0.7388	0.7661	0.7640	0.7616
c_3	0.6	0.6710	0.7112	0.7100	0.7083
c_4	$\frac{2}{3}$	0.7349	0.7577	0.7554	0.7526
c_5	$\frac{1}{3}$	0.3983	0.4232	0.4213	0.4191
Tidal and rotational deformation coefficients (Equation 28)					
N_{iso}	-	0.42422	0.38589	0.36475	0.35150
d_1	-	0.0191	0.0144	0.01084	0.00588
d_2	-	0.9561	0.9850	0.9980	1.025
d_3	-	0.3557	0.3880	0.3945	0.4086
d_4	-	0.9130	0.9333	0.9470	0.9767
d_5	-	1.1635	1.205	1.202	1.198

specify the polytropic index that best describes the donor under consideration. Fully convective stars (i.e. donors below the period gap) are well-described by $n = 3/2$ polytropes. For more massive donors, we interpolate on the relationship between stellar mass and effective polytropic index given in Table 3 of Lai et al. (1994). This was derived by matching the properties of polytropes to those of MS stellar models. In Table 1, we provide the stellar masses, M_2 , and coefficients, c_i , for a small grid of polytropic indices that span the parameter space relevant for CVs. The coefficients for $n = 3/2$ were taken from SK09; coefficients for other n were kindly provided to us by Fedir Sirotkin (private communication).

Implementing this more complex form of R_L/a is just about worth it. Figure 3 shows how R_L/a as calculated via Equation 15 (with polytropic index n varying with mass ratio as given in Table 1) compares to both the Paczyński (1971) and the Eggleton (1983) approximations. The difference between the n -dependent formulation and the standard ones (in which the donor is represented as a point source in the potential) can amount to a few percent and varies systematically with mass ratio. Note that the point-source Roche model is least accurate for fully convective low-mass star, i.e. donors below the gap. Physically, this is because such stars are not very centrally concentrated.

Fourth, we have slightly modified the χ^2 -fitting method we use to infer the optimal broken-power-law parameters. More specifically, we found that explicitly including systematic uncertainties in the fit (see K06 for details) could sometimes produce unphysical results in the period bouncer regime. This is probably due to bias affecting the method in particular limiting cases. We therefore now use a standard χ^2 fit (without a systematic error term), but still allowing for intrinsic dispersion at the level needed to achieve $\chi^2_{\nu} = 1$.

Figure 4 shows the new broken-power-law fit to the updated $M_2 - R_2$ data set. The optimal mass-radius

relation is

$$\frac{R_2}{R_{\odot}} = \begin{cases} 0.118 \pm 0.004 \left(\frac{M_2}{M_{\text{bounce}}} \right)^{0.30 \pm 0.03} & \text{for } M_2 < M_{\text{bounce}} \\ 0.225 \pm 0.008 \left(\frac{M_2}{M_{\text{conv}}} \right)^{0.61 \pm 0.01} & \text{for } M_{\text{bounce}} < M_2 < M_{\text{conv}} \\ & P_{\text{min}} < P_{\text{orb}} < P_{\text{gap},-} \\ 0.293 \pm 0.010 \left(\frac{M_2}{M_{\text{conv}}} \right)^{0.69 \pm 0.03} & \text{for } M_{\text{conv}} < M_2 < M_{\text{evol}} \\ & P_{\text{gap},+} < P_{\text{orb}} < P_{\text{evol}}, \end{cases} \quad (16)$$

where the following quantities have been assumed

$$\begin{aligned} M_{\text{bounce}} &= 0.069 \pm 0.009 M_{\odot} \\ M_{\text{conv}} &= 0.20 \pm 0.02 M_{\odot} \\ M_{\text{evol}} &\simeq 0.6 - 0.7 M_{\odot} \\ P_{\text{min}} &= 82.4 \pm 0.7 \text{ min} \\ P_{\text{gap},-} &= 2.15 \pm 0.03 \text{ hr} \\ P_{\text{gap},+} &= 3.18 \pm 0.04 \text{ hr} \\ P_{\text{evol}} &\simeq 5 - 6 \text{ hr}. \end{aligned} \quad (17)$$

The notation here is the same as in K06, i.e. P_{min} , $P_{\text{gap},-}$, $P_{\text{gap},+}$ and P_{evol} , respectively, are the orbital periods at period minimum, at the bottom and top of the period gap, and at the point where systems with evolved secondaries are expected to start dominating the Galactic CV population. Similarly, M_{bounce} , M_{conv} and M_{evol} are the corresponding donor masses at these points (with $M_2 = M_{\text{conv}}$ at both $P_{\text{gap},-}$ and $P_{\text{gap},+}$, since the donor mass does not change during evolution through the gap).

The fit parameters and errors are quite similar to those derived in K06, but there are some differences in the bouncer and short-period regimes. These differences arise primarily because the larger value of P_{min} has caused some data to be shifted from the short-period regime into the bouncer regime, and also because of the addition of high-precision data points from L08. However, all of the main conclusions of K06 still hold. In particular, the intrinsic dispersion in radius is still only 0.01-0.02 dex in all three regimes, in line with the theoretical expectation that all unevolved CVs should quickly converge onto a unique evolution track (with some WD-

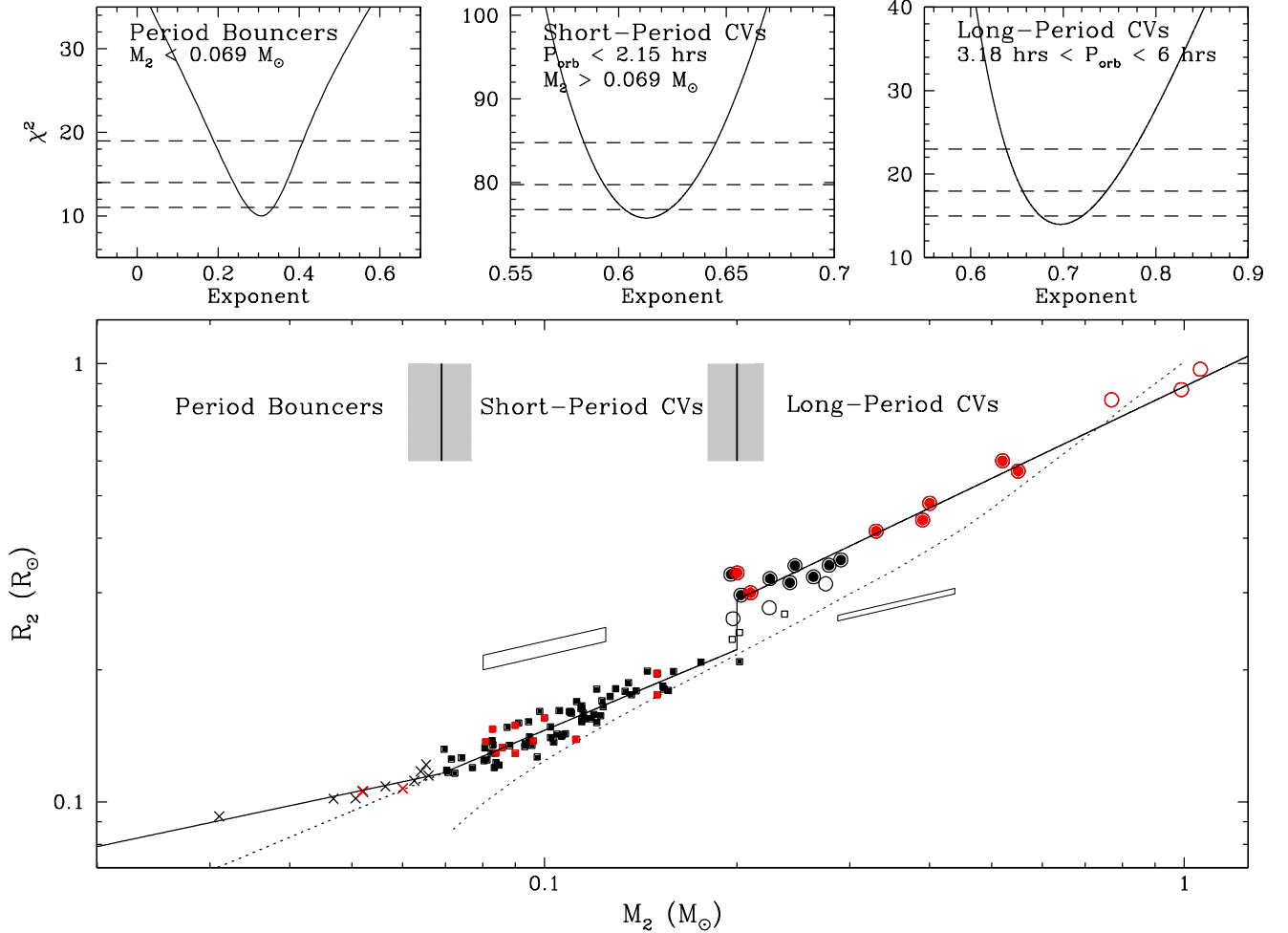


Figure 4. The mass-radius relation of CV donor stars. *Bottom panel:* Points shown are empirical mass and radius estimates for CV donors. Superhumpers are shown in black, eclipsers in red. Filled squares correspond to short-period CVs, filled circles to long-period systems, and crosses to candidate period bouncers. The parallelograms illustrate the typical error on a single short-period or long-period CV. Open symbols were ignored in fits to the data since they correspond to systems in the period gap or long-period (probably evolved, Podsiadlowski et al. 2003) systems. The solid lines show the optimal broken-power-law fit to the data in the period bouncer, short-period and long-period regions. The dotted line is the mass-radius relation for main sequence stars taken from the 5 Gyr BCAH98 isochrone. *Top panels:* Constraints on the power law exponents of the $M_2 - R_2$ relations in the three period/mass regimes. For each regime, we plot χ^2 vs exponent and indicate the χ^2 corresponding to 1σ , 2σ and 3σ around the minimum with horizontal dashed lines.

mass-dependent scatter). Also, the power-law slope derived for period bouncers is (just) consistent with an increasing period in this regime (i.e. $\zeta < 1/3$, c.f. Equation 14).

We can now use this new $M_2 - R_2$ relation to create our updated donor sequence. Again, we will only discuss how our implementation here differs from that described in K06. First, in K06 we adopted the $M_2 - T_{eff}$ relation suggested by the BCAH98 5 Gyr MS models down to $T_{eff} \simeq 2000$ K, switching to the 1 Gyr “DUSTY” (Baraffe et al. 2002) and, ultimately, 1 Gyr “COND” (Baraffe et al. 2003) isochrones at lower temperatures. We adopted younger isochrones in the brown dwarf regime, because CV secondaries are essentially born as brown dwarfs when their masses drop beyond the Hydrogen burning limit. This need to adopt a characteristic “age” for donors in the brown dwarf regime was an

obvious weakness of the original donor sequence.¹² Here, we instead adopt the $M_2 - T_{eff}$ relation suggested by the revised (best-fit) evolution track presented in Section 6.1. Clearly, this still does not amount to a self-consistent treatment, since the donor properties along this track are not identical to those on the broken-power-law donor sequence. Moreover, the stellar models on which this track is based do not account for dust formation and settling (see discussion in Section 5.4). Nevertheless, we expect this to be at least a mild improvement over the ad-hoc adoption of a particular age for the lowest-mass

¹² Note that this weakness *only* affects donors at the lowest masses, in or close to the brown dwarf regime. As explained in Section 2.2.3, at higher masses ($M_2 \gtrsim 0.1 M_\odot$), the $M_2 - T_{eff}$ relation of CV donors is virtually identical to that of isolated MS stars (Kolb, King & Baraffe 2001), with no significant dependence on age.

Table 2
The updated semi-empirical broken-power-law donor sequence for CVs.

$P_{orb}(hr)$	$M_2(M_\odot)$	$R_2(M_\odot)$	$T_{eff}(K)$	$\log g$	$\log L/L_\odot$	M_U	M_B	M_V	M_R	M_I	M_J	M_H	M_K	SpT
1.390	0.035	0.094	1115	5.036	28.67	35.88	30.01	25.97	21.51	18.55	14.60	14.71	14.63	T
1.387	0.040	0.098	1320	5.058	29.00	33.07	27.71	24.82	20.59	17.64	13.77	13.74	13.60	T
1.384	0.045	0.102	1537	5.077	29.30	31.24	25.99	23.49	19.42	16.51	13.00	12.88	12.81	T
1.382	0.050	0.105	1738	5.094	29.54	30.28	25.47	22.51	18.97	16.38	12.82	12.25	11.90	T
1.379	0.055	0.108	1934	5.110	29.75	28.80	24.46	21.28	18.19	15.77	12.28	11.56	11.07	L0.0
1.377	0.060	0.111	2110	5.125	29.93	27.45	23.25	20.52	17.82	15.34	11.82	11.13	10.71	M9.6
1.375	0.065	0.114	2265	5.138	30.07	25.76	21.64	19.51	17.42	14.87	11.31	10.64	10.32	M9.2
1.373	0.069	0.116	2377	5.148	30.17	24.41	20.64	18.71	16.89	14.40	11.04	10.39	10.08	M8.3
1.382	0.070	0.117	2402	5.146	30.20	24.08	20.43	18.52	16.74	14.28	10.98	10.33	10.02	M8.1
1.423	0.075	0.122	2520	5.140	30.32	22.62	19.44	17.63	16.01	13.71	10.72	10.08	9.76	M7.3
1.464	0.080	0.127	2618	5.133	30.42	21.49	18.65	16.92	15.41	13.23	10.50	9.87	9.55	M6.9
1.503	0.085	0.132	2699	5.127	30.50	20.58	18.01	16.34	14.91	12.84	10.31	9.69	9.38	M6.6
1.540	0.090	0.137	2768	5.122	30.58	19.89	17.50	15.87	14.50	12.52	10.15	9.54	9.23	M6.4
1.576	0.095	0.141	2827	5.116	30.64	19.31	17.07	15.47	14.15	12.25	10.01	9.41	9.09	M6.2
1.611	0.100	0.146	2877	5.111	30.70	18.83	16.71	15.14	13.86	12.02	9.89	9.29	8.97	M6.0
1.678	0.110	0.154	2957	5.102	30.80	18.11	16.15	14.62	13.39	11.65	9.67	9.08	8.77	M5.7
1.741	0.120	0.163	3020	5.094	30.88	17.56	15.71	14.21	13.03	11.36	9.49	8.90	8.59	M5.4
1.801	0.130	0.171	3069	5.086	30.95	17.14	15.37	13.89	12.74	11.13	9.33	8.74	8.44	M5.2
1.858	0.140	0.179	3115	5.078	31.02	16.76	15.06	13.59	12.47	10.92	9.18	8.60	8.30	M5.0
1.912	0.150	0.187	3160	5.072	31.08	16.39	14.76	13.31	12.22	10.71	9.04	8.46	8.17	M4.7
1.964	0.160	0.194	3200	5.065	31.14	16.07	14.50	13.06	11.99	10.53	8.92	8.34	8.05	M4.5
2.014	0.170	0.202	3227	5.059	31.18	15.86	14.32	12.89	11.84	10.40	8.81	8.23	7.95	M4.4
2.062	0.180	0.209	3250	5.054	31.23	15.67	14.15	12.73	11.69	10.27	8.71	8.13	7.85	M4.2
2.108	0.190	0.216	3272	5.048	31.27	15.49	13.99	12.58	11.55	10.16	8.61	8.04	7.76	M4.1
2.152	0.200	0.223	3290	5.043	31.30	15.33	13.85	12.45	11.43	10.05	8.53	7.96	7.67	M4.0
3.183	0.200	0.289	3300	4.817	31.53	14.64	13.23	11.89	10.87	9.49	7.95	7.37	7.09	M4.1
3.578	0.250	0.338	3372	4.779	31.71	14.03	12.66	11.34	10.35	9.02	7.54	6.96	6.69	M3.8
3.931	0.300	0.383	3428	4.747	31.85	13.55	12.20	10.90	9.94	8.64	7.20	6.63	6.37	M3.5
4.249	0.350	0.427	3489	4.721	31.97	13.12	11.79	10.50	9.57	8.30	6.91	6.33	6.08	M3.2
4.540	0.400	0.469	3550	4.698	32.08	12.75	11.42	10.14	9.23	8.00	6.65	6.07	5.83	M2.9
4.808	0.450	0.509	3614	4.678	32.18	12.41	11.07	9.80	8.91	7.72	6.41	5.82	5.60	M2.6
5.058	0.500	0.547	3690	4.660	32.28	12.08	10.72	9.46	8.58	7.44	6.18	5.58	5.38	M2.3
5.291	0.550	0.585	3790	4.644	32.39	11.74	10.34	9.08	8.23	7.16	5.95	5.33	5.15	M1.9
5.511	0.600	0.622	3911	4.629	32.49	11.39	9.93	8.67	7.85	6.86	5.72	5.07	4.93	M1.3
5.718	0.650	0.657	4055	4.615	32.61	10.99	9.48	8.22	7.42	6.55	5.49	4.84	4.72	M0.5
5.914	0.700	0.692	4204	4.603	32.71	10.55	9.01	7.77	7.01	6.24	5.26	4.63	4.53	K7.3

Note. — UBVRI magnitudes are given on the Johnson-Cousins system (Bessell 1990), JHK are given on the CIT system (Elias et al. 1982b,a). The sequence provided here is abbreviated. A more complete sequence, using steps of $0.001 M_\odot$ and including the far-infrared L (CIT), L' and M' (Mauna Kea) bands is available in electronic form.

stellar models. Second, we use a slightly updated set of stellar atmosphere grids to compute the photometric donor properties. More specifically, we use the standard NextGen atmosphere models (Hauschildt et al. 1999) down to $T_{eff} = 2300$ K, the AMES-DUSTY models (Chabrier et al. 2000) between $1800 \text{ K} \leq T_{eff} \leq 2000 \text{ K}$, and the AMES-COND models (Baraffe et al. 2003) for temperatures $T_{eff} \leq 1700 \text{ K}$. The transitions between these regimes are bridged by interpolation. See Section 5.4 for a brief discussion of the differences between the different types of atmosphere models.

A short version of the revised donor sequence is provided in Table 2; a more finely spaced version is available in electronic form. We defer a closer look at the physical and photometric properties along the sequence to Section 6.1. There, we will directly compare the old and new versions of the broken-power-law donor sequences to the donor properties suggested by our full evolution track. However, we note here already that the new version of the donor sequence should not be used for masses lower than $M_2 \simeq 0.05 M_\odot$, since the power-law approximation to the mass-radius relation probably breaks down in this regime (c.f. Figure 10).

Finally, here and throughout this paper, we have followed K06 in adopting a constant value of $M_1 = 0.75 M_\odot$ for the mass of a WD in a typical CV. In K06, we showed

that the mean WD mass among the eclipsing CV sample available at the time was $\langle M_1 \rangle = 0.75 \pm 0.05 M_\odot$, with no evidence for evolution in WD mass as a function of P_{orb} , but with a roughly 20% intrinsic dispersion ($\sigma_{int} = 0.16 M_\odot$). If we add the new data points from L08, there is still no evidence for evolution, but the mean WD mass increases slightly to $\langle M_1 \rangle = 0.79 \pm 0.03 M_\odot$. This is not significantly different from the earlier estimate, and, since we had already begun to assemble our grid of donor sequences and evolution tracks at the time of L08's publication, we chose to retain $M_1 = 0.75 M_\odot$ as a representative WD mass.

4. RECONSTRUCTING SECULAR EVOLUTION IN THE PRESENCE OF \dot{M}_2 FLUCTUATIONS

We noted in Section 1 that our donor-based method for reconstructing $\dot{M}_2(P_{orb})$ is likely to yield *secular* mass-transfer rates. This is a key advantage, since the mass-transfer and accretion rate in a CV can vary on a wide range of time scales. As long as the variability time scale, τ_{var} , is shorter than the evolutionary time scale, $\tau_{ev} \simeq \dot{J}/J \simeq \dot{M}_2/M_2$, these fluctuations will not significantly affect the system's overall evolution. However, they can confound observational tracers of \dot{M}_2 that track the mean mass-transfer or accretion rate on time scales $\lesssim \tau_{var}$.

The possible existence of mass-transfer-rate fluctua-

tions on unobservably long time scales has been widely discussed in the CV community. In this section, we will explain the origin of this idea, briefly discuss the main mechanisms that could produce such fluctuations, compare the variability time scales associated with these mechanisms to the averaging time scales of several observational tracers of \dot{M}_2 , and finally assess the evidence for such fluctuations in the light of the latest data.

4.1. The Historical Case for Long-Term \dot{M}_2 Fluctuations

The first attempts to estimate CV mass-transfer rates found substantial scatter in the inferred average \dot{M}_2 values at given P_{orb} , especially above the period gap (Patterson 1984; Warner 1987). These studies used time-averaged accretion light as a tracer of \dot{M}_2 (see Section 4.3.1), but additional evidence for significant scatter in the present-day mass-transfer rates at fixed P_{orb} appeared to come from the co-existence of dwarf novae and nova-likes at orbital periods above the gap. According to the disk instability model for dwarf nova eruptions (e.g. Osaki 1996; Lasota 2001), these CV sub-classes are differentiated primarily by the rate at which mass is supplied to the accretion disk. If all CVs follow a unique evolution track, one might therefore expect CV sub-types to populate distinct period ranges. Taken at face value, scatter in sub-types must therefore reflect scatter in $\dot{M}_2(P_{orb})$ (but see Section 7.2 for a more detailed look at this issue).

Such observationally inferred dispersion in $\dot{M}_2(P_{orb})$ is unlikely to reflect a real spread in the *secular* mass-transfer rates within the CV population. Theoretically, all CVs with initially unevolved donors are expected to quickly join onto a *unique* evolution track, whose properties are determined solely by the mechanism for AML from the system (Paczynski & Sienkiewicz 1983; Ritter & Kolb 1992; Kolb 1993; Stehle et al. 1996). Empirically, a unique track is also necessary in order to explain the existence of a period gap with sharp edges and a well-defined minimum period. The observed scatter in \dot{M}_2 was therefore quickly interpreted as evidence for mass-transfer-rate fluctuations on unobservably long time scales, but still satisfying $\tau_{var} \ll \tau_{ev}$ (Verbunt 1984; Hameury et al. 1989).

4.2. Physical Causes of Long-Term \dot{M}_2 Fluctuations

How could such fluctuations be produced? The mass-loss rate from the donor depends exponentially on the distance between the stellar radius and the Roche lobe (Ritter 1988)

$$\dot{M}_2 = \dot{M}_0 \exp^{-\frac{\Delta R}{H}}, \quad (18)$$

where $\Delta R = R_L - R_2$, and $H \simeq 10^{-4} R_2$ is the scale height near R_2 . Quite generally, fluctuations in \dot{M}_2 may therefore be associated with variations in H and/or changes in ΔR .

Fluctuations in \dot{M}_2 driven by spatial and/or temporal variations in H are, in fact, likely to occur. However, their time scales are much shorter than we are interested in here. For example, the strongly magnetic polars, which lack an accretion disk entirely, exhibit high- and low-state behaviour with characteristic time scales

of weeks to years (e.g. Hessman et al. 2000; Kafka & Honeycutt 2005). These low states may well be linked to the L_1 point becoming covered by star spots. This can quench \dot{M}_2 , because star spots are characterized by lower H than the surrounding photospheric regions (Livio & Pringle 1994; King & Cannizzo 1998, but also see Howell et al. 2000). Similarly, there is some observational evidence that the mass-transfer rate from the secondary may be enhanced during dwarf nova eruptions (Patterson et al. 2002; Steeghs 2004; Smak 2004a). This may be due to irradiation-driven heating of the upper atmospheric layers in the donor star, causing an increase in H and hence \dot{M}_2 (Smak 2004b,c; but also see Osaki & Meyer 2003, 2004). However, neither of these types of variations occur on the long time scales relevant to us here. In fact, the longest plausible time scale on which H variations may be driven is probably that of magnetic activity cycles. Even this is “only” on the order of years and therefore still accessible to observations.

The only promising way to produce unobservably slow fluctuations in \dot{M}_2 is therefore to invoke variations in ΔR . Such variations might be driven by changes in either R_2 or R_L . The only two mechanisms that have been considered in any detail in this context – irradiation-driven \dot{M}_2 cycles and nova-induced hibernation – can, in fact, be distinguished along these lines.

4.2.1. Varying R_2 : Irradiation-Driven Mass-Transfer Rate Fluctuations

It can be shown on fairly general grounds that a long-term limit cycle on the basis of stellar radius variations is possible, provided the donor’s thermal relaxation time scale depends explicitly on \dot{M}_2 (King et al. 1995, 1996). The only obvious physical mechanism for producing such a coupling is irradiation.

A full discussion of the finer details of irradiation-driven mass-transfer cycles is far beyond the scope of the present study. Such discussions are provided by King et al. (1995, 1996); Ritter et al. (1995, 1996); Wu et al. (1995b,a); McCormick & Frank (1998); Ritter et al. (2000); King (2000) and most recently Büning & Ritter (2004, hereafter BR04). For our present purposes, the two questions that really matter are: (i) on what time scale are such cycles expected to be driven?; (ii) what is the amplitude of the R_2 variations expected during these cycles?

Let us start with the first question. In order to produce significant fluctuations in \dot{M}_2 , ΔR must fluctuate by at least H . Moreover, the low states of these cycles correspond to an (almost) detached state, which is terminated when the Roche lobe catches up with the stellar radius again. Thus a firm lower limit on the time scale of such cycles is given by the time it takes the Roche lobe to move through H in the absence of any mass loss. This is given by (e.g. King & Kolb 1995)

$$\tau_h \simeq \frac{H}{R_2} \frac{J}{2\dot{J}}. \quad (19)$$

In order to obtain a more realistic estimate of the cycle time scale, we need to answer the second question. As we will show in Section 5.2.3, irradiation in CVs is only capable of inflating donor radii by $\simeq 1\%$. For mass-transfer cycles driven by irradiation, this is then also a

rough estimate of the amplitude of the radius variations the donor experiences during these cycles, i.e. $\delta R/R_2 \simeq 0.01$.¹³ A more realistic estimate of the duration of mass transfer cycles is therefore

$$\tau_{\delta R} \simeq \frac{\delta R}{R} \frac{J}{2\dot{J}}. \quad (20)$$

Finally, an independent estimate of the time scale associated with irradiation-driven mass-transfer cycles is provided by BR04. They show that *low-amplitude* cycles are expected to have characteristic time scales of

$$\tau_{bh} \simeq 2\pi \left(\frac{H}{R_2} \frac{J}{\dot{J}} \frac{\tau_{CE}}{10} \right)^{0.5}, \quad (21)$$

where τ_{CE} is the thermal time scale of the convective envelope of the donor. This depends primarily on the mass of the convective envelope, M_{CE} , and the thermal time scale of the undisturbed star, $\tau_{kh,eq}$, and is given explicitly by

$$\tau_{CE} \simeq \frac{3}{7} \frac{M_{CE}}{M_2} \tau_{kh,eq}. \quad (22)$$

For reference, in our standard model sequence, M_{CE} can be approximated roughly by

$$M_{CE} \simeq M_2 - \exp^{-(3M_2+0.75)} \quad (23)$$

across most of the mass range above the period gap. Note that τ_{bh} is really a lower limit, since it only refers to low-amplitude cycles. The numerical examples in BR04 show that large-amplitude cycles are characterized by longer time scales.

As noted above, the donor radius fluctuates by only $\simeq 1\%$ across the full mass-transfer cycle. This is a small fluctuation on top of the larger radius increase that is due to the secular \dot{M}_2 . After all, the donor must be $\simeq 30\%$ inflated at the upper edge of the gap (Section 2.3.2). Thus, as advertised above, mass-transfer rates inferred from donor radii should remain largely unaffected by such cycles.

This last statement comes with some fine print. A key problem with irradiation-driven cycles is that CVs with donor masses $M_2 \lesssim 0.65M_\odot$ – i.e. essentially all the CVs we are interested in – are not susceptible to the instability that produces these cycles (e.g. King et al. 1996; Ritter et al. 2000; BR04). However, it has been shown that the combination of irradiation-driving with CAML (King & Kolb 1995) can destabilize CVs with lower donor masses, even possibly including systems below the period gap (e.g. King et al. 1996; McCormick & Frank 1998; Ritter et al. 2000; BR04). It is not obvious to us whether CAML-assisted irradiation-driven cycles would necessarily also show only small radius excursions. In the low state of such a cycle, the AML is reduced (because

the “consequential” part of it depends, by definition, on \dot{M}_2). But the AML time scale also sets the time scale for Roche-lobe shrinkage in the detached state. It is therefore conceivable that some models of CAML-assisted cycles could predict considerably longer low states – perhaps long enough to allow significant shrinkage of the donor. If so, then radius measurements of active CVs, would trace the average high-state \dot{M}_2 , rather than the secular value. Note, however, that even the standard interpretation of the period gap itself would have to be modified in this case. The gap width, for example, would reflect only the high-state properties of donors above and below the gap in such a scenario. If the cycle time scale were comparable to the evolutionary time scale, it would also become difficult to explain the sharpness of the period gap and the period minimum.

4.2.2. Varying R_L : Nova-Induced Cycles and Hibernation

The second way to drive long-term \dot{M}_2 fluctuations in CVs is via cyclic variations in the Roche-lobe radius, R_L (which must be superposed on the slow evolutionary changes in R_L). There is really just one obvious recurring event in the life of a CV that might produce such variations: a nova eruption.

The idea that nova eruptions might explain the large inferred scatter in \dot{M}_2 at fixed P_{orb} was first put forward by MacDonald (1986). He argued that the dominant effect of these eruptions would be to *reduce* the size of the binary orbit. More specifically, he suggested that during a nova eruption, the binary would effectively orbit inside a common envelope composed of material lifted off the WD surface. This material would therefore be frictionally heated, spun up, and ejected, with the energy and AML associated with this process being drained from the binary orbit. The dominant effect on binary evolution in this picture is *frictional angular momentum loss* (FAML). This shrinks the binary orbit and, with it, the Roche lobe. MacDonald’s theory therefore predicts that novae should exhibit enhanced mass-transfer rates in the aftermath of nova eruptions.

At almost the same time, Shara et al. (1986) presented a completely different take on the same basic idea. In effect, they argued that the dominant effect of the nova eruption is the removal of *mass* from the binary system (not the removal of angular momentum). In this case, the orbit (and the Roche lobe) must *expand* in the aftermath of an eruption, leaving the secondary temporarily in detached (or almost detached) low state. Thus Shara et al. (1986) suggested that most CV may “hibernate” for most of the time between nova eruptions.

As with irradiation-induced mass-transfer cycles, a full discussion of nova-induced mass-transfer cycles and hibernation is beyond the scope of the present study. The effect of nova eruptions on binary parameters is examined in Livio & Shara (1987) and Livio et al. (1991), while Schaefer & Patterson (1983) and Martin et al. (2010) discuss attempts to measure this effect directly. The observational case *for* hibernation is presented in Vogt (1990); Duerbeck (1992) and Schmidtobreick et al. (2005), while the observational case *against* is made by Naylor et al. (1992); Weight et al. (1994); Somers et al. (1996) and Thomas et al. (2008). Finally, the impact of nova-induced \dot{M}_2 fluctuations on long-term CV evo-

¹³ Note that the donor does not relax all the way back to its thermal equilibrium radius during the low states, because the lobe catches up with the stellar radius well before this can happen. This is also why a significant ($\gtrsim 5\times$) reduction in the AML rate is needed in the disrupted MB braking model in order to produce a period gap of the observed width. Without such a reduction, the Roche lobe would catch up with the donor before it has relaxed all the way back to its thermal equilibrium radius. The result would be a premature emergence from the gap, i.e. a gap of insufficient width.

lution has been studied by Schenker et al. (1998) and Kolb et al. (2001b). A comprehensive review of nova theory and observations, including hibernation, is given by Shara (1989), while a very readable introduction and take-off point for further study is provided by Warner (2006).

Here, we simply wish to know on what time scale nova eruptions might cause \dot{M}_2 to fluctuate. This is fairly easy to answer: the relevant time scale is simply the nova recurrence time, which can be calculated from nova models as

$$\tau_{nova} \simeq \frac{M_{ign}}{\dot{M}_{acc}}. \quad (24)$$

Here, \dot{M}_{acc} is the accretion rate onto the WD, averaged over the nova cycle. If nova eruptions are the only cause of long-term variability, we can take $\dot{M}_{acc} = \dot{M}_2$, where, as usual, \dot{M}_2 is the secular mass-transfer rate. The nova ignition mass, M_{ign} , is the critical mass of the accreted envelope on the WD above which a thermonuclear runaway is triggered. M_{ign} depends primarily on three parameters: (i) the accretion rate, \dot{M}_{acc} ; (ii) the WD mass, M_1 ; and (iii) the WD core temperature, $T_{wd,c}$. In a CV, the equilibrium WD core temperature is set by the compressional release of energy associated with accretion and is therefore itself a function of M_1 and \dot{M}_{acc} (Townesley & Bildsten 2004).¹⁴

Strictly speaking, τ_{nova} is clearly an upper limit on the time scale associated with nova-induced mass-transfer rate cycles. However, at least for the most popular incarnation of such cycles – hibernation – it is easy to see that the actual time scale cannot be much less than this. Suppose, for example, that hibernation causes complete detachment of the donor from the Roche lobe, but that this detached state lasts for only 1% of the nova recurrence time. In this case, the mass-transfer rate in the “high state” would, by definition, be just 1% above the secular mean. Similarly, the space density of active CVs would amount to a full 99% of the intrinsic CV space density. Relaxing the assumption of complete detachment makes little difference: there is then a wider range of possible \dot{M}_2 values at fixed P_{orb} , but 99% of the active CV population would have \dot{M}_2 within better than 1% of the secular mean. This shows that in order to have any significant effect on our understanding of CV evolution at all, the hibernating phase must take up a large fraction of the nova cycle.

A rough lower limit on the time scale associated with hibernation cycles is once again provided by τ_h (Equation 19). After all, if the system is detached in the hibernating state, the Roche lobe has to have time to catch up to the stellar radius again before the next nova eruption.

4.3. Averaging Time Scales Associated with Observational Tracers of \dot{M}_2

Let us now take a look at the different observables that can be used to estimate \dot{M}_2 , focusing particularly on the time scale over which they effectively average the mass-transfer rate.

¹⁴ The WDs in long-period CVs actually may not have time to fully equilibrate, but Townesley & Bildsten (2005) argue that M_{ign} becomes insensitive to \dot{M}_{acc} in this parameter regime anyway.

4.3.1. Accretion Light

The most straightforward tracer of a CV’s mass-transfer rate is its brightness. To first order, this is primarily a measure of the accretion luminosity, $L_{acc} \simeq GM_1\dot{M}_{acc}/R$, and thus of the accretion rate through the disk and onto the WD, \dot{M}_{acc} . This can vary dramatically in a CV. For example, in a dwarf nova, \dot{M}_{acc} changes by orders of magnitude over the outburst cycle. If the full time scale of such variations is covered and resolved observationally – as is true for many, but not all dwarf nova cycles – one can attempt to average over this variability. The relevant averaging time-scale associated with the use of accretion light as a tracer of \dot{M}_2 is therefore simply the length of the observational record. A typical number for this might be $\tau_{obs} \sim 10$ yrs.

4.3.2. White Dwarf Temperatures

Another promising method to estimate \dot{M}_2 is based on the quiescent effective temperature of the accreting WD in a CV (Townesley & Bildsten 2002, 2003, 2004; Townesley & Gänsicke 2009). This is set primarily by the mean accretion rate over the last thermal time scale of the non-degenerate layer on the WD surface (Townesley & Bildsten 2003)

$$\tau_{wd} \simeq 10^4 \left(\frac{\dot{M}_{acc}}{10^{-10} M_{\odot} \text{yr}^{-1}} \right)^{-3/4} \text{ yrs}, \quad (25)$$

for a $M = 0.8M_{\odot}$ WD.

4.3.3. Donor Radii

The method adopted in the present study is to infer \dot{M}_2 from the mass-loss-induced bloating of the donor radii in CVs. As already discussed in Section 2.2.2, the time scale on which a CV secondary is able to adjust its radius to the prevailing mass-loss rate from its surface is given by $\tau_{adj} \simeq 0.05\tau_{kh,eq}$ (Equation 8; Stehle et al. 1996).

4.4. A Direct Comparison of Variability and Observational Averaging Time Scales

We now have estimates for the time scales on which long-term \dot{M}_2 fluctuations may be driven, and also for the effective averaging time scales associated with different observational tracers of \dot{M}_2 . How do these time scales compare?

Figure 5 shows all the time-scale estimates we arrived at in the previous sections as a function of P_{orb} . All of these curves have been calculated for a CV evolving according to the standard model. In the case of τ_{nova} , we estimated appropriate ignition masses for $M_1 = 0.75M_{\odot}$ by interpolating on the calculations shown in Figure 8 of Townesley & Bildsten (2004).

As one might expect, τ_{obs} is by far the shortest of all of these time scales. Thus accretion light will only yield reliable estimates of secular mass-transfer rates if long-term cycles do not exist at all. However, τ_{wd} is also about an order of magnitude faster than even τ_h , which is quite a firm lower limit on any likely cycle time scale.

Strictly speaking, if $\tau_{var} > \tau_{wd}$, τ_{wd} itself will vary with the varying \dot{M}_{acc} . Thus τ_{wd} will be much longer in the low state of a cycle than in the high state, an effect

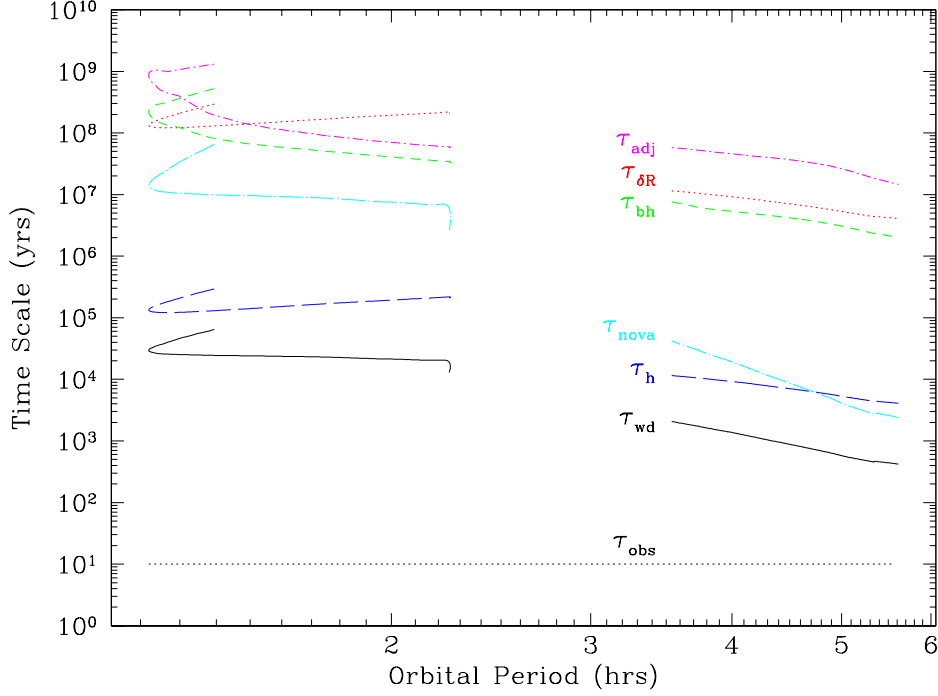


Figure 5. Several key time scales as calculated along a standard-model CV evolution track. The thick solid black horizontal line at the bottom of the plot marks $\tau_{\text{obs}} = 10$ yrs, which is a rough estimate of the typical averaging time scale associated with mass-transfer-rate estimates based on accretion luminosity (see Section 4.3.1). The thin solid black line shows the thermal time scale of the non-degenerate surface layer on the accreting WD, τ_{wd} (Equation 25). This is roughly the averaging time scale for mass-transfer-rate estimates based on (quiescent) WD effective temperatures. The long-dashed blue line corresponds to the time it takes the Roche lobe to move through one scale height in the donor’s atmosphere, τ_H (Equation 19). This is the shortest possible time scale for mass-transfer-rate fluctuations driven by donor radius changes. The remaining three curves show several more realistic estimates of the time scale for long-term mass-transfer rate fluctuations: τ_{bh} (Equation 21; green short-dashed line), $\tau_{\delta R}$ (Equation 20; red dotted line) and τ_{adj} (Equation 8; magenta dash-dotted line).

that is not taken into account in Figure 5. Perhaps as a result of this, τ_{wd} may perform slightly better than suggested by Figure 5. The detailed calculations presented in Townsley & Gänsicke (2009, hereafter TG09) show, for example, that if \dot{M}_{acc} were to vary by a factor of 9 with a period of 8×10^4 yrs around a secular mean of $\dot{M}_2 = 5 \times 10^{-11} M_{\odot} \text{ yr}^{-1}$ (i.e. a variation between $\dot{M}_2 = 1 \times 10^{-11} M_{\odot} \text{ yr}^{-1}$ and $\dot{M}_2 = 9 \times 10^{-11} M_{\odot} \text{ yr}^{-1}$), the quiescent WD luminosity – and hence the inferred \dot{M}_2 – would fluctuate by a factor 2-3 over the course of this cycle.

In any case, Figure 5 shows that if mass-transfer rate fluctuations exist at all in CVs, their time scale could be very long indeed: $10^6 - 10^9$ yrs for irradiation-driven cycles, and $10^4 - 10^8$ yrs for nova-induced variations.¹⁵ Neither accretion light nor WD temperatures can be expected to yield reliable estimates of secular \dot{M}_2 if either mechanism drives large-amplitude accretion-rate variations over a large fraction of a CV’s life.

Finally, what about donor radii? Figure 5 shows that τ_{adj} is comparable to our estimates for the time scale associated with irradiation-driven cycles. This is as expected, since τ_{adj} can actually itself be thought of as an

estimate of (or limit on) the time scale of such cycles. After all, τ_{adj} is a measure of the time it takes the stellar radius to adjust to the changing \dot{M}_2 across the cycle. However, as explained in Section 4.2.1, donor radii are nevertheless likely to trace the secular \dot{M}_2 in this case, because the donor radius variations that drive these cycles are much smaller than the mass-loss-induced donor bloating. In the case of hibernation, there is no worry at all: τ_{adj} is comfortably longer than τ_{nova} at all orbital periods.

4.4.1. The Observational Case for Long-Term \dot{M}_2 Fluctuations: An Update

Having spent so much time discussing the theory and implications of mass-transfer cycles, let us provide a brief update on the observational evidence for their existence. The most recent compilations of empirical \dot{M}_2 tracers are contained in TG09, which is based on the WD effective temperature, and in Patterson (2009), which is based on the time-averaged accretion disk luminosity. Let us first consider long-period systems. These are not included in Patterson’s study at all, and only a handful are contained in TG09. Those few points do seem to show quite significant scatter, although this is mainly driven by just three objects. All of these have exceptionally high inferred accretion rates, and all are located in the period range 3 hrs - 4 hrs (see their Figure 5 and also Figure 16 in Section 6.4). This *might* be evidence for mass-transfer-rate

¹⁵ The fact that τ_{nova} and τ_h cross at the longest periods suggests that it is not quite self-consistent to assume that nova-induced hibernation would leave the secular mean \dot{M}_2 unaffected in this case.

fluctuations above the period gap.

Below the gap, there is still some scatter in the WD-based \dot{M}_2 estimates, but the error bars are also large. More importantly, however, it seems possible that much or all of the scatter could be due to within-sample variations in white dwarf mass and the mass of the non-degenerate layer on the WD surface (see Section 4). The time-averaged absolute magnitudes, M_V , presented in Patterson (2009) show considerable variation as well, by about 1 mag at fixed P_{orb} . However, the systematic uncertainties affecting these M_V estimates are also quite large, so it is hard to assess whether this really provides evidence for long-term mass-transfer cycles below the gap.

Finally, what about the co-existence of dwarf novae and nova-likes at the same orbital period? The current data on this is presented and interpreted in more detail in Section 7.2. It turns out that this may provide *some* evidence for \dot{M}_2 fluctuations above the gap, although it would probably not be compelling in its own right. Overall, we think the latest data provide marginally convincing evidence for long-term mass-transfer-rate variations above the period gap. Below the gap, it is unclear whether such cycles are needed to explain the observations.

5. CV EVOLUTION FROM DONOR PROPERTIES

Let us remind ourselves of our main goal. We wish to construct a complete evolution track for CVs based solely on the observed properties of their donor stars. This is possible because mass loss on a time scale comparable to the donor’s thermal time scale will lead to a moderate expansion of the star. Thus the degree by which a donor is bloated (relative to an equal-mass MS star) can be used as a tracer of the rate at which it is losing mass.

In this section, we will first deal with several effects other than mass loss that might make Roche-lobe-filling CV secondaries appear larger than models of ordinary MS stars would predict (Section 5.2). We will then describe how we actually construct our final evolution track by fitting self-consistent models of mass-losing stars to the observational data (Sections 5.3 and 5.4).

5.1. Overview of the Method

The key challenge in reconstructing CV evolution from donor properties is to obtain a reliable calibration of the relationship between \dot{M}_2 and observed donor inflation. In principle, this relationship can be provided entirely by stellar models, and this is indeed the backbone of our method. However, in practice, two obstacles must be overcome. First, there are several effects other than mass loss that might make Roche-lobe-filling CV secondaries appear larger than models of ordinary MS stars would predict. We will deal with these effects in Section 5.2.

Second, as explained in Section 2.2.2, donor bloating is not strictly a measure of the instantaneous \dot{M}_2 , but is also somewhat sensitive to the mass-loss *history* of the donor. Unfortunately, it is too computationally expensive to calculate full stellar model evolution sequences for the ML histories corresponding to all plausible AML recipes. We therefore use an approximate method to first determine a suitable functional form and approximate normalization for \dot{J}_{sys} ; this is briefly described in

Section 5.3. Once this form is fixed, self-consistent model sequences can be used to determine its optimal normalization and evaluate the goodness-of-fit to the data. The resulting CV evolution track can then again be coupled to stellar atmosphere models to simultaneously provide a complete set of photometric donor properties. These final steps are explained in Section 5.4.

5.2. Apparent Donor Bloating Unrelated to Mass Loss

There are at least three questions that need to be addressed before the radii predicted by stellar structure models can be applied to CV donor stars. First, to what extent are these models capable of accounting for the observed radii of *isolated* low-mass stars? Second, what is the net effect of tidal and rotational deformation on the radii of semi-detached donor stars? Third, could irradiation cause significant radius inflation in CV secondaries?

5.2.1. Larger-Than-Expected Radii in Non-Interacting Low-Mass Stars

Over the last few years, it has become increasingly clear that the empirically-inferred radii of at least some lower-MS stars are significantly larger than predicted by stellar structure models (by up to 30% in extreme cases; see López-Morales 2007 for a fairly recent overview). If we are going to use such models to infer mass-loss rates from observed donor radii, this discrepancy clearly needs to be taken into account.

In order to test and calibrate the BCAH98 models we are using, we have compiled our own, fairly comprehensive list of empirically determined masses and radii for lower MS stars. This is given in Appendix B. The resulting empirical mass-radius relation is shown in Figure 6, along with a standard 5 Gyr BCAH98 MS track.

Figure 6 confirms that at least some lower-MS stars have radii significantly in excess of the standard BCAH98 model prediction. However, it also reveals two other important points. First, there is no evidence that *all* observational radii are larger than predicted. Instead, it appears that there is considerable radius *scatter* in the $M - R$ relation, with some stars falling quite close to the model track, but others lying well above it. This finding mirrors that of Beuermann (2006), who dubbed those stars found close to the theoretical MS “immaculate dwarfs”.

Second, it is striking that fully convective stars appear to be much closer to the model predictions, on average, and exhibit much less radius scatter, than stars with a radiative core. A hint along these lines had first been noted by Ribas (2006) and López-Morales (2007), but our larger data base here allows us to confirm and quantify this impression. In particular, we can directly estimate the average fractional radius excess, $\langle f_R \rangle$ and the intrinsic dispersion around this excess, σ_{int} , both above and below the fully convective limit ($\simeq 0.35M_\odot$). We take the errors on mass and radius to be uncorrelated and thus estimate $\langle f_R \rangle$ and σ_{int} by minimizing the χ^2 -statistic

$$\chi^2 = \sum_{i=1}^{N_{data}} \frac{\log R_{data,i} - \log f_R R_{model,i}}{\sigma_{\log R_{data,i}}^2 + \sigma_{int}^2} + \frac{\log M_{data,i} - \log M_{model,i}}{\sigma_{\log M_{data,i}}^2} \quad (26)$$

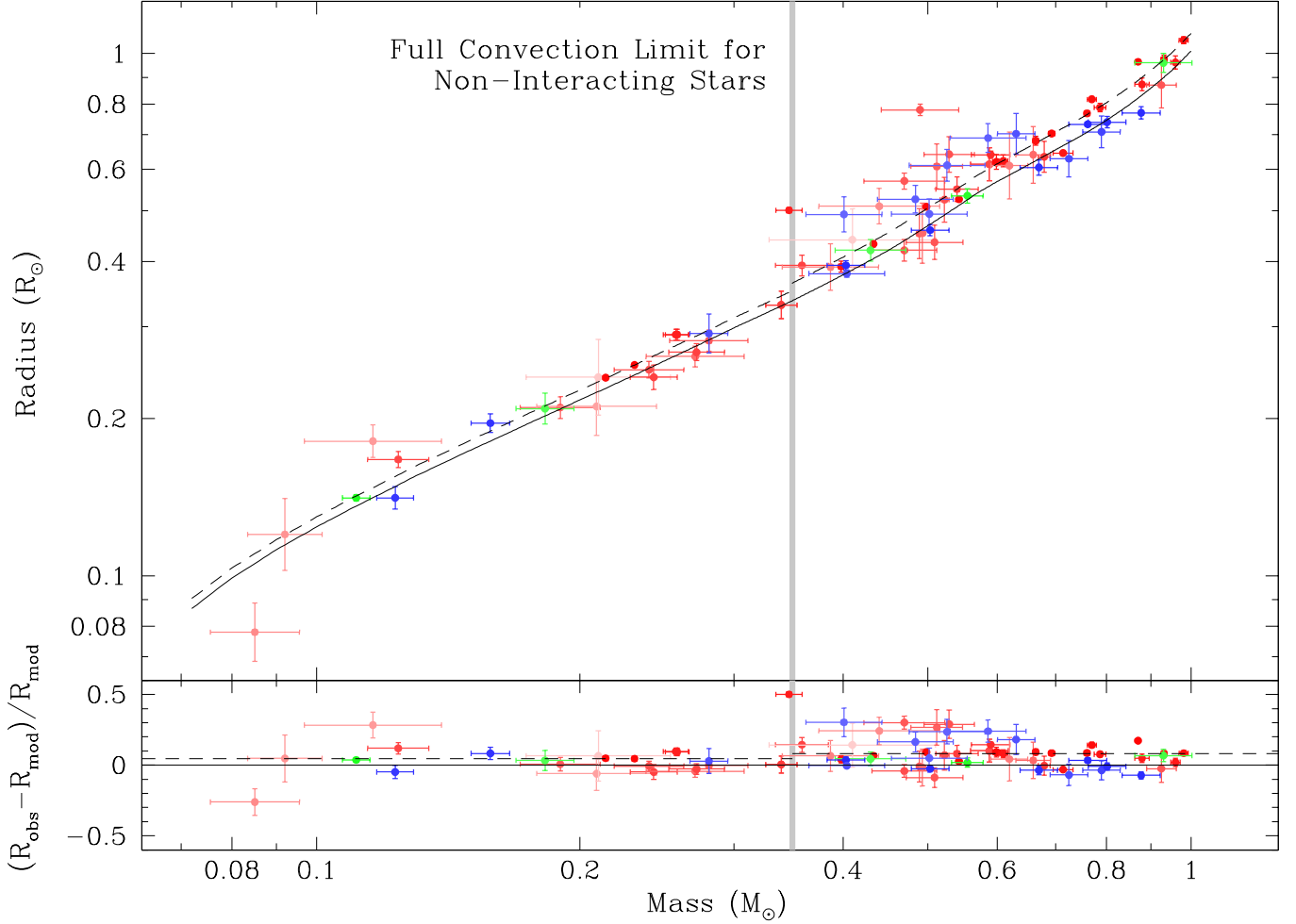


Figure 6. *Top panel:* The mass-radius relationship of non-interacting low-mass stars. Points and errors are based on the observational data listed in Table B1. Different colours correspond to different types of objects: single stars are shown in blue, stars in binaries with WD companions are plotted in green; stars in other binaries are shown in red. Observations with larger errors bars are plotted with slightly lighter/fainter colours. The solid black line shows the predicted mass-radius relation at 5 Gyr from BCAH98. The dashed black lines show the same sequence after re-scaling it slightly to optimally match the data. The re-scaling is done independently for fully convective and partially radiative stars and amounts to 4.5% and 7.9% adjustments, respectively. *Bottom panel:* Residuals of the data points with respect to predicted mass-radius relationship. The dashed lines once again show the optimal re-scalings. The vertical grey line in both panels marks the dividing line between fully convective and partially radiative stars ($0.35 M_{\odot}$; Chabrier & Baraffe 1997).

with respect to f_R , while adjusting the intrinsic dispersion so that $\chi^2_{\nu} = \chi^2 / (N_{data} - 1) = 1$ for the best estimate. In evaluating Equation 26, we take the model point ($\log M_{model,i}$, $f_R R_{model,i}$) associated with the i -th data point to be that closest to it in χ^2 sense (i.e. that which minimizes this datum’s contribution to the total χ^2).

For stars with radiative cores and masses below $0.7 M_{\odot}$ (the regime relevant to unevolved, long-period CV donors), we obtain $\langle f_R \rangle = 1.079 \pm 0.012$ with $\sigma_{int} = 0.022$ dex (equivalent to a 5% dispersion). However, for fully convective stars, we find a much smaller average radius excess, $\langle f_R \rangle = 1.045 \pm 0.005$, with no need for any intrinsic dispersion ($\chi^2_{\nu} = 0.79$ with $\sigma_{int} = 0$). Note that the one data point virtually *on* the fully convective boundary has been excluded from both estimates.

These numbers agree fairly well with those found in

the recent study by Morales et al. (2010). Based on their own compilation of mass-radius measurements, Morales et al. (2010) estimated $f_R = 1.081$ with $\sigma_{int} = 12.2\%$ for partially radiative stars, and $f_R = 1.057$ with $\sigma_{int} = 3.1\%$ for fully convective stars. The slight differences between their numbers and ours – especially with respect to the intrinsic dispersions – are probably due to somewhat different samples and statistical methods being adopted in the two analyses. For example, had we ignored the mass uncertainties, or assumed them to be strongly positively correlated with the radius errors, our intrinsic dispersion estimates would also have been somewhat larger.

The evidence for intrinsic radius scatter among (at least) stars with a radiative core suggests that there are one or more hidden parameters that determine if a particular star is “immaculate” (radius close to the expected

value) or not. The two most promising candidates for such parameters are starspot coverage and convective efficiency (Chabrier et al. 2007). More specifically, both a very high starspot covering fraction and a reduced convective efficiency in the stellar envelope can decrease the heat flux from the stellar interior and thus lead to a swelling of the star. The underlying cause of reduced convective efficiency could be either fast rotation and/or a strong magnetic field.

Chabrier et al. (2007) explored both of these possibilities, with findings that may be relevant to CV donors (c.f. L08). In particular, it turns out that reduced convective efficiency has only a modest effect on fully convective stars, whereas spot coverage affects stars with and without a radiative core in a broadly similar way. This suggests that slight radius excesses among fully convective stars may be due to spot coverage, whereas the considerably larger excesses seen in stars with radiative cores may be primarily due to reduced convective efficiency. It is also easy to account for the observed radius scatter in this picture, since the efficiency of convective energy transport will depend on factors that vary from star to star (e.g. rotation and magnetic field strength).

A quantitative analysis of these ideas has recently been carried out by Morales et al. (2010). Crucially, their study also considered whether some of the inferred radius excesses may be artifacts of the way in which the radii were estimated. Most of the precise radius estimates for low-mass stars to date – particularly those for fully convective stars – are based on light curve analyses of eclipsing binary systems. The results of such analyses can be sensitive to asymmetries in the surface brightness distribution across the stellar surface. Of particular concern here are high-latitude or polar star spots, which are common amongst active stars (e.g. Hussain 2004). The application of standard eclipse analyses to light curves affected by polar spots will tend to overestimate the stellar radii. The main finding of Morales et al. (2010) is that the observed radius excesses are probably due to all three factors: (i) observational radius estimates derived from eclipsing binaries are probably overestimated by $\simeq 3\%$ (actually between 0% and 6%) due to the effect of polar spots; (ii) the effect of star spots on the outward heat flux accounts for $\simeq 3\%$ of the observed differences; (iii) reduced convective efficiency accounts for any remaining excess (0% – 4%).

The results of Chabrier et al. (2007) and Morales et al. (2010) suggest a simple, physically motivated calibration for our theoretical donor models. Following Morales et al. (2010), we assume that the average radius excesses inferred above need to be corrected downward to account for the 3% bias associated with polar spots. This leaves us with a physical excess of 1.5% for fully convective stars (which is probably driven by star-spot-induced suppression of outward heat flux) and an excess of 4.9% for partially radiative stars (which is probably driven by both star spots and a reduced convective efficiency due to rotation and/or magnetic fields). We can therefore apply these correction factors to our theoretical donor models, i.e. we will adjust the predicted radii upward by a factor $f_R = 1.015$ below the gap and $f_R = 1.049$ above.

There are, of course, systematic uncertainties associated with this calibration. For example, CV donors are faster rotators than most of the stars in our calibration

sample. This might matter, because fast rotation could be linked to all of the physical mechanisms that may drive stellar inflation unrelated to mass loss (Chabrier et al. 2007): it may directly suppress convection, it may produce stronger magnetic fields, and it may also produce higher star spot coverage. If so, then the radii of CV donors might be more inflated than those of the stars in our calibration sample.

There is not enough observational data on CV donors to test this idea directly. For example, there is very little evidence for even the presence or absence of star spots on CV secondaries. Webb et al. (2002) spectroscopically inferred a spot coverage of $\simeq 20\%$ for the donor in SS Cyg, but the likely nuclear-evolved nature of this star (Bitner et al. 2007) makes it an unreliable calibration point for our purposes. Similarly, Roche tomography has been used to detect star spots in the donor stars of AE Aqr (Watson et al. 2006), BV Cen (Watson et al. 2007b) and V426 Oph (Watson et al. 2007a), but one of these is a strongly magnetic system (AE Aqr) and at least one of the others contains an evolved donor (BV Cen). The only application of Roche tomography to a fully convective donor is presented by Beuermann & Reinsch (2008) for the magnetic system EX Hya. Their analysis reveals evidence of irradiation, but not of star spots or chromospheric emission.

Fortunately, however, our calibration sample does actually include a few synchronously rotating stars in very short-period binaries. These do not support the idea that such stars exhibit massively larger inflation. For example, the fully convective secondaries in the pre-CVs NN Ser ($P_{orb} \simeq 3.1$ hrs; Parsons et al. 2010) and RR Cae ($P_{orb} \simeq 7.3$ hrs; Maxted et al. 2007) both exhibit rather modest radius excesses between 3% and 4%, quite consistent with other fully convective stars in the calibration sample. In the absence of evidence to the contrary, the best we can do is assume that the calibration factors derived from our detached star sample will apply to CVs donors as well. The systematic uncertainties associated with this assumption will need to be explored, however, and we will do so in Section 8.3.

5.2.2. Tidal and Rotational Deformation

CV secondaries are not spherical. More specifically, the critical equipotential surface that defines the outer boundary of a Roche-lobe-filling star is distorted into the well-known “tear-drop” shape by strong tidal and rotational forces. This is a key difference between CV donors and isolated MS stars. In practice, this difference is usually ignored, and the donors are treated as spherical objects with radius equal to the volume-averaged Roche-lobe radius, R_L , i.e. the radius of a sphere with the same volume as the lobe. Both Equations 11 and 15 are numerical approximations for R_L . Moreover, it is usually assumed that the *equilibrium* radius of the star is unaffected by its distorted shape.

For many purposes, this treatment is sufficient. However, our goal here is to use the modest amounts of donor bloating induced by mass loss to infer \dot{M}_2 . Moreover, all of the stellar models we will use to accomplish this are purely 1-dimensional, i.e. spherical and non-rotating. In this context, it is clearly important to check whether the distorted shape of the donor may affect its equilibrium radius. The precise question we need to answer is

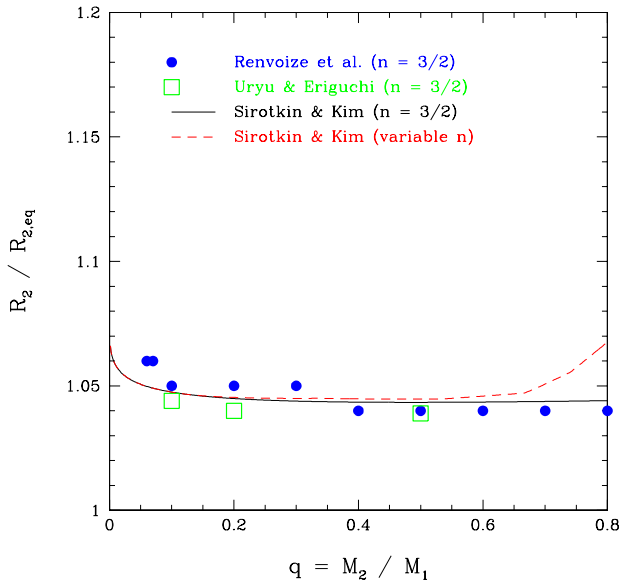


Figure 7. The effect of tidal and rotational deformation on the equilibrium stellar radius of a Roche-lobe-filling star. The solid black line is the analytical approximation derived by SK09 (our Equation 27) for polytropes with $n = 3/2$. This is appropriate for fully convective donors below the period gap. The blue points and green open squares show numerical results obtained for the $n = 3/2$ case in the hydrodynamic simulations by Renvoizé et al. (2002) and Uryu & Eriguchi (1999), respectively. The red dashed line shows the correction factor for CV donors if n is allowed to vary self-consistently with stellar mass and hence mass ratio, from $n = 3/2$ at the lowest mass ratios to $n = 2.8$ at the highest.

this: if we take an isolated spherical star with mass M_2 and equilibrium radius $R_{2,eq}$, place it in a binary, and then slowly contract the Roche lobe around it, what will its volume-averaged radius be at the point when it just reaches contact?

There have been several attempts to address this question in recent years. For example, Renvoizé et al. (2002) directly implemented the thought experiment described above via SPH simulations. Approximating MS stars as polytropes, they found that for polytropic index $n = 3/2$ (particularly appropriate for fully convective donors), R_L at contact was $\simeq 5\%$ larger than the equilibrium radius of the isolated star, with only a weak dependence on mass ratio. Similar results were found by Uryu & Eriguchi (1999), using a different computational technique.

Most recently, the question has been addressed again by SK09, who used a self-consistent field method that should be both accurate and computationally efficient. They show that the radii of Roche-lobe-filling polytropes exceed those of isolated ones by a factor

$$\frac{R_{RL}}{R_{iso}} = \left(\frac{N_{RL}}{N_{iso}} \right)^{n/(n-3)}, \quad (27)$$

where $N_{iso}(n)$ and $N_{RL}(n, q)$ are dimensionless coefficients appearing in the polytropic mass-radius relationships (see Equations 23 and 24 in SK09). Both of these coefficients depend on the polytropic index, n , while N_{RL} additionally depends the mass ratio of the system.

This latter dependence can be approximated by (Equation 40 in SK09)

$$N_{RL} = N_{iso} - \frac{d_1 q^{d_2}}{d_3 q^{d_4} + \ln(1 + q^{d_5})}. \quad (28)$$

Appropriate values for $N_{iso}(n)$ and $d_i(n)$ are provided in Table 1 for the parameter space relevant to CV donors. The values for $n = 3/2$ were taken from SK09, while the rest were kindly provided to us by Fedir Sirotkin (private communication).

Figure 7 shows the predicted deformation-induced radius inflation for $n = 3/2$ (appropriate for a fully convective donor) and for n varying self-consistently with stellar mass (and hence mass ratio) as given in Table 1. For $n = 3/2$, tidal and rotational deformation inflates donor radii by $\simeq 4.5\%$ across most of the mass ratio range. This is in quite reasonable agreement with the numerical results obtained by Renvoizé et al. (2002) and Uryu & Eriguchi (1999), which are also plotted in Figure 7. For the more realistic case of variable n , the deformation effects can be stronger. For the highest-mass donors we consider ($M_2 = 0.6M_\odot$, for which we adopt $n \simeq 2.3$), the radius inflation can be as large as 6.8% .¹⁶ In our self-consistent evolution sequences, we account for deformation-induced donor inflation by applying the correction factor predicted by Equation 27 with self-consistently varying n .

Before we move on, we note three caveats regarding our implementation of deformation-induced donor inflation. First, while there is good agreement between Renvoizé et al. (2002) and SK09 for $n = 3/2$ polytropes, the same is not true for $n = 3$ polytropes. This is probably due to the fact that the radius of an $n = 3$ polytrope does not depend on its mass, which may lead to computational difficulties for one or both methods. However, the precise reason for this discrepancy remains to be established. In practice, we do not think this is a serious problem, because the inflation predicted by the SK09 formalism for $n = 2.8$ agrees well with the inflation obtained for $n = 3$ by Renvoizé et al. (2002). Thus our results would be virtually unchanged if we had interpolated on the results of Renvoizé et al. (2002) instead of using the SK09 formalism.

Second, Landin et al. (2009) have also recently modelled the effect of Roche deformation on low-mass MS stars. Surprisingly, they find that the net effect of this deformation is to slightly *reduce* the stellar radius. The results of Landin et al. (2009) are based on the application of the Kippenhahn & Thomas (1970) perturbative method to full stellar models. It seems likely that their discrepant results are due to the breakdown of this method in the limit of strong distortion. However, we cannot rule out that the discrepancy may be related to the polytropic approximation, in which case the Landin et al. (2009) results would be preferred.

Third and finally, Renvoizé et al. (2002) have shown that, in addition to the mechanical effects of Roche deformation, there are also what they call “thermal ef-

¹⁶ For donors of even higher mass, the predicted level of deformation-induced inflation rises rapidly, reaching $\simeq 14\%$ for $M_2 \simeq 0.75$ ($n = 2.8$). We do not consider this regime, partly because we encounter numerical difficulties in applying such a large and fast-changing correction to our 1-dimensional stellar models.

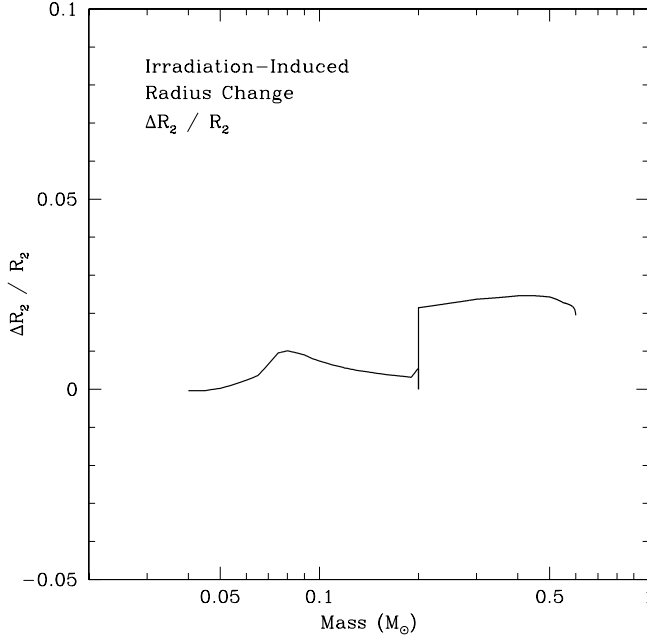


Figure 8. The expected amount of radius inflation due to irradiation along a standard-model CV evolution track. The net efficiency factor was assumed to be $\alpha = 0.1$ across the entire track; see text for details.

fects”. Briefly, the deformation-induced expansion of the donor changes its characteristic thermal time scale and hence its detailed response to mass loss. Renvoizé et al. (2002) show that these effects may partially compensate for deformation-induced inflation, i.e. they will tend to slightly reduce the effect of deformation on CV evolution sequences. We ignore these thermal effects in our models.

5.2.3. Irradiation

Another key difference between isolated MS stars and CV secondaries is that the latter may be exposed to irradiation from the vicinity of the WD primary. This irradiation can block the release of internally generated energy over some fraction of the donor’s surface, causing the donor to swell. Could this irradiation-induced donor bloating be large enough to matter in the present context?

Donor irradiation has been studied extensively in the literature, mainly in the context of long-term mass-transfer cycles (see Section 4; King et al. 1995, 1996; Ritter et al. 1995, 1996; Wu et al. 1995b,a; McCormick & Frank 1998; Ritter et al. 2000; King 2000; BR04). The key result for our purposes is that if irradiation blocks energy release over a fraction s of the donor’s surface, the donor radius will be inflated by a factor of about (Ritter et al. 2000)

$$\frac{R_2}{R_{2,0}} = (1 - s)^{0.1}. \quad (29)$$

A firm upper limit on the degree of irradiation-induced bloating can be obtained by noting that $s_{max} \leq 1/2$, with the equality obtaining if the entire hemisphere facing the primary is blocked. In this case, the radius of the donor would be inflated by about 7%. In reality, the pri-

mary does not “see” the entire facing hemisphere of the donor star, and so a better estimate is $s_{max} \simeq 0.3 - 0.4$ (BR04). The maximum possible irradiation-induced radius inflation is then 4% – 5%.

In order to obtain a more realistic estimate of donor bloating due to irradiation, we have to estimate the blocked surface fraction s . This is controlled primarily by the ratio of irradiating flux to intrinsic flux at the donor’s surface; the relevant dimensionless parameter can be written as (c.f. Hameury & Ritter 1997, hereafter HR97)

$$x_0 = \alpha_{acc} \alpha_{irr} \alpha_d \frac{(GM_1 \dot{M}_1)/(4\pi R_1 a^2)}{\sigma T_{eff,0}^4}. \quad (30)$$

Here, the α terms are efficiency factors which we discuss further below, \dot{M}_1 is the instantaneous accretion rate onto the WD, $T_{eff,0}$ is the effective temperature of the donor in the absence of irradiation, and all other symbols have their usual meaning.

Equation 30 is identical to Equation 8 in HR97, except that we have split their single efficiency factor into three separate terms, following BR04. The first, $\alpha_{acc} \leq 1$, allows for the non-isotropic release of accretion luminosity from the vicinity of the WD, and also for the possibility that the accretion disk may shield substantial portions of the donor from irradiation. The second, $\alpha_{irr} \lesssim 1$, measures the efficiency with which the irradiating flux penetrates to the sub-photospheric layers. The third, $\alpha_d \leq 1$, allows for the possibility that the release of accretion energy fluctuates on short time scales, in which case α_d is roughly equal to the duty cycle of the fluctuations (BR04).

HR97 have numerically calculated the function $s(x_0)$ for a large grid of stellar models spanning a wide range of T_{eff} and $\log g$. They have also provided a convenient numerical fitting formula for their results, along with an electronic table giving the relevant coefficients as a function of T_{eff} , $\log g$ and R_2/a .¹⁷

We can now assess the impact of irradiation on any particular CV donor. As a representative example, let us estimate the magnitude of irradiation-induced donor bloating along a standard-model-like CV evolution track, calculated with $\dot{J}_{sys} = \dot{J}_{GR} + \dot{J}_{MB} (\gamma = 3)$ above the gap and $\dot{J}_{sys} = \dot{J}_{GR}$ below the gap. (We have checked that the effect of irradiation on the optimal track discussed in Section 6.1 is qualitatively similar.) We conservatively take all efficiency parameters to be unity along the entire sequence, with two exceptions. First, we set $\alpha_{acc} = 0.1$ above the period gap; this roughly accounts for the anisotropic radiation and donor shielding produced by an optically thick accretion disk. Second, we take $\alpha_d = 0.1$ below the gap, since most short-period systems are dwarf novae with low duty cycles. With these choices, the net efficiency – $\alpha_{acc} \alpha_{irr} \alpha_d = 0.1$ – is constant along the entire evolution track. For each model CV along this track, we can now use Equation 30 to estimate x_0 , calculate $s(x_0)$ from the HR97 fitting formula (using coefficients appropriate for the current set of T_{eff} , $\log g$ and R_2/a) and finally use Equation 29 to determine

¹⁷ Since the original HR97 grid does not quite cover the full range of stellar properties we are interested in, Jean-Marie Hameury kindly provided us with an expanded table of coefficients.

the expected degree of donor inflation.

The results of this exercise are shown in Figure 8. We find that, even with our fairly conservative set of efficiency factors, irradiation-induced donor inflation is $< 3\%$ along the entire sequence, and $\lesssim 1\%$ below the period gap. The corresponding numbers for the optimal track in Section 6.1 are $< 2.5\%$ above the gap and $< 2\%$ below. As discussed in Section 5.2.1, we already explicitly allow for the possibility that our model radii systematically underestimate real MS star radii by 1.5% (for fully convective stars) or 4.9% (for stars with radiative cores). Since irradiation-induced donor inflation is usually smaller, and at most comparable, to this, yet is tricky to implement self-consistently, we draw the line here and neglect it in our modeling.¹⁸ In any case, the impact on our results of somewhat larger (or smaller) radius corrections – regardless of their cause – is discussed explicitly in Section 8.3.

5.3. Settling on the Form of \dot{J}_{sys}

In principle, we are now ready to construct our semi-empirical CV evolution track, but there is one last practical obstacle to overcome. The problem is that the construction of self-consistent donor evolution sequences is computationally expensive. Ideally, we would create large grids of self-consistent sequences for a wide range of AML recipes and normalizations, and then directly fit all of these to the empirical mass-radius data. However, this is simply not feasible.

We therefore adopt the following procedure. First, as noted in Section 2.3.1, we consider only the Rappaport et al. (1983, hereafter RVJ83) formulation for MB. With its adjustable normalization and power-law index γ (see Equation A7), this formulation allows us to efficiently cover the relevant parameter space in full. Second, we obtain a first estimate of $\dot{M}_2(P_{orb})$ by interpolating across a set of constant- \dot{M}_2 sequences to roughly match the observed donor mass-radius relationship. As discussed in Section 2.2.2, this ignores the effect of mass-loss history and is therefore not self-consistent. However, it does provide a good starting point for detailed modelling. Third, we compare the resulting approximate $\dot{M}_2(P_{orb})$ relation to those predicted by a range of RVJ83-like (Equation A7) with $0 \leq \gamma \leq 4$ and GR-like (Equation 9) AML prescriptions. We then finally identify those prescriptions that appear to best match the shape of the approximate $\dot{M}_2(P_{orb})$ relation above and below the period gap. Based on these steps, we adopted an RVJ83-based AML recipe with $\gamma = 3$ above the gap, and a GR-based one (Equation 9) below the gap in our self-consistent models. It should be understood, however, that we do not consider the exact shape of the AML recipes to be particularly well constrained (see, for example, the discussion in Section 7.2.3).

5.4. Constructing the Final Track

With the AML prescription fixed, the final evolution track can be constructed via the following steps. First,

we calculate two small grids of self-consistent evolution tracks. The set of normalization factors covered by the RVJ83-based grid for CVs above the gap was $f_{MB} = 0.25, 0.5, 1.0, 2.0, 4.0$; the corresponding set of normalization factors for the GR-based grid for short-period CVs was $f_{GR} = 1.0, 2.0, 3.0, 4.0, 5.0$.¹⁹ Tracks for other normalization factors are constructed via linear interpolation on these grids.

The donor models used in creating these evolution sequences employ the BCAH98 stellar physics, which still represents the state of the art in modelling of low-mass stars. In a CV context, BCAH98-based donor models have previously been used by Kolb & Baraffe (1999, 2000); Baraffe & Kolb (2000); Kolb et al. (2001a), and we refer the reader to these papers for additional details. However, one point that does deserve explicit mention is that the BCAH98 models do not include a treatment for atmospheric dust formation and settling. Dust is expected to form in the atmospheres of very cool ($T_{eff} \lesssim 2500$ K), low-mass ($M_2 \lesssim 0.1M_\odot$) donors, and to eventually settle out again at even lower temperatures ($T_{eff} \lesssim 1700$ K). However, these processes will primarily affect the SED of the donor, rather than its radius and response to mass loss, and this can be taken into account by calculating photometric properties from model atmosphere grids that do account for dust.²⁰ We have checked that the radius difference between the BCAH98 5-Gyr isochrone and an equivalent one that accounts for dust (based on the DUSTY00 models described by Chabrier et al. 2000) is less than 1% down to $M_2 = 0.075M_\odot$. Thus our BCAH98-based evolution sequences and associated donor properties should be quite reliable for essentially the entire parameter space covering long-period and pre-bounce short-period CVs. It should nevertheless be kept in mind that our BCAH98-based models will become less reliable as we move deeply into the regime of sub-stellar secondaries and post-period-minimum CVs.

Next, we apply the donor radius correction factors discussed in Section 5.2. For the secondaries in short-period CVs, this means a 1.5% upward correction to bring the BCAH98 model radii in line with observations of non-interacting stars, and a $\simeq 4.5\%$ upward correction to account for tidal and rotational deformation. For donors in long-period CVs, the corresponding corrections are 4.9% and 4.5% – 6.9%, respectively. For comparison, we have also carried out calculations with smaller and larger correction factors; the impact of the adopted correction factors on our results will be discussed in Section 8.3. Note also that, as discussed in Section 5.2.2, the corrections for tidal and rotation distortion are actually a function of donor mass and mass ratio.

Since all radius corrections change the mean density of the donor, we also need to adjust the orbital period of the system in order to retain consistency with the period-density relation. Moreover, since our AML recipes are functions of P_{orb} and R_2 , changing these parameters also produces a slight inconsistency between the

¹⁸ Implementing a self-consistent correction for irradiation-induced donor bloating is non-trivial, because the strength of irradiation depends itself on the mass-loss rate from the donor. Thus there is feedback between irradiation- and ML-induced donor inflation, necessitating the use of an iterative computational scheme.

¹⁹ Normalization factors below unity are unphysical, as GR-driven AML must always be active. Also, Figure 2 already shows that AML rates in excess of GR are likely needed below the gap.

²⁰ Of course, one hemisphere of the donor is also bathed in UV and X-ray radiation from the vicinity of the WD primary, which might inhibit dust formation in its atmosphere.

mass- and angular-momentum-loss rates that were actually used in the models (\dot{J}_{sys} and \dot{M}_2) and the values that these recipes would now produce, given the adjusted donor radius and orbital period (\dot{J}'_{sys} and \dot{M}'_2). In order to get back to a mutually consistent set of parameters, we use an iterative scheme. Thus we adjust the radius again, this time by the amount expected from considering the ratio \dot{M}'_2/\dot{M}_2 . We then recalculate the orbital period and re-estimate the expected angular-momentum-loss and mass-loss rates for the new set of system parameters. This sequence of adjustments is repeated until mass, radius, period, AML- and ML-rates are all mutually consistent again.

Third, we fit the adjusted models to the empirical data. We do this via a χ^2 -minimization in the $P_{orb} - M_2$ plane. Since errors on orbital periods are usually much smaller than those on donor masses, we neglect them. However, we do add an intrinsic dispersion term and allow this to affect both M_2 and P_{orb} isotropically. The goodness-of-fit statistic we minimize is thus

$$\chi^2 = \sum_{i=1}^N \frac{(\log M_{2,i} - \log M_{2,mod})^2}{\sigma_{\log M_{2,i}}^2 + \sigma_{int}^2} + \frac{(\log P_{orb,i} - \log P_{orb,mod})^2}{\sigma_{int}^2}, \quad (31)$$

where N is the number of data points, and σ_{int} is adjusted so as make $\chi^2 = N - 1$ (the only free parameter we fit is the normalization of our adopted AML recipes). The χ^2 associated with each individual datum is evaluated at the point along the model sequence that minimizes this χ^2 . Thus we can calculate meaningful χ^2 values even for sequences that do not extend to the lowest observed orbital periods, for example. Errors on the normalization factors are derived in the usual way, by considering the change in normalization required to reduce the goodness-of-fit by $\Delta\chi^2 = 1$.

Up to this point, long-period and short-period systems have been treated independently, since they are characterized by different AML recipes. The fourth step in constructing the final evolution track is therefore to merge the two sequences. In doing so, we include the detached evolution through the period gap, under the assumption that AML in the gap follows the same AML recipe and normalization as derived for CVs below the gap. We do not, however, follow the relaxation of the donor star back to its thermal equilibrium radius in detail. In reality, this happens on a time scale of τ_{adj} (Equation 8), but we simply reset R_2 to its equilibrium MS value immediately after the system has entered the gap. We have checked, however, that τ_{adj} is significantly shorter than the time it takes a CV to pass through the gap in our models.

The fifth and final step is to calculate the photometric donor properties along the evolution track. We do this by interpolating in T_{eff} and $\log g$ on the same set of stellar atmosphere grids that were also used for the updated broken-power-law donor sequence (Section 3). Thus we again adopt the standard NextGen atmosphere models (Hauschildt et al. 1999) down to $T_{eff} = 2300$ K, the AMES-DUSTY models (Chabrier et al. 2000) between $1800 \text{ K} \leq T_{eff} \leq 2000 \text{ K}$, and the AMES-COND models

(Baraffe et al. 2003) for temperatures $T_{eff} \leq 1700$ K. The boundaries between these regimes are bridged by interpolation.

Physically, these model grids differ mainly in their treatment of dust²¹: the NexGen models assume that no dust formation has taken place in the atmosphere; the DUSTY models allow for the formation of dust grains and include their opacity; the COND models also include dust formation, but do not include its opacity. The assumption behind the COND models is that rapid gravitational settling efficiently removes dust from the atmosphere.

Our choices here are based partly on a comparison to the MS star data of Beuermann et al. (1999), and partly on a desire to keep the photometric donor properties relatively smooth along our model track. Thus the NextGen grid does the best job of reproducing the observed location of the MS in the $(I - K)$ vs M_K plane down to $I - K \simeq 4.5$, which corresponds to about $T_{eff} \simeq 2300$ K. Moreover, there can be fairly substantial photometric differences between the different grids at the same temperature and surface gravity, so an abrupt switch at the recommended temperatures would have introduced awkward discontinuities into the model sequences. These considerations also imply, of course, that the photometric donor properties below $T_{eff} \simeq 2300$ K (i.e. in systems near or beyond period bounce) should be treated with considerable caution. The underlying problem is that the physics governing the gradual formation and settling of atmospheric dust have still not been comprehensively modelled, even in isolated MS stars and brown dwarfs. Given that CV secondaries are additionally exposed to anisotropic UV and X-ray radiation fields, it is quite unclear whether and how one should account for dust formation and settling in their atmospheres.

6. A COMPLETE, SEMI-EMPIRICAL, DONOR-BASED CV EVOLUTION TRACK

The final result of this model construction and fitting process is shown in Figure 9. This represents the main result of our study. The top panel shows the data and the best-fitting model sequence in the $P_{orb} - M_2$ plane; the bottom panel shows the same information in the $M_2 - R_2$ plane. For comparison, we also show a classic “standard model” sequence, in which we adopt the same AML recipes as for our best-fit model (GR below the gap, RVJ83 with $\gamma = 3$ above the gap), but fix the normalization of these recipes to unity ($f_{GR} = f_{MB} = 1$). Note that we do apply the radius correction factors discussed in Section 5.2 to the standard sequence, so it is still an improvement on similar sequences published previously.

The normalization factors derived for our best-fit sequence are 2.47 ± 0.22 below the gap and 0.66 ± 0.05 above the gap.²² Thus our results imply that AML is somewhat stronger than pure GR in short-period CVs, but somewhat weaker than a typical MB formulation in long-period CVs. No intrinsic dispersion at all was needed for long-period systems (we obtained $\chi^2_{\nu} = 1.0$

²¹ They also employ different molecular line lists; see Chabrier et al. (2000) and Baraffe et al. (2003) for details.

²² The errors quoted here are purely statistical and, in particular, do not include the systematic uncertainties associated with the corrections discussed in Section 5.2.

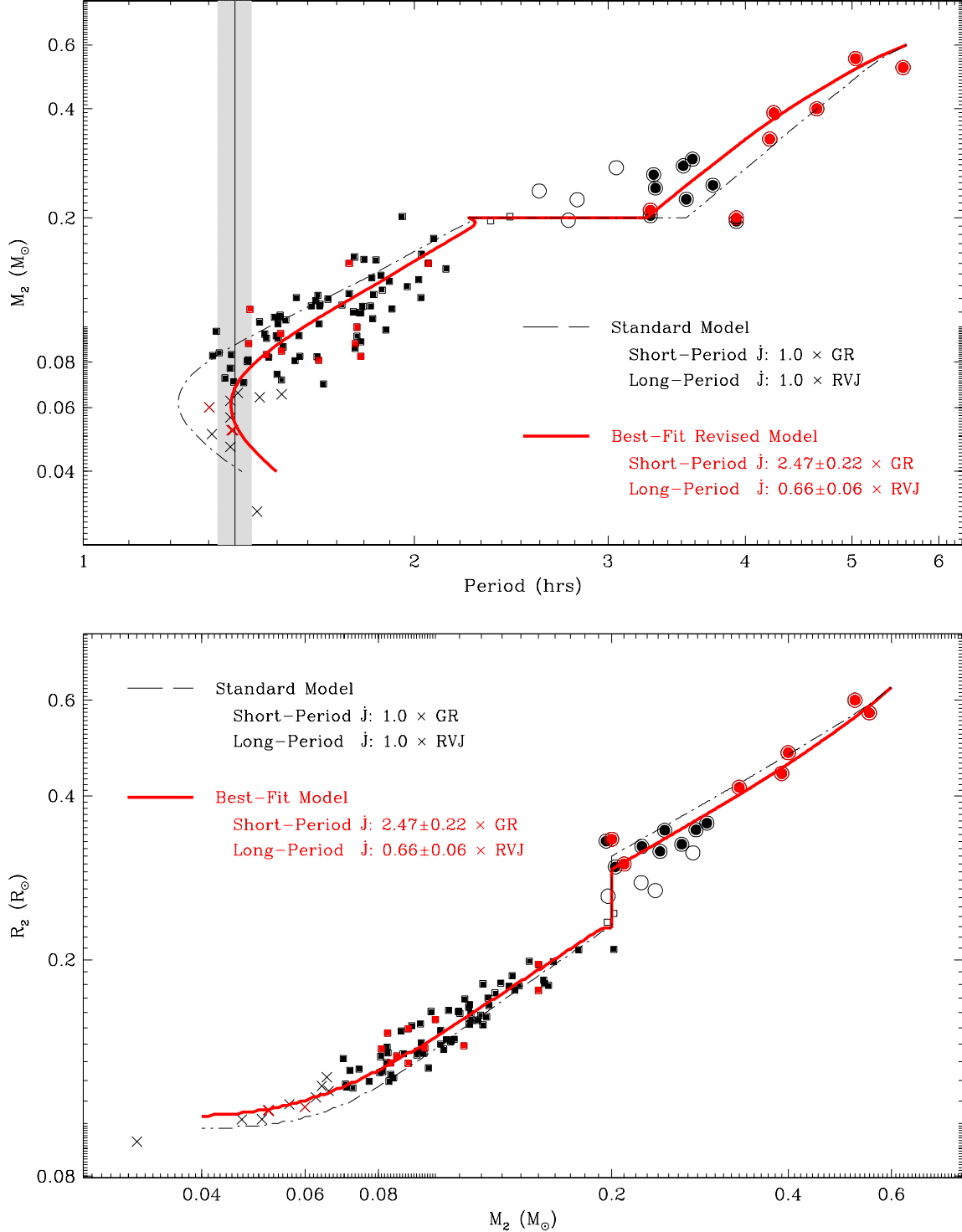


Figure 9. Self-consistent model fits to the observed properties of CV donors in the period-mass (top panel) and mass-radius (bottom panel) planes. The same symbols as in Figure 4 are used for the data points. Error bars are suppressed for clarity, but were used in the fits. The black dash-dotted line shows the predicted evolution of donor properties according to the standard model for CV evolution, which is characterized by $f_{GR} = f_{MB} = 1$. The red solid line shows the evolution of donor properties along the best-fit model track. This revised model is characterized by $f_{GR} = 2.47 \pm 0.22$ (i.e. enhanced AML) below the gap and $f_{MB} = 0.66 \pm 0.05$ (i.e. slightly reduced AML) above. The vertical line in the top panel marks the observed location of the period spike (which presumably corresponds to P_{min} ; the width of the shaded area around this corresponds to the FWHM of the spike as measured in G09).

with $\sigma_{int} = 0$); for short-period CVs, a small intrinsic dispersion of $\sigma_{int} = 0.02$ dex was sufficient to achieve $\chi^2_\nu = 1.0$.

Figure 9 shows that our best-fit donor evolution sequence is a substantial improvement on the standard model in terms of its match to the data, especially below the period gap. Here, the standard model clearly underpredicts the donor radii at fixed mass (or, equivalently, overpredicts their masses at fixed P_{orb}). It also predicts a minimum period that is inconsistent with the period spike (G09), whose location is marked by the vertical line in the top panel, and also with the data shown in Figure 9. By contrast, the best-fit sequence describes the data quite well. In particular, it predicts a minimum period that matches the location of the period spike (see also Section 6.2 below). This was not guaranteed, since the value of P_{min} is not imposed as a boundary condition in the construction of the best-fit evolution sequence.

In order to make our calculations as useful as possible to the community, we provide comprehensive listings of all relevant physical and photometric binary parameters along both the standard model track and along our new best-fit evolution sequence in Tables 3 - 6

As a supplement to our donor-based evolution tracks, we have also calculated the corresponding physical properties of the WD primary. For this, we first estimated the effective temperature of the $0.75 M_\odot$ WD assumed in our models by interpolating on the theoretical \dot{M}_{acc} vs $T_{eff,1}$ calibration for $0.6 M_\odot$ and $1.0 M_\odot$ WDs shown in Figure 10 of Townsley & Bildsten (2004).²³ As discussed in their paper (and shown in their results), even for fixed mass and accretion rate, the predicted $T_{eff,1}$ depends somewhat on the mass of the accreted layer on the surface of the WD, ΔM_{acc} . Following Townsley & Bildsten (2004), we have therefore calculated three sets of WD temperatures for each model track, corresponding to $\Delta M_{acc} \simeq (0.05, 0.5, 0.95) M_{ign}$, where $M_{ign}(M_1, \dot{M}_{acc})$ is the ignition mass required to trigger a nova eruption. Our default set with $\Delta M_{acc} \simeq 0.5 M_{ign}$ corresponds to systems about halfway between nova eruptions, while the other two sets represent the upper and lower limits corresponding to system just before or after a nova outburst.²⁴ Given M_1 and $T_{eff,1}$, we then estimate R_1 and all photometric properties by interpolating on the Holberg & Bergeron (2006) grid of WD models.²⁵ The predicted properties of the accreting WD are listed as a function of P_{orb} in Tables 7 and 8.

In the following sections, we will take a closer look at the detailed properties of our revised, donor-based CV evolution track. Where appropriate, we will also compare it to both the broken-power-law donor sequence derived in Section 3 and a conventional, “standard model” evolution track (i.e. $f_{GR} = f_{MB} = 1$).

6.1. Physical and Photometric Properties

²³ Note, however, that the Townsley & Bildsten (2004) calculations do not account for the dependence of the WD radius, R_1 , on $T_{eff,1}$.

²⁴ The heating of the WD by the thermonuclear burning it undergoes during a nova outburst is not taken into account, however. See TG09 for a discussion of this effect.

²⁵ <http://www.astro.umontreal.ca/bergeron/CoolingModels/>

Figure 10 shows the physical properties of the donor star as a function of orbital period along the standard model track (thick blue line) and along our new best-fit model track (thick red line). For comparison, we also show the physical donor properties along both the original (thin black dashed line) and updated (thin magenta dashed line) broken-power-law donor sequences. The donor properties along both broken-power-law sequences are generally very similar to those along our new best-fit model, except in the poorly constrained period-bounce regime. This is reassuring, since all of these sequences are based on almost the same set of donor mass-radius data.

The physical differences between the standard and best-fit models are also easily understood. Above the gap, AML is stronger in the standard model, resulting in a larger donor radius, lower surface gravity, lower luminosity and larger mass-radius index. Moreover, due to the period-density relation, the mass at fixed period is higher along the standard track, and the effective temperature slightly lower (this is hard to see on the scale shown in the Figure 10). Below the gap, the situation is exactly reversed. In particular, the higher mass-transfer rate in the best-fit model causes the mass-radius index to drop to $1/3$ at a considerably longer orbital period than in the standard model (82 min vs 73 min), although at nearly the same donor mass ($M_{bounce} = 0.061 M_\odot$ vs $0.062 M_\odot$, respectively). It is worth noting that, even in our version of the standard model, the minimum period is considerably longer than that found in most previous investigations. This is because of our corrections for tidal/rotational deformation and for the radius offset between stellar models and non-interacting stars, which is probably related to magnetic activity (see Section 5.2). Below the gap, these upward radius corrections amount to about 4.5% and 1.5%. As a result of the period-density relation, the combined 6% upward radius correction produces a $\simeq 9\%$ upward shift in the location of period bounce.

Figure 10 also shows the temperature and luminosity of the accreting WD as a function of P_{orb} along the model tracks. Since M_1 is constant along our tracks (by assumption), other WD parameters do not evolve appreciably and are therefore not plotted. It is interesting to note that the bolometric luminosity of the accreting WD dominates over that of the donor star in essentially all model systems. The only exception occurs in the standard model sequence, where there is a small region just below the period gap where the secondary’s bolometric output exceeds that of the WD.

The evolution of the *binary* parameters is shown as a function of orbital period in Figure 11 and as a function of time in Figure 12. Again, we show both the standard model and our best-fit donor-based evolution track. As expected, the evolution is initially faster in the standard model (since $f_{MB} = 0.65 < 1$ above the gap in the best-fit model), but this situation is quickly reversed below the gap, where the AML rate of the best-fit model is substantially higher ($f_{GR} = 2.47$) than that of the standard model ($f_{GR} = 1$). In the standard model, the upper edge of the period gap is reached after about 1.7×10^8 years, while in the best-fit model, systems enter the gap after about 2.4×10^8 . Here and throughout, $t = 0$ refers to a

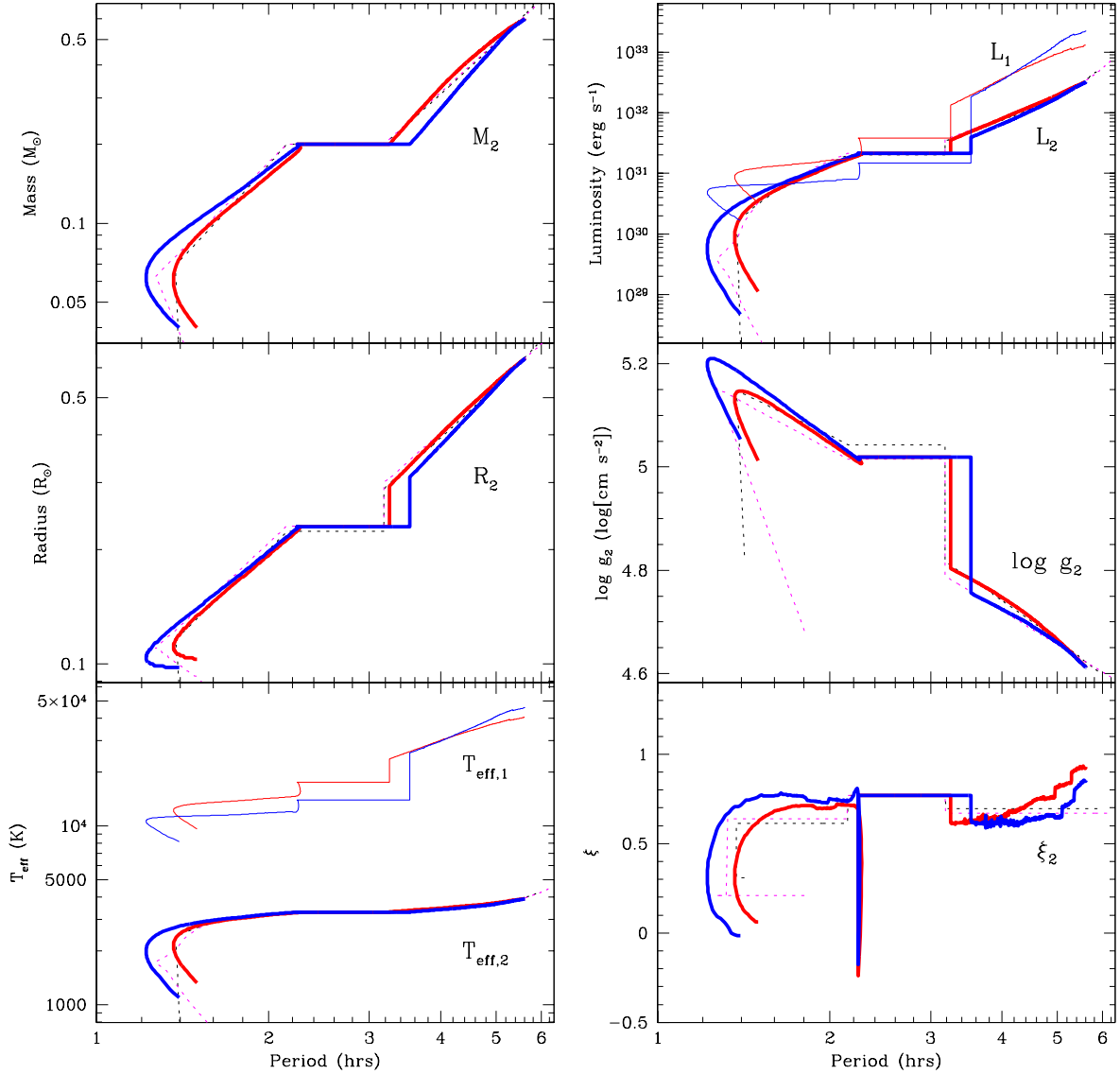


Figure 10. The run of physical donor properties as a function of orbital period along standard and revised evolution tracks. The left-hand column of panels shows, from top to bottom, the donor mass, radius and effective temperature. The right-hand column of panels shows, from top to bottom, the donor luminosity, surface gravity and effective mass-radius index. In each panel, the thick blue solid line is the track corresponding to the standard model ($f_{GR} = f_{MB} = 1$) while the thick red solid line is the evolution sequence predicted by the revised model ($f_{GR} = 2.47$; $f_{MB} = 0.66$). In each panel, we also show the original (thin magenta dashed line) and updated (thin black dashed line) broken-power-law donor sequences (see Section 3). For comparison, the (long-term average) temperature and luminosity predicted for the accreting WD in our evolution sequences are also plotted in the relevant panels (thin solid blue line: standard model; thin solid red line: revised model).

system reaching contact at a donor mass of $M_2 = 0.6M_\odot$. Evolution through the gap takes about 1.3 Gyrs in the standard model, but only about 0.4 Gyrs in the best-fit model, due to the higher AML rate in the latter. Period bounce is reached after about 5.7 Gyrs (standard model) or 2.6 Gyrs (best-fit model).

These time scale differences are important, because they directly affect the number of systems we may expect to find in the different phases of CV evolution. For example, we have seen that CVs evolve faster below the period

gap in the best-fit model and reach period bounce sooner. Thus CVs evolving according to our best-fit model spend a smaller fraction of their life as short-period, pre-bounce CVs, but a larger fraction as period bouncers. Correspondingly, we may expect (and Section 7.3 indeed confirms) that the best-fit model predicts a lower percentage of short-period, pre-bounce CVs among the Galactic CV population, but a higher percentage of period bouncers. This change helps to reconcile some of the long-standing clashes between the standard model and the statistics of

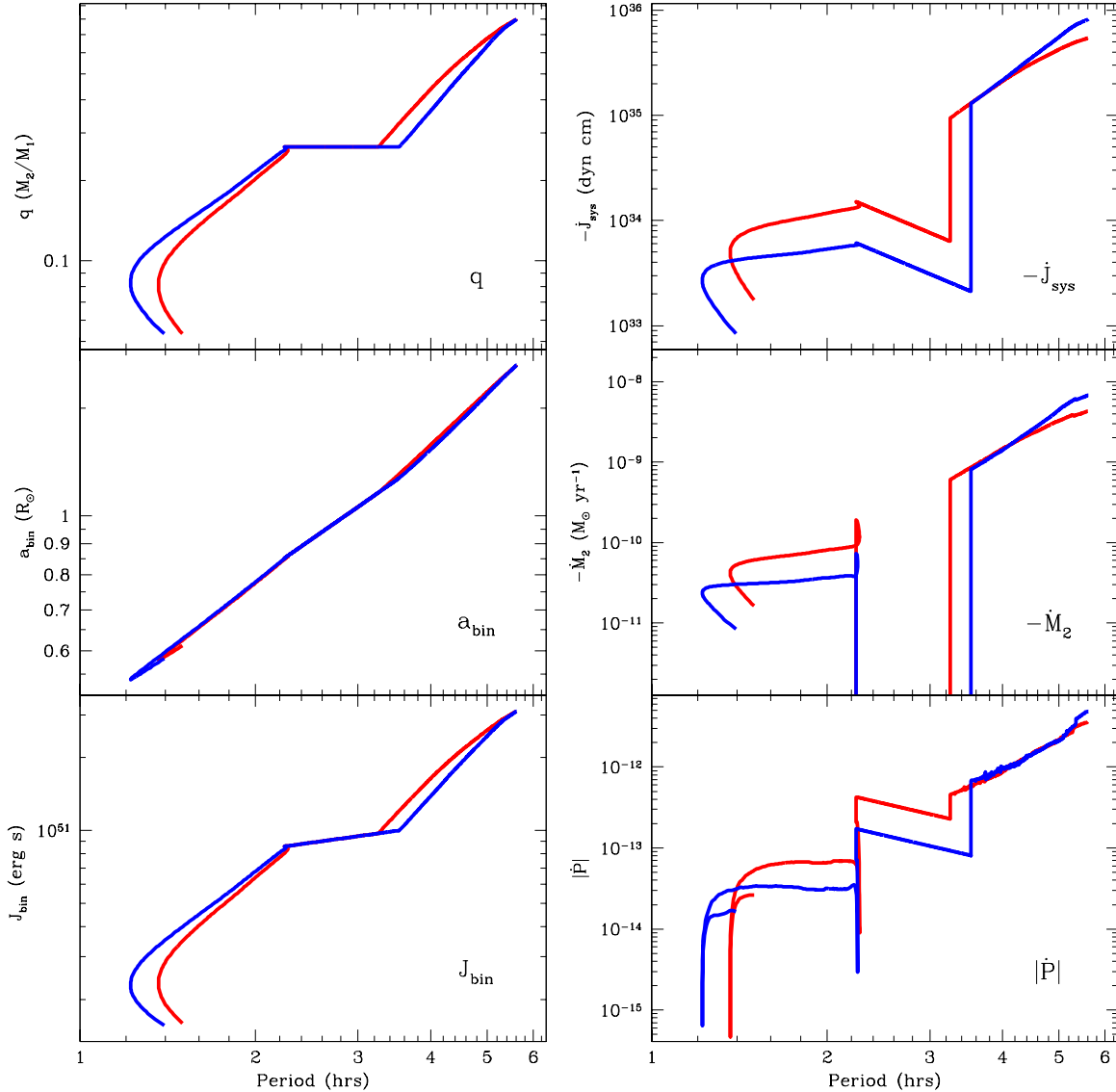


Figure 11. The evolution of key binary parameters as a function of orbital period along our self-consistent model tracks. In all panels, the thick blue line is the standard model ($f_{GR} = f_{MB} = 1$), while the thick red line is the revised best-fit model ($f_{GR} = 2.47$; $f_{MB} = 0.66$). The left-hand column of panels shows, from top to bottom, the evolution of the mass ratio, binary separation and orbital angular momentum. The right-hand column of panels shows, from top to bottom, the evolution of the systemic angular-momentum-loss rate, the mass-transfer rate and the orbital period derivative.

observational CV samples.

Finally, in Figure 13, we show the run of optical (B, V, R) and near-infrared (J, H, K) absolute magnitudes for both the donor and the accreting WD along our self-consistent evolution sequences. These plots confirm several pieces of conventional wisdom. For example, only unusually bright (e.g. nuclear-evolved) donors are expected to be easily detectable at optical wavelengths, and particularly in the blue. Even the accreting WD competes with – or even outshines – the secondary at these wavelengths. In the infrared, the situation is considerably more favourable, but a key point to note is the

steep drop-off in donor brightness near P_{min} in all bands. Around P_{min} , the WD begins to compete with the donor even in the near-infrared. Given that the accretion disk is likely to be considerably brighter than the WD in both the optical and near-infrared, this highlights the observational challenge facing us if we wish to directly detect and characterize the sub-stellar donors in period bouncers.

6.2. The Locations of Period Bounce and Period Gap

Figure 14 presents a closer look at the locations of the three critical orbital periods that delineate the life of a CV: the minimum period, as well as the upper and lower

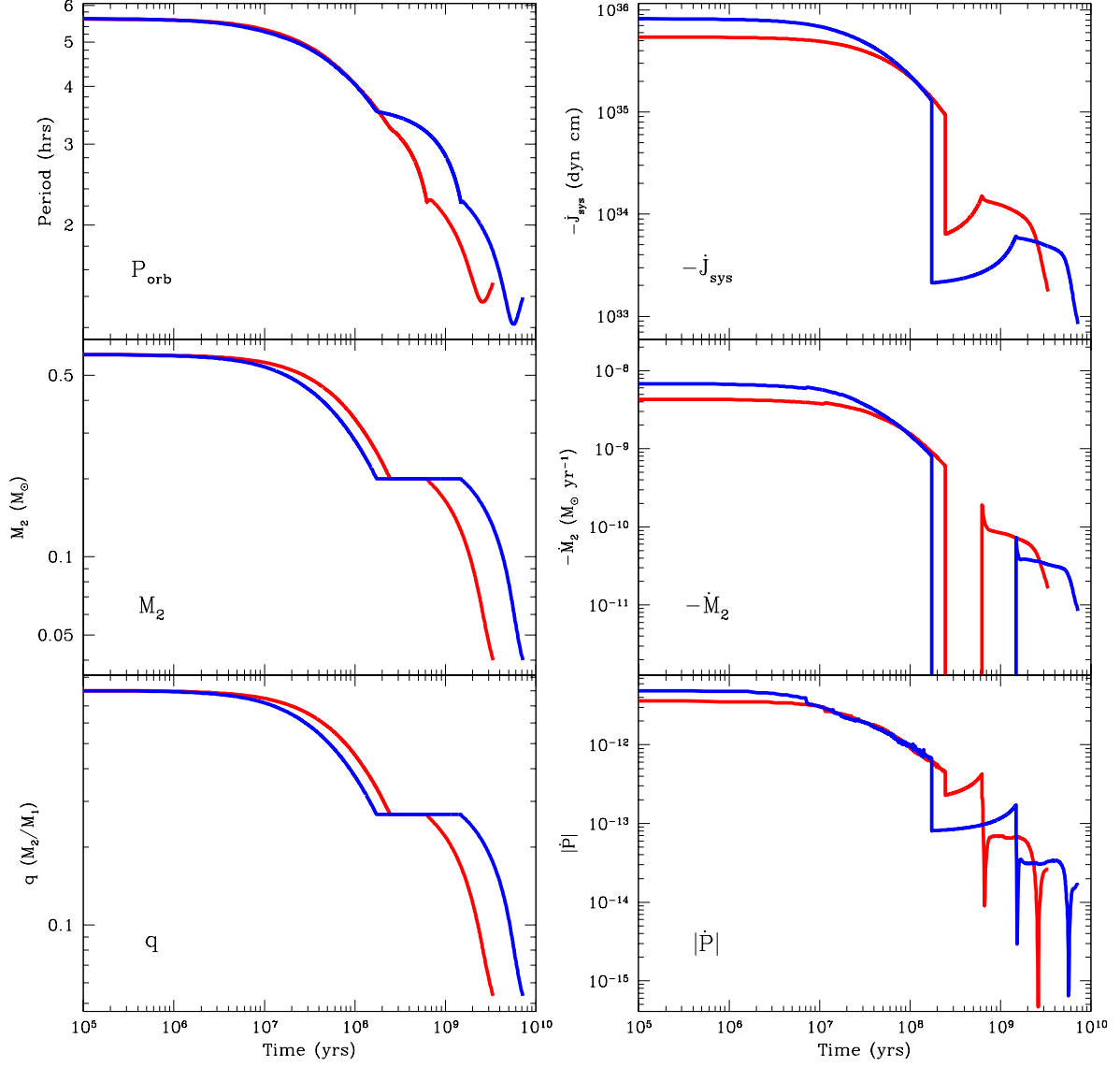


Figure 12. The evolution of key binary parameters as a function of time along our self-consistent model tracks. In all panels, the thick blue line is the standard model ($f_{GR} = f_{MB} = 1$), while the thick red line is the revised best-fit model ($f_{GR} = 2.47$; $f_{MB} = 0.66$). The left-hand column of panels shows, from top to bottom, the evolution of the orbital period, the donor mass and the mass ratio. The right-hand column of panels shows, from top to bottom, the evolution of the systemic angular-momentum-loss rate, the mass-transfer rate and the orbital period derivative.

edges of the period gap.

In the top panel, we show how the predicted location of P_{min} depends on f_{GR} . The thick part of the curve marks the 1σ confidence interval around our best-fit value of $f_{GR} = 2.47$. The vertical line shows the observed location of the period spike, as determined by G09. Their estimate of P_{min} was determined by fitting a Gaussian to the spike, and the vertical grey bands in the top panel mark their corresponding estimate of the error on P_{min} and the FWHM of the spike.

The run of P_{min} with f_{GR} in the top panel confirms that, in order to match the observed location of P_{min} ,

it is necessary to invoke AML rates in excess of GR below the period gap. More interestingly, it shows that our best-fit model predicts a value for P_{min} (81.8 ± 0.9 min) that is in excellent, quantitative agreement with the observed location of the period spike (82.4 ± 0.7 min). Note that this success was not guaranteed. Unlike for our broken-power-law donor sequence, we do not impose P_{min} as an external constraint when fitting the data. Thus the predicted P_{min} emerges simply from the fit to the mass-radius data shown in Figure 9 – a data set that is very different from the SDSS sample used by G09.

Turning to the period gap, let us take the upper edge

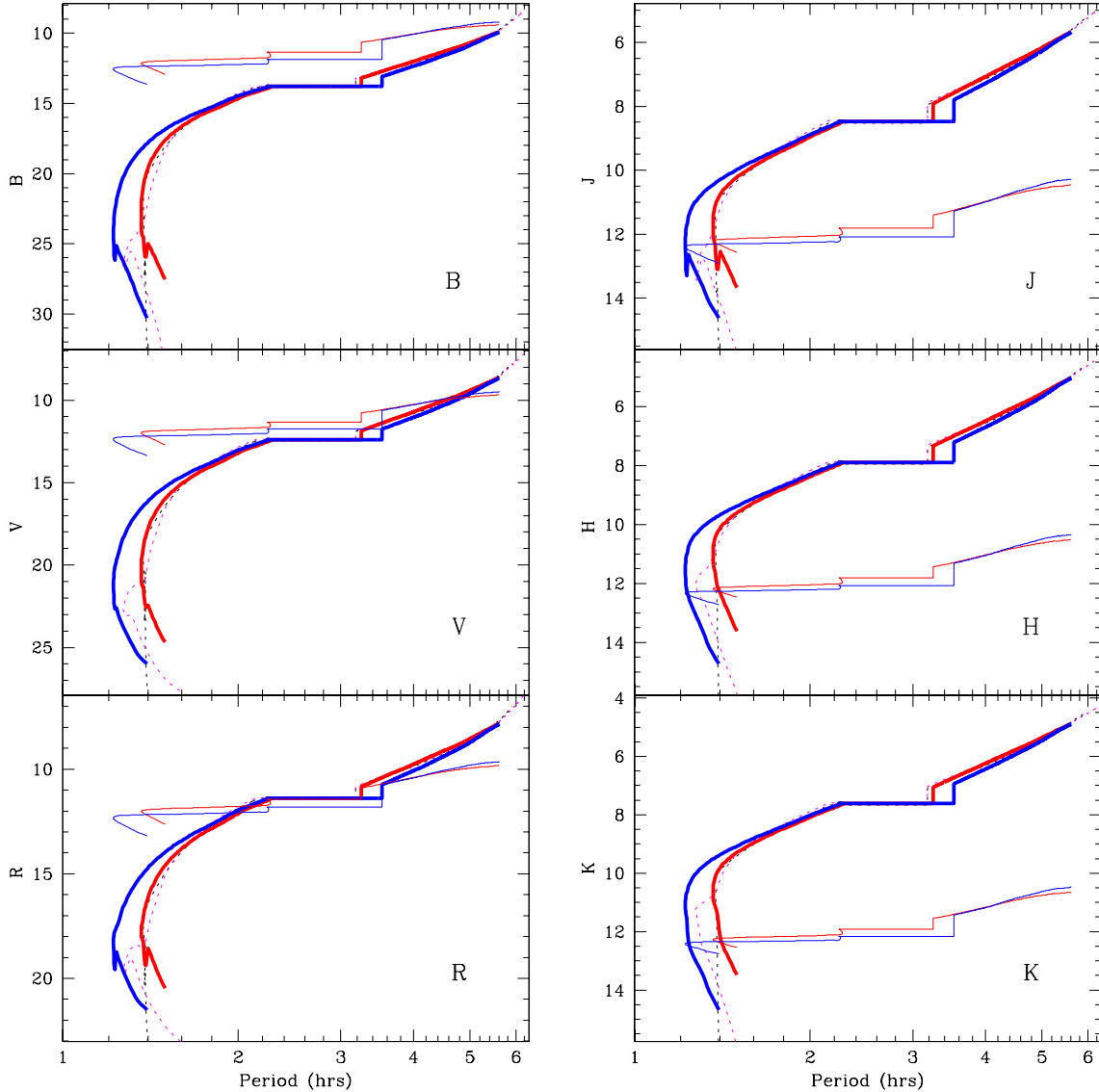


Figure 13. The evolution of the absolute magnitudes of both binary components as a function of orbital period along our self-consistent evolution tracks. The left-hand column of panels shows three optical bands (from top to bottom: B , V and R), while the right-hand column of panels shows three near-infrared bands (from top to bottom: J , H and K). The thick solid blue and red lines represent the absolute magnitudes of the donor stars along the standard ($f_{GR} = f_{MB} = 1$) and revised best-fit ($f_{GR} = 2.47$; $f_{MB} = 0.66$) evolution sequence, respectively. The thin solid blue and red lines show the corresponding absolute magnitudes of the accreting WDs. In each panel, we also plot tracks corresponding to the original (thin magenta dashed line) and updated (thin black dashed line) broken-power-law donor sequences (see Section 3).

first (bottom panel in Figure 14). In our models, we have assumed that systems enter the period gap when their donor mass reaches the empirically determined values of $M_{conv} = 0.20 \pm 0.02 M_{\odot}$ (K06). The notation “conv” here reflects the conventional notion that the period gap is caused by a disruption of MB associated with the transition of the donor star to a fully convective structure. However, this empirically determined value for M_{conv} does not have to correspond to the actual mass at which the models predict a transition to a fully convective structure. In fact, the inset in the bot-

tom panel shows how this theoretically predicted value, $M_{conv,th}$, varies with f_{MB} . Starting from the MS value of $M_{conv,th} \simeq 0.35 M_{\odot}$ at $f_{MB} = 0$, $M_{conv,th}$ initially drops steeply with increasing f_{MB} , but then asymptotes around $M_{conv,th} \simeq 0.22 M_{conv}$ beyond $f_{MB} \simeq 1$. Based on a simple linear interpolation, the value of $M_{conv,th}$ corresponding to our best-fit estimate of $f_{MB} = 0.65 \pm 0.05$ is $M_{conv,th} = 0.236 \pm 0.002 M_{\odot}$. We conclude that the empirically determined estimate of M_{conv} is in reasonable, though by no means perfect agreement with the idea that AML in CVs is suppressed exactly (and instan-

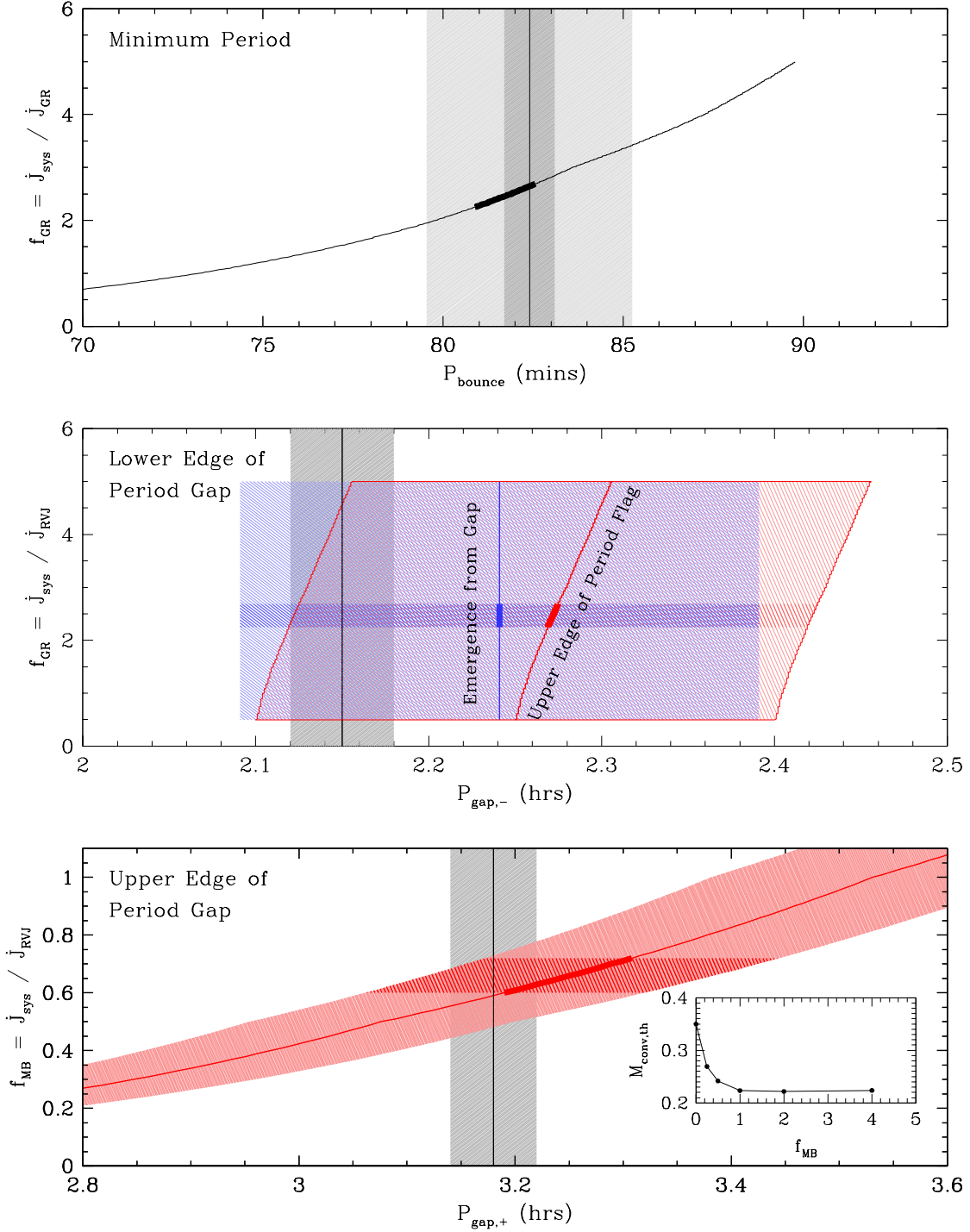


Figure 14. Predicted and observed locations of the critical periods along a CV evolution track. *Top panel:* The predicted location of the minimum period as a function of f_{GR} , the angular-momentum-loss rate relative to GR. The thick part of the curve marks the 1σ confidence interval around our best-fit value of $f_{GR} = 2.47 \pm 0.22$. The vertical line is the observed location of the period spike $P_{min} = 82.4 \pm 0.7$ min (G09). The vertical shaded regions mark the error on P_{min} (dark grey) and the intrinsic FWHM (5.7 min) of the spike (light grey). *Middle panel:* The predicted location of the lower edge of the period gap as a function of f_{GR} . The blue line corresponds to the period at which the system emerges from the period gap and re-establishes contact; the red line is the upper edge of the period flag, i.e. the longest period reached before evolution proceeds to shorter periods again (see text for details). The thick portions on both lines correspond to the 1σ confidence interval around our best-fit value of $f_{GR} = 2.47 \pm 0.22$. The blue- and red- shaded regions extending left and right of these curves show the uncertainty on the location of the lower gap edge arising from uncertainty in the donor mass corresponding to the period gap ($M_{conv} = 0.20 \pm 0.02 M_{\odot}$). The vertical black line and grey shaded region mark the observed location of $P_{gap,-}$ and the error on this ($P_{gap,-} = 2.15 \pm 0.03$ hrs; K06). *Bottom panel:* The red line shows the predicted location of the upper gap edge, $P_{gap,+}$, as a function of f_{MB} , the angular momentum loss rate relative to the standard RVJ recipe with $\gamma = 3$. The thick part of the line marks the 1σ confidence interval around our best-fit value of $f_{MB} = 0.66 \pm 0.05$. The red-shaded region extending left and right of this line again shows the uncertainty on the location of the upper gap edge arising from uncertainty in the donor mass corresponding to the period gap. The vertical black line and grey shaded region mark the observed location of $P_{gap,+}$ and the error on this ($P_{gap,+} = 3.18 \pm 0.04$ hrs; K06). The inset in the bottom panel shows the mass at which our stellar models formally become fully convective as a function of f_{MB} .

taneously) when the donor star becomes fully convective. We also note that *if* this scenario is taken seriously, and *if* we are willing to trust the stellar models in this respect, then extremely low values of $f_{MB} \lesssim 0.25$ would be ruled out. However, these are both rather big “ifs”, so we will continue to adopt the empirically determined M_{conv} in the construction of our model sequences.

Returning to the main plot in the bottom panel of Figure 14, the red line shows the predicted location of the upper gap edge as a function of f_{MB} . The thick part of the curve marks the 1σ range around our best-fit value of $f_{MB} = 0.65 \pm 0.05$. The red shaded region around this curve shows the uncertainty associated with the $0.02M_{\odot}$ error on M_{conv} . The best-fit model predicts $P_{gap,+} = 3.24 \pm 0.05$ hrs, which is an excellent match to the observed location of the gap edge. By contrast, the standard model – which corresponds to the point on the curve where $f_{MB} = 1$ – predicts $P_{gap,+} = 3.52$ hrs, significantly longer than observed.

We finally turn to the middle panel of Figure 14, which compares predicted and observed locations of the lower edge of the gap. Here, we actually show two theoretically predicted locations. The blue vertical line shows the period at which the system is predicted to emerge from the period gap, P_{emerge} . Since the donor is just a MS star in thermal equilibrium at this point, P_{emerge} is independent of f_{GR} or f_{MB} – it only depends on M_{conv} and the MS mass-radius relationship. The blue-shaded region shows the uncertainty in the predicted location associated with the error on M_{conv} .

By contrast, the red curve and red shaded region show the maximum extent of the so-called *period flag*. The period flag is a small “loop” in the P_{orb} vs \dot{M}_2 plane that is executed by CVs as they emerge below the gap, immediately after the turn-on of mass transfer and before settling on the standard evolution track that will ultimately take them to P_{min} . The period flag is clearly visible in the middle panel of Figure 11, and the physics responsible for it have been discussed in detail by Ritter & Kolb (1992) and Stehle et al. (1996).

Briefly, the period flag arises because the mass-transfer rate initially rises exponentially when contact between Roche lobe and secondary is re-established below the gap. Thus there is a brief window in which significant mass loss has already begun, but the secondary has not yet had time to relax thermally. During this window, the mass loss is effectively adiabatic, and the response of the fully convective donor to adiabatic mass loss is to swell up ($\zeta_{ad} \simeq -1/3$). Following the discussion in Section 2.3.3, this means that the orbital period must initially *increase*. However, the secondary then relaxes thermally, causing ζ to increase and ultimately settle just below the MS value ($\zeta \simeq 0.6 - 0.7$). Along the way, ζ must pass through the critical value of $1/3$. As discussed in Section 2.3.3, this value separates evolution towards long periods from evolution towards short periods. The period at which $\zeta = 1/3$ is reached, P_{flag} , therefore marks the upper edge of the period flag. All of these aspects of the donor response to the re-establishment of mass loss are nicely visible in the bottom right panel of Figure 10.

In the middle panel of Figure 14, we show the predicted P_{flag} as a function of f_{MB} . Unlike P_{emerge} , P_{flag} *does* depend on the strength of the ongoing mass loss.

More specifically, Figure 14 shows that P_{flag} increases with f_{MB} . This is in line with the findings of Stehle et al. (1996). In any case, the main conclusion to draw from this panel is simply that the bottom edge of the period gap is in reasonable agreement with theoretical predictions. However, since P_{emerge} , in particular, is completely insensitive to mass loss, the level of agreement with $P_{gap,-}$ does not provide a powerful way of distinguishing between different models.

6.3. Donor Spectral Types

As discussed in Section 2.2.3, the effective temperature of low-mass stars with a large convective envelope is virtually unaffected by mass loss, so the $T_{eff,2} - M_2$ relationship of CV donors is the same as for ordinary MS stars (at least to the point where the donors become sub-stellar). Since the spectral type (SpT) of a star is essentially a direct measure of its effective temperature, the $SpT_2 - M_2$ relationship of CV donors is also the same as for MS stars. However, mass loss does drive CV donors slightly out of thermal equilibrium and causes them to be bloated compared to MS stars of identical mass. As a consequence of the period-density relationship (Equation 12), a bloated, mass-losing star will be found at longer P_{orb} than an equivalent Roche-lobe-filling MS star in thermal equilibrium. Thus, at fixed period, CV donors should have lower mass, and hence later $T_{eff,2}$ and later SpT , than Roche-lobe-filling pure MS stars (see, for example, Baraffe & Kolb 2000).

This theoretical expectation was initially verified for CVs above the gap by Beuermann et al. (1998) and later for both short- and long-period CVs by K06. In K06, we also showed that our original broken-power-law donor sequence was a good match to the empirical $P_{orb} - SpT$ relation for CV donors. Thus the degree of donor inflation represented by that sequence was just right to produce the observed later-than-MS SpT at a given period.

In Figure 15, we now compare the standard model, the best-fit model, as well as both original and updated broken-power-law sequences to the observed $P_{orb} - SpT$ relation for CV donors. The observational data here is the same as in K06, except that we have included some additional long-period CVs from Thorstensen et al. (2010). The calibration of SpT based on $V - K$ photometric colours is the same as in K06. The figure shows that all theoretical tracks – including the standard model – do a reasonable job of matching these observations. This is not unexpected, since all of these tracks produce significant amounts of donor bloating. In fact, all but the standard model are constrained by essentially the same donor mass-radius data set, so they predictably produce almost identical amounts of donor inflation. The donor bloating predicted by the standard model is slightly different – stronger above the gap, weaker below; see Figure 10 – but this difference is not large enough to produce a significant difference in the predicted $SpTs$ (at least not in the period range for which we have data).

Nevertheless, the observed $P_{orb} - SpT$ relation does confirm yet again that CV donors are significantly bloated relative to MS stars. The good agreement between predictions and observations in the $P_{orb} - SpT$ plane is therefore reassuring, even if the spectral type data is not as powerful as the observed $M_2 - R_2$ relation in distinguishing between competing models.

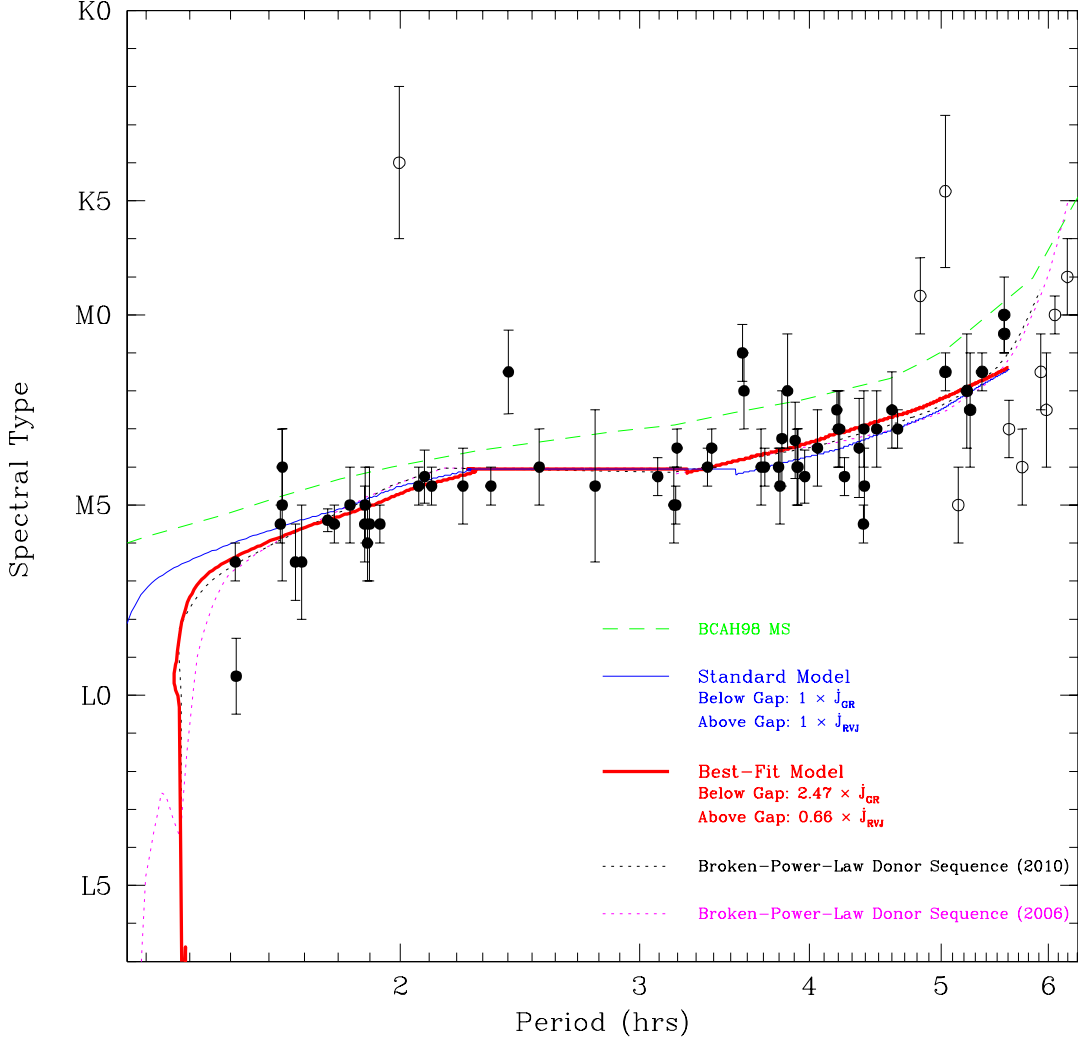


Figure 15. Observed vs. predicted spectral types of CV donors as a function of orbital period. Points correspond to empirically determined SpT 's for CVs with $P_{orb} \lesssim 6$ hrs from K06 (with a few additions noted in the text). Likely evolved donors are shown as open symbols. The green dashed line shows the evolution of SpT along a standard MS BCAH98 5-Gyr track, assuming marginal contact, i.e. not allowing for any thermal disequilibrium (see K06 for details). The thin solid blue line shows the predicted $SpT - P_{orb}$ relation for the standard model, the thick solid red line shows the same for the revised (best-fit) model. For comparison, the thin dotted black (magenta) line shows the $SpT - P_{orb}$ relation for our updated (original; K06) broken-power-law donor sequence.

6.4. White Dwarf Temperatures

A final empirical check on our evolution track is presented in Figure 16. Here, we compare a set of observed WD temperatures to the values predicted by both the standard model and our best-fit alternative. The observational data are taken mainly from the compilation provided by TG09, but supplemented by a few additional estimates from L08. Note that all of the observational estimates for dwarf novae are obtained from observations in quiescence, when the WD temperatures should best track the long-term-average accretion rate.

Taken at face value, Figure 16 suggests that neither the standard model, nor our best-fit, donor-based one, provides a particularly good match to the observed WD temperatures. The best-fit model clearly lies closer to the data, but it still systematically underpredicts the

WD temperatures in short-period, pre-bounce CVs. The simplest interpretation of this result is that the WD temperatures point to an even stronger AML enhancement over GR than is allowed for in our best-fit model. This apparent preference for faster-than-GR mass transfer is in line with the findings of TG09.

However, as also noted by TG09, considerable care needs to be taken before accepting such a conclusion. First, and most fundamentally, there is the issue already noted in Section 1: even though quiescent WD temperatures are tracers of \dot{M}_{acc} averaged over 10^3 yrs - 10^4 yrs, this time scale is short compared to the time scale on which mass-transfer-rate fluctuations associated with the donor star are expected to operate. Thus $T_{eff,1}$ may simply not trace the secular mass-transfer rate faithfully. This probably explains at least the huge scatter in the

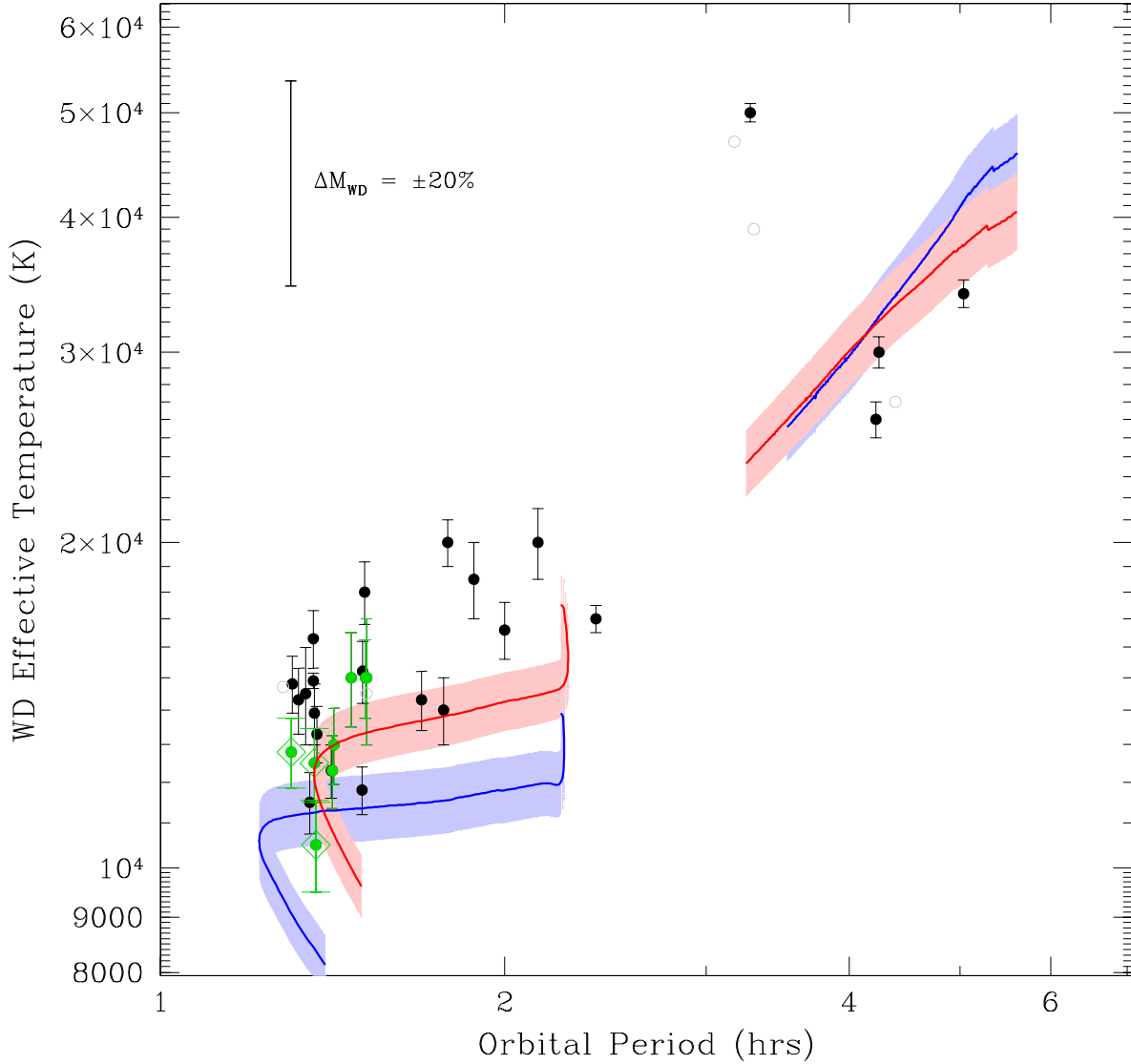


Figure 16. Predicted and observed WD temperatures as a function of orbital period. The data are mostly from the compilation by TG09, but a few additional points have been added from L08. The latter are shown in green; candidate period bouncers with sub-stellar secondaries among these are additionally marked by open diamonds. Points without error bars are more uncertain and are plotted as open circles. The thick solid blue line shows the long-term average WD temperatures predicted by the standard model ($f_{GR} = f_{MB} = 1$). The thick solid red line shows the same for the revised (best-fit) model ($f_{GR} = 2.47$; $f_{MB} = 0.66$). The shaded regions around both curves show the uncertainty in $T_{eff,1}$ associated with the mass of the non-degenerate layer (or, equivalently, with the time since the last nova eruption). The error bar in the top left of the figure shows the effect of a 20% change in M_1 on the predicted temperatures.

(sparse) set of observations above the period gap. Second, the predicted WD temperatures scale roughly as $T_{eff,1} \propto M_1 \dot{M}_{acc}^{1/4}$ (TG09), so they are quite sensitive to the assumed WD mass. No attempt has been made in Figure 16 to take this into account. In particular, both models assume our usual $M_1 = 0.75 M_{\odot}$, but the actual WD masses are not known for most of the systems plotted in Figure 16. Third, the observed sample is likely to be affected by selection effects. In particular, $T_{eff,1}$ is probably biased high in the sample, because hot WDs

are easier to detect and analyse.

The best way to mitigate at least the last two concerns is to focus on systems with well-determined $T_{eff,1}$ and M_1 . For these, the accretion rate needed to heat the WD can be estimated and compared to different models. A first attempt to do this was made by L08, based on their small sample of eclipsing, short-period CVs. They concluded that mass-transfer rates driven purely by GR – as in the standard model – provided a better match to the WD-based \dot{M}_2 estimates than an enhanced AML

model. This is a rather surprising conclusion, given the appearance of Figure 16, and we will discuss the results of L08 in more detail below (Section 8.1). However, it would clearly be important to test their conclusions by obtaining WD-based M_2 estimates for a larger sample of CVs with accurate $T_{eff,1}$ and M_1 measurements. At the moment, it may be premature to draw strong conclusions about CV evolution scenarios on the basis of WD temperatures.

7. IMPLICATIONS AND APPLICATIONS

In the previous section, we presented a semi-empirical CV evolution track based on the observed mass-radius relationship of CV donor stars. The inferred AML rates along our best-fit track are somewhat lower (higher) than in the standard model of CV evolution above (below) the period gap. We also compared its properties to observed donor spectral types, the locations of the period gap edges, the location of the period minimum and to observed WD temperatures. Overall, our donor-based best-fit track appears to match these observed properties of CV significantly better than the standard model. With the construction and testing of the donor-based track concluded, it is time to consider some of its implications and applications for observational and theoretical studies of CVs. This is the goal of the present section. In Section 7.1, we will show how (lower limits on) distances towards CVs can be estimated via simple donor-based photometric parallax in the near-infrared (NIR). In Section 7.2, we will compare the predicted mass-transfer rate along the track to the critical rate for the occurrence of dwarf nova outbursts. Finally, in Section 7.3, we will calculate the approximate orbital period distribution predicted by our donor-based evolution scenario and compare this to both the standard model prediction and observations.

7.1. Donor-Based Photometric Parallax

The physical and photometric properties of CV donors are expected to change only on the secular evolution time scale. At fixed P_{orb} , they are also quite insensitive to the detailed system parameters, thanks largely to the period-density relationship (Equation 12). Thus all unevolved CV donors at the same orbital period should be quite similar. This makes them potentially quite useful as distance indicators via photometric parallax, provided their absolute magnitudes are reliably known as a function of P_{orb} .

The absolute magnitude of a star is primarily a function of its radius and effective temperature. Thus our semi-empirical donor sequences – which were constructed by fitting the observed mass-radius relationship of CV secondaries and tested against their observed $SpTs$ – should predict the absolute donor magnitudes at given P_{orb} quite well. As discussed in more detail in K06, we can therefore use these sequences to obtain lower limits on the distance towards any CV with an unevolved donor star. For example, the lower limit on the distance associated with a single epoch K -band measurement is

$$\log d \geq \frac{K - M_{K,2}(P_{orb}) + 5}{5}, \quad (32)$$

where K is the apparent magnitude and $M_{K,2}$ is the absolute K -band magnitude on the relevant donor sequence

at the CV's orbital period. In principle, the apparent magnitude should be extinction-corrected, but in practice this correction is usually negligible for CVs in the infrared.

This method only yields a lower limit on the distance, because the fractional contribution of the donor to a single photometric measurement is unknown. If an actual measurement of the *donor's* apparent magnitude is available, K in Equation 32 should be replaced with K_2 , and the lower limit becomes an actual estimate of the distance.

In K06, we tested and calibrated this method for our original broken-power-law donor sequence. Thus we compared the predicted NIR donor absolute magnitudes along this track to the absolute magnitudes for CVs with distances determined by trigonometric parallax. Figure 17 shows the same comparison for our updated broken-power-law donor sequence (Section 3) and for the best-fit, self-consistent CV evolution track (Section 6). For reference, we also show the donor properties predicted by the standard model ($f_{MB} = f_{GR} = 1$). The observational data set is the same as in K06.

We already know from Figure 13 that all of these sequences – including the original broken-power-law one – predict very similar donor absolute magnitudes for pre-bounce CVs with $P_{orb} \gtrsim 90$ min. In line with this, we find that the scatter in the observational data is considerably larger than any differences between the models. None of the sequences are inconsistent with these observations. The model tracks all trace a lower envelope around the data points, as expected since the observed magnitudes may include substantial contributions from system components other than the donor star (e.g. the accretion disk). The predicted donor magnitudes do differ quite significantly in the period bounce regime, but here the stellar atmosphere models become unreliable anyway (see discussion in Section 5.4), and even the WD starts to compete with or outshine the donor in the NIR (Figure 13).

As in K06, we have estimated the average offsets (ΔJ , ΔH , ΔK) between the donor tracks and the data, as well as the scatter around the tracks if these offset are applied ($\sigma_J, \sigma_H, \sigma_K$). The results are listed in Table 9 and are very similar to those given in K06 for the original broken-power-law donor sequence. More specifically, for the small sample of CVs shown in Figure 17, the donor contribution to the total NIR light is about 23% in J, 29% in H, and 31% in K. Thus, to the extent that this sample is representative, lower limits on CV distances (e.g. Equation 32) will typically underestimate the true distance by about a factor of about 2.1 (J), 1.9 (H) and 1.8 (K). If such lower limits are converted into actual distance estimates by applying these factors, the resulting values will be uncertain by *at least* a factor of about 1.9 (J), 1.8 (H) and 1.7 (K). The real uncertainties could be even larger, both because our small and heterogenous sample of CVs with trigonometric parallaxes may not be representative, and also because there is no reason to think that the typical donor contributions are actually constant along the entire CV evolution track. The specific numbers quoted above are for the best-fit self-consistent evolution track, but the other sequence give similar estimates.

Given that we have also calculated predicted WD tem-

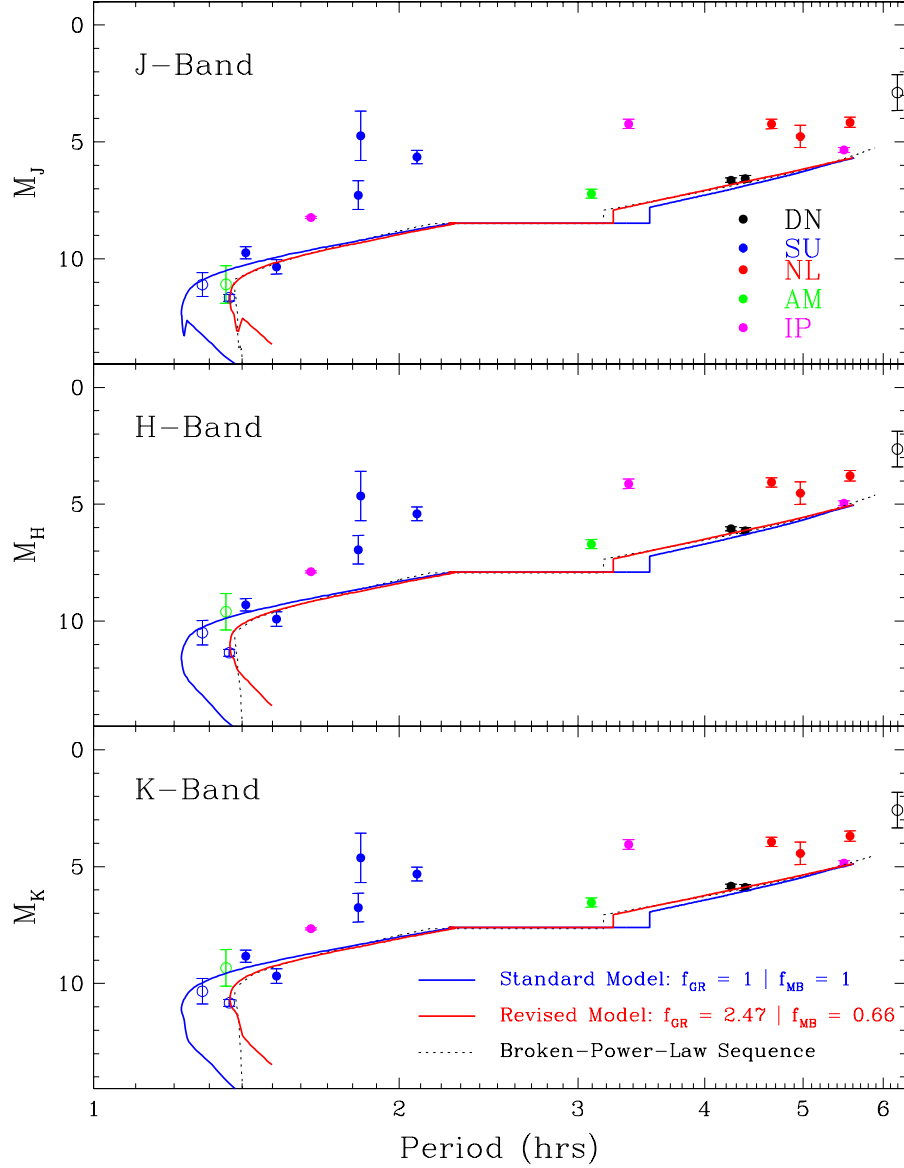


Figure 17. Infrared absolute magnitudes of CVs as a function of P_{orb} . Points correspond to absolute magnitudes for CVs with trigonometric parallaxes and reliable 2MASS observations, taken from K06. Colours correspond to various CV sub-types, as indicated (DN = dwarf nova; SU = SU UMa star; NL = non-magnetic nova-like; AM = AM Her star; IP = intermediate polar). Systems with $P_{orb} < 82.4$ min or $P_{orb} > 6$ hrs are shown as open symbols and were excluded in calculating the quantities listed in Table 9. The thick solid blue line shows the track predicted by the standard model ($f_{GR} = f_{MB} = 1$), the thick solid red line that predicted by the revised (best-fit) model ($f_{GR} = 2.47$; $f_{MB} = 0.66$). For reference, the track predicted by our updated broken-power-law donor sequences is also shown as a thin dotted black line.

peratures and absolute magnitudes along our evolution tracks, it is reasonable to ask if improved distance estimates could be obtained by, for example, replacing $M_{K,2}$ in Equation 32 with the predicted absolute magnitude of primary and secondary *combined*. This may also seem to be a sensible way of extending the usefulness of the method to shorter wavelengths, where the WD contribution can be dominant at all orbital periods. However, we think the drawbacks of such an approach would outweigh its benefits. In particular, as discussed in Section 4, mass-transfer-rate fluctuations may cause WD temper-

atures (and hence brightnesses) to vary on time scales longer than $\sim 10^5$ yrs, but still shorter than the evolutionary time scale. As a result, and unlike for donor stars, it is not clear that the absolute magnitude of a WD in a CV can be reliably predicted solely on the basis of the system’s orbital period. If additional information is available – e.g. if the WD is detected spectroscopically (e.g. Knigge et al. 2000; Howell et al. 2002; Araujo-Betancor et al. 2003, 2005; Long et al. 2009) or via eclipses in multiple photometric bands (e.g. L08) – excellent WD-based distance estimates can, of course, nevertheless be

obtained. However, as a simple tool for setting reliable distance limits based solely on P_{orb} and a single-shot NIR magnitude, the pure donor sequence is hard to beat.

7.2. Disk (In)stability: The Parameter Space of Dwarf Novae

7.2.1. Motivation and Observational Background

As noted in Section 4, one of the reasons for suspecting CV mass-transfer rates must vary on unobservably long time scales is the fact that different *types* of CVs can apparently co-exist at the same orbital period. It is interesting to explore this argument in more detail. In particular, does it still hold for our new best-fit evolution track?

According to the widely accepted disk instability model (DIM; e.g. Osaki 1996; Lasota 2001) the key difference between nova-likes and dwarf novae is the rate at which mass is supplied to the disk, \dot{M}_{disk} . If this is above a certain critical rate, $\dot{M}_{crit,hi}$, the disk is bright and stable, and the system is a nova-like CV. Otherwise the system is unstable and cycles as a dwarf nova between high- and low-states. (Actually, there is also a lower critical rate, $\dot{M}_{crit,lo}$, below which the system is stable again. However, unless the inner disk is truncated well before reaching the WD surface, this rate is far below even the purely GR-driven \dot{M}_2 ; see Equation 34 below.)

Now the critical rate of mass supply to the accretion disk, $\dot{M}_{crit,hi}$, does depend on the system parameters, but only weakly so at fixed P_{orb} (see Equation 33 below). Similarly, we know that unevolved CVs are expected to follow a unique evolutionary track (see Section 2.2.2), with only minor sensitivity of \dot{M}_2 to other system parameters at given P_{orb} . It therefore follows that if $\dot{M}_{disk} = \dot{M}_2$, the unevolved CV population at any given P_{orb} should be strongly dominated by either dwarf novae or nova-likes. A population mix in which both types contribute significantly should only be possible near orbital periods where $\dot{M}_2(P_{orb})$ crosses $\dot{M}_{crit}(P_{orb})$, or is at least very close to it.

What is the observational situation? The top panel of Figure 18 shows the orbital period distribution of all non-magnetic CVs in the Ritter & Kolb (2003) catalogue (version 7.11) compared to that of just the dwarf novae.²⁶ The bottom panel shows the corresponding dwarf nova fraction, i.e. the fractional contribution of dwarf novae to the non-magnetic CV population as a function of P_{orb} . The short-period CV populations is essentially 100% dominated by dwarf novae. However, the dwarf nova fraction then drops steadily through the period gap, reaches a minimum value of about 0% just above the gap, and then rises again to a value of about 75% beyond periods of about 4 hrs. Thus, in apparent violation of naive theoretical expectations, significant populations of dwarf novae and nova-likes happily co-exist above the period gap. As noted above, this has been interpreted as evidence for mass-transfer-rate fluctuations on unobservably long time scales.

²⁶ It should be acknowledged that the type assignments in the Ritter & Kolb catalogue are not necessarily all that secure, especially for little-studied systems. However, they are probably reliable enough for the basic statistical analyses carried out in this section.

7.2.2. Critical vs. Secular Mass-Transfer Rates

Let us now consider the theoretical picture. After all, the simplest explanation for the co-existence of dwarf novae and nova-likes would be that the upper edge of the period gap is a crossing point for $\dot{M}_2(P_{orb})$ and $\dot{M}_{crit,hi}(P_{orb})$. In this case, differences in WD mass, or perhaps a modest amount of intrinsic dispersion in \dot{J}_{sys} (perhaps reflecting the initial donor mass or system age) could be sufficient to explain the observations.

With this in mind, Figure 19 shows direct comparisons of $\dot{M}_2(P_{orb})$ and $\dot{M}_{crit}(P_{orb})$ for both the standard model of CV evolution (top panel) and our new best-fit model (bottom panel). A very similar comparison was first shown in Shafter (1992). The critical accretion rates adopted here are based on the “grey atmosphere” approximation and taken from Hameury et al. (1998), i.e.

$$\begin{aligned}\dot{M}_{crit,hi} &= 8.0 \times 10^{15} \alpha_{hot}^{0.03} \left(\frac{M_1}{M_\odot} \right)^{-0.89} \left(\frac{R_{disk}}{10^{10} \text{cm}} \right)^{2.67} \\ \dot{M}_{crit,lo} &= 4.0 \times 10^{15} \alpha_{cold}^{-0.04} \left(\frac{M_1}{M_\odot} \right)^{-0.89} \left(\frac{R_1}{10^{10} \text{cm}} \right)^{2.67},\end{aligned}\tag{33}$$

where α is the usual viscosity parameter. We adopt $\alpha_{hot} = 0.3$, $\alpha_{cold} = 0.03$ and, as usual, $M_1 = 0.75 M_\odot$. We further assume that the disk radius is given by $R_{disk} = 0.7 R_{L,1}$, based on the empirical study of Harrop-Allin & Warner (1996), and take $R_1 = 0.01 R_\odot$, as appropriate for our adopted WD mass.

In one sense, the theoretical curves are quite promising. For both models, systems below the gap are predicted to be firmly in the unstable regime, as is indeed observed. And above the gap, the differences between $\dot{M}_2(P_{orb})$ and $\dot{M}_{crit,hi}(P_{orb})$ are less than a factor of 3 everywhere. However, there are also two glaring inconsistencies. First, both models predict that most unevolved systems above the gap should be unstable, at least out to $P_{orb} \simeq 5$ hrs.²⁷ Yet, observationally, nova-likes dominate this distribution out to about 3.8 hrs. Second, the *sense* in which the DN fraction changes above the period gap is exactly opposite to what one might expect theoretically. Both models predict that CVs should become increasingly stable as we move towards larger P_{orb} above the period gap. Thus the dwarf nova fraction is expected to *decrease*. However, the observed dwarf nova fraction actually *increases* (from 0% to 75%) between $P_{orb} \simeq 3$ hrs and $\simeq 4$ hrs.

7.2.3. Reconciling Theory and Observation

How can these discrepancies be resolved? The often-invoked mass-transfer rate fluctuations – be they driven by irradiation (Section 4.2.1) or nova eruptions (Section 4.2.2) – offer one possibility. Most nova-likes below $P_{orb} \simeq 4 - 5$ hrs would then have to be systems caught in the high state of such a cycle. In addition, the dearth of dwarf novae in the period range just above the gap would imply that low-state systems there must be essentially unobservable. Similarly, the absence of nova-likes

²⁷ And this is the period range that matters, since beyond this evolved CVs may be expected to dominate the observed population in any case (Podsiadlowski et al. 2003).

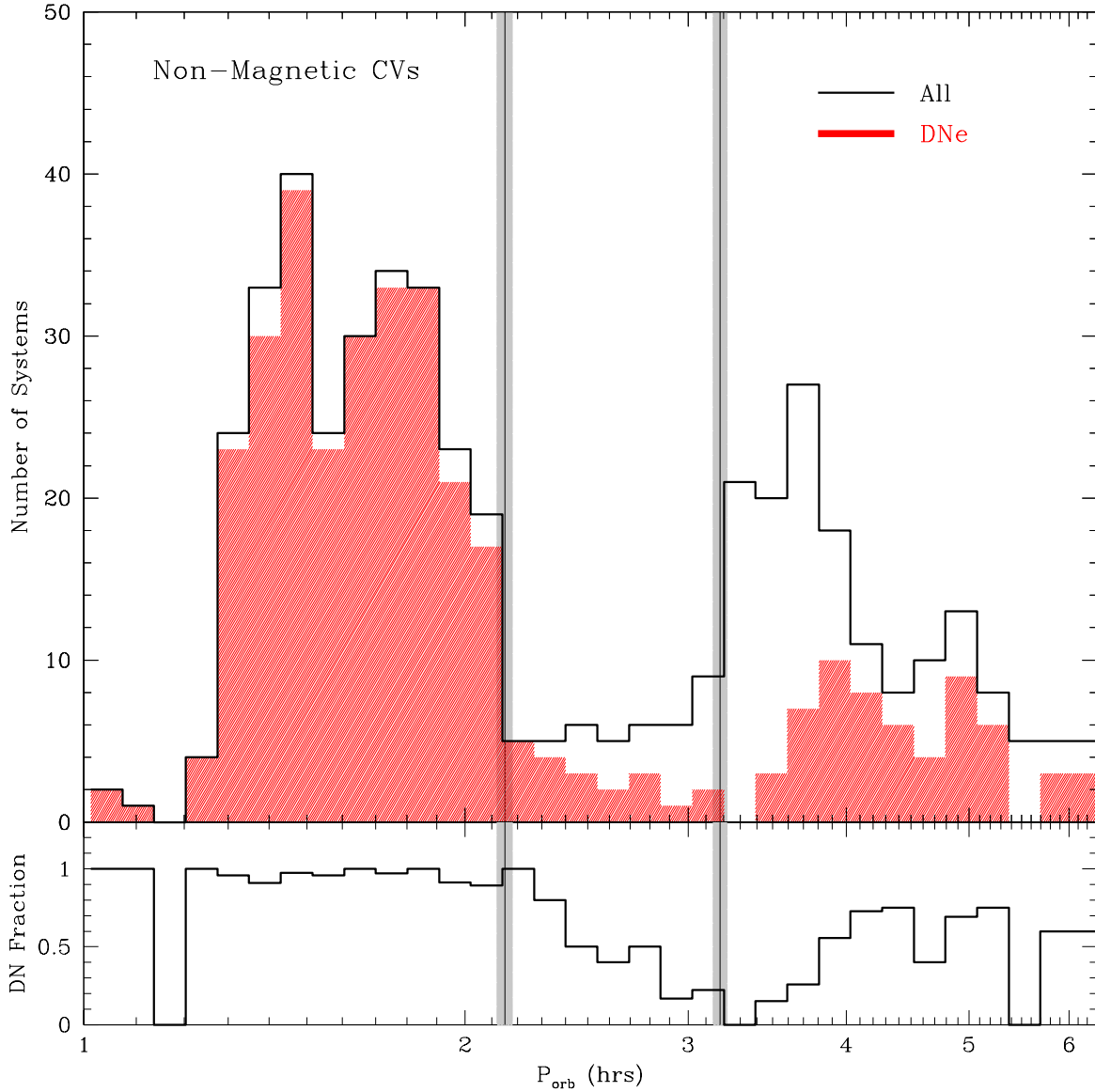


Figure 18. The orbital period distribution of non-magnetic CVs and the associated dwarf nova fraction. *Top panel:* The solid black histogram shows the orbital period distribution of all non-magnetic CVs in the Ritter & Kolb catalogue (v7.11). The red-shaded histogram shows the subset of dwarf novae within this sample. *Bottom panel:* The dwarf nova fraction – defined as the ratio of dwarf novae to all non-magnetic CVs within a given period bin – is shown as a function of orbital period. In both panels, the vertical lines and grey shaded regions mark the location of the upper and lower period gap edges, along with their errors.

below the period gap would imply that, if such cycles exist at all in this period range, the mass-transfer rate in the high state must be less than $\dot{M}_{crit,hi}(P_{orb})$. Based on Figure 19, the high-state mass-transfer rate could thus be at most $\simeq 10$ -times higher than the secular $\dot{M}_2(P_{orb})$.

However, mass-transfer-rate fluctuations are not the only possible way to account for the discrepancy between observed and predicted dwarf nova fractions above the period gap. Errors or uncertainties in $\dot{M}_2(P_{orb})$ and/or $\dot{M}_{crit,hi}(P_{orb})$ could, in principle, also be to blame.

Let us first assume that $\dot{M}_{crit,hi}(P_{orb})$ is correct. Is it

possible that we could have achieved an acceptable fit to the observed $M_2 - R_2$ data with a functional for $\dot{M}_2(P_{orb})$ that would better match the observed dwarf nova fraction? Given that we would like systems to be most stable just above the gap, Figure 19 implies that this would require \dot{M} to be a flat or decreasing function of P_{orb} . Based on the preliminary tests we carried out before settling on a functional form for $\dot{M}_2(P_{orb})$ (Section 5.3), such models would produce a significantly worse fit to the data. However, the mass-radius data set above the gap remains fairly sparse, and additional measurements are highly desirable to tie down the exact form of AML

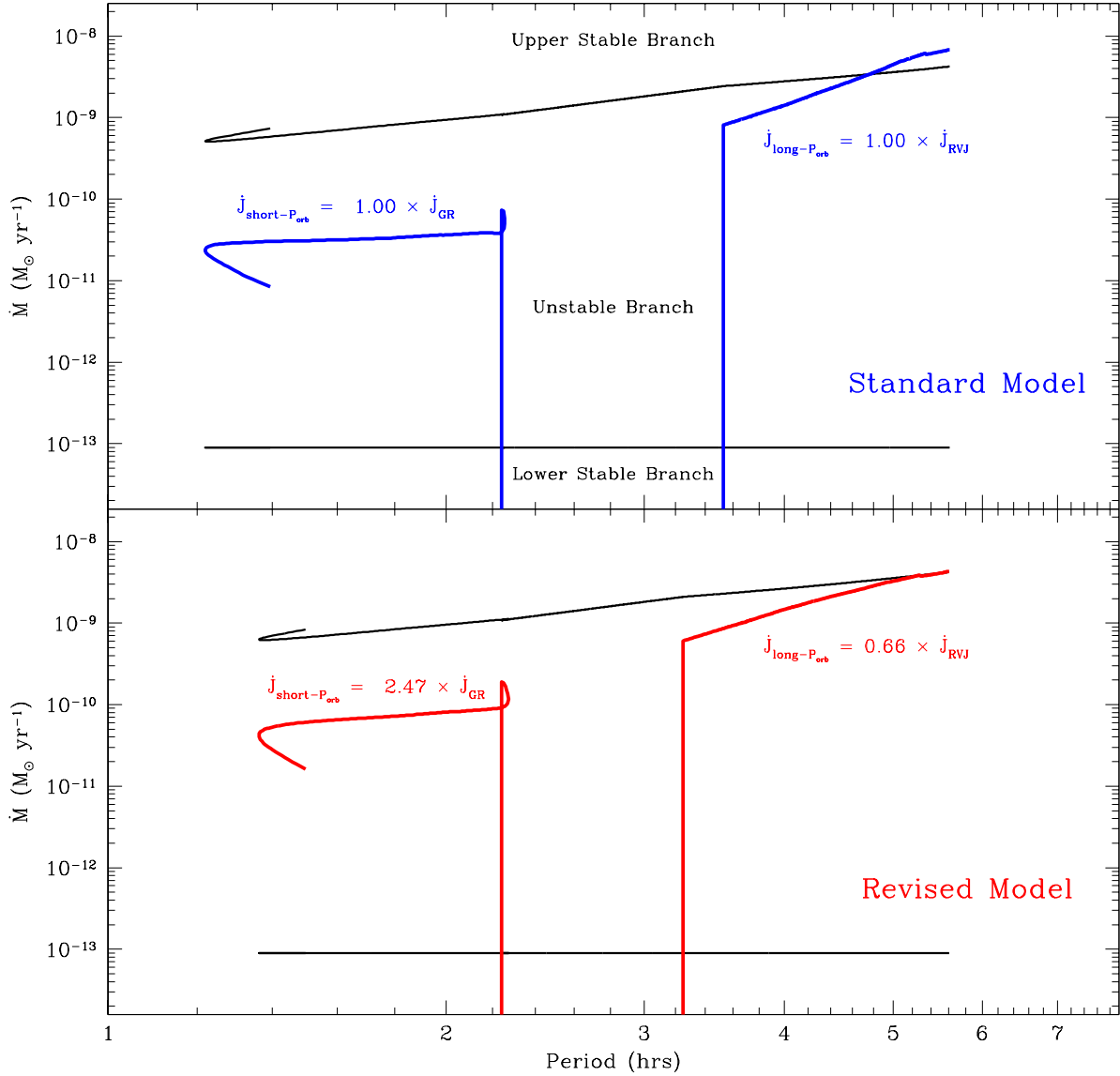


Figure 19. A comparison of the predicted mass-transfer rates along our self-consistent evolution sequences and the critical rates for the occurrence of dwarf nova eruptions. *Top panel:* The thick solid blue line shows the run of \dot{M}_2 as a function of P_{orb} according to the standard model of CV evolution ($f_{\text{GR}} = f_{\text{MB}} = 1$). The thin solid black lines show the corresponding upper and lower boundaries of the unstable region in the $P_{\text{orb}}-\dot{M}_2$ plane, as predicted by the thermal disk instability model (Equations 33 and 34). Only CVs between these two regions are expected to be unstable, i.e. to undergo dwarf nova eruptions. *Bottom panel:* Same as top panel, but here the thick solid red line shows the revised model track ($f_{\text{GR}} = 2.47$, $f_{\text{MB}} = 0.66$).

above the gap.

What about $\dot{M}_{\text{crit},hi}(P_{\text{orb}})$? The disk instability model on which Equation 33 is based has been around for several decades and, overall, has been very successful (e.g. Osaki 1996; Lasota 2001). However, Equation 33 is only an approximation to numerical results that themselves depend on various assumptions. Perhaps most importantly, it does not include the heating of the outer disk that may be expected due to tidal dissipation and irradiation (e.g. Stehle et al. 2001; Buat-Ménard et al. 2001). Depending on the system parameters, this can lower the

$\dot{M}_{\text{crit},hi}(P_{\text{orb}})$ by a factor of several (Buat-Ménard et al. 2001), which might be enough to push the predicted $\dot{M}_2(P_{\text{orb}})$ into the stable regime above the period gap.²⁸ It is not clear if such an adjustment would tend to stabilize *all* unevolved, long-period CVs. Even if it did,

²⁸ However, it is also worth noting that there is at least one well-known, long-period dwarf nova – the famous SS Cygni – that manages to be unstable despite apparently satisfying $\dot{M}_2(P_{\text{orb}}) > \dot{M}_{\text{crit},hi}(P_{\text{orb}})$ by a wide margin (regardless of whether outer disk heating is accounted for; Schreiber & Gänsicke 2002; Schreiber & Lasota 2007).

the rise in the dwarf nova fraction with increasing P_{orb} could perhaps still be understood. It might simply reflect the increasing contribution of evolved systems to the observed population, since these are indeed expected to have lower \dot{M}_2 at given P_{orb} than unevolved systems (Podsiadlowski et al. 2003).

Finally, Stuart Littlefair has suggested another possible explanation to us: according to some recent studies of MB in non-interacting stars (Barnes 2003, 2007; Irwin et al. 2007; Barnes 2010, also see discussion in Section 8.5), even partly radiative stars begin their life with spin-down rates comparable to fully convective stars. They only switch to a faster, Skumanich-like spin-down sequence on a mass-dependent time-scale that can reach $\simeq 1$ Gyr. This raises the possibility that there could be genuine \dot{J}_{sys} and \dot{M}_2 differences above the period gap, with the “hidden parameters” being the initial donor mass and/or the age of the system. It is not clear to us if this idea can be reconciled with the absence of significant scatter in the $\dot{M}_2 - R_2$ relation above the period gap, but the data is still somewhat sparse in this regime. In any case, this is an interesting possibility that deserves to be explored more carefully.

Where does all of this leave us? In our view, the comparison of Figures 18 and 19 does reveal a clear and interesting discrepancy between theory and observation. This discrepancy affects both the standard model of CV evolution and our new best-fit donor-based one, so it cannot be used to distinguish between them. Long-term mass-transfer-rate fluctuations provide one possible explanation for the observations, but so do uncertainties in the $\dot{M}_{crit,hi}$ and – perhaps – also uncertainties in the form of \dot{M}_2 . Thus, on its own, the co-existence of dwarf novae and nova-likes above the period gap provides at most circumstantial evidence for long-term mass-transfer-rate fluctuations.

7.2.4. Coda: The Surprising Decline of Dwarf Novae in the Period Gap

There is one final feature of Figure 18 that deserves comment: the smooth and monotonic drop in the dwarf nova fraction from $\simeq 100\%$ to $\simeq 0\%$ inside the period gap is actually rather surprising. In the disrupted MB framework, the existence of CVs in the gap is explained by noting that some systems will necessarily first come into contact within the gap (e.g. Howell et al. 2001). Such systems will typically have fully convective secondaries with masses $0.2M_\odot < M_2 < 0.35M_\odot$, and, in the standard model, will evolve through the gap as purely GR-driven systems. More generally, they are essentially short-period CVs that find themselves within the gap by an accident of birth. However, this immediately implies that, just like other short-period systems, CVs within the period gap would be expected to be located firmly within the unstable domain in Figure 19. The dwarf nova fraction would therefore be expected to be close to 100% throughout the period gap, followed by a sharp cut-off at the upper gap edge. This is not what is observed.

One possible explanation is that the CV population within the gap includes a significant proportion of MB-driven systems with slightly lower metallicity secondaries. Such donors are expected to become fully convective at shorter P_{orb} than their solar metallicity coun-

terparts. As a result, stable, long-period, low-metallicity CVs may “invade” the period gap from above (Stehle et al. 1997; Webbink & Wickramasinghe 2002).

7.3. Orbital Period Distributions

7.3.1. Motivation and Construction

We have already seen that the best-fit donor-based evolution track successfully predicts the observed location of the period minimum, thus resolving one of the long-standing conflicts between the standard model of CV evolution and observations (Section 2.3.3). A similar conflict exists concerning the ratio of long-period CVs to short-period, pre-bounce CVs, with the standard model predicting a far lower ratio than is observed, even after allowing for selection effects (Pretorius et al. 2007a; Pretorius & Knigge 2008a,b). Does the revised donor-based model resolve this conflict as well?

Intuitively, it is reasonable to hope that it might. Relative to the standard model, the best-fit donor-based evolution track is characterized by a slower AML rate above the gap and a faster one below. CVs evolving along the best-fit track may therefore be expected to spend a relatively larger fraction of their lives above the period gap. Other things being equal, this should lead to a higher fraction of long-period systems in the predicted CV population.

A full population synthesis calculation (as carried in out various CV contexts by Kolb 1993; Howell et al. 1997, 2001; Politano 2004; Willems et al. 2005) would be required to properly verify and quantify this prediction, and any quantitative comparison with observed period distributions would also have to carefully deal with selection effects (Pretorius et al. 2007a). This is well beyond the scope of our present, already overlong study.

Here, we instead limit ourselves to the simplest possible population models that can be constructed from our evolution tracks. Thus we assume that all CVs in our model populations have $M_1 = 0.75 M_\odot$ and start their life as CVs with $M_2 = 0.6 M_\odot$ at $P_{orb} \simeq 5.6$ hrs. We also adopt a constant CV formation rate over the age of the Galactic disk, for which we take $t_{gal} = 10$ Gyr; we assume that the pre-CV evolution phase is negligibly short compared to t_{gal} . With these assumptions, the number of CVs expected in a given orbital period bin is simply proportional to the total amount of time a single CV evolving from $t = 0$ to $t = t_{gal}$ spends inside this bin. The distribution is normalized by taking the theoretical CV birth rate density to be $2 \times 10^{-15} \text{ yr}^{-1} \text{ pc}^{-3}$ (Politano 1996). This is $5\times$ lower than the estimate given by de Kool (1992), but yields a CV space density ($\simeq 2 \times 10^{-5} \text{ pc}^{-3}$) that is in better agreement with observations (e.g. Patterson 1998; Pretorius et al. 2007b). We also take the space density to be constant throughout whatever volume we consider.

7.3.2. Basic Results

The resulting theoretical orbital period distribution for both the standard and the best-fit model are shown in Figure 20; some associated statistics are listed in Table 10. It should be obvious that these distributions are highly approximate and should not be compared directly to observations. For example, the age-dependent scale height of the Galactic disk should really be taken into ac-

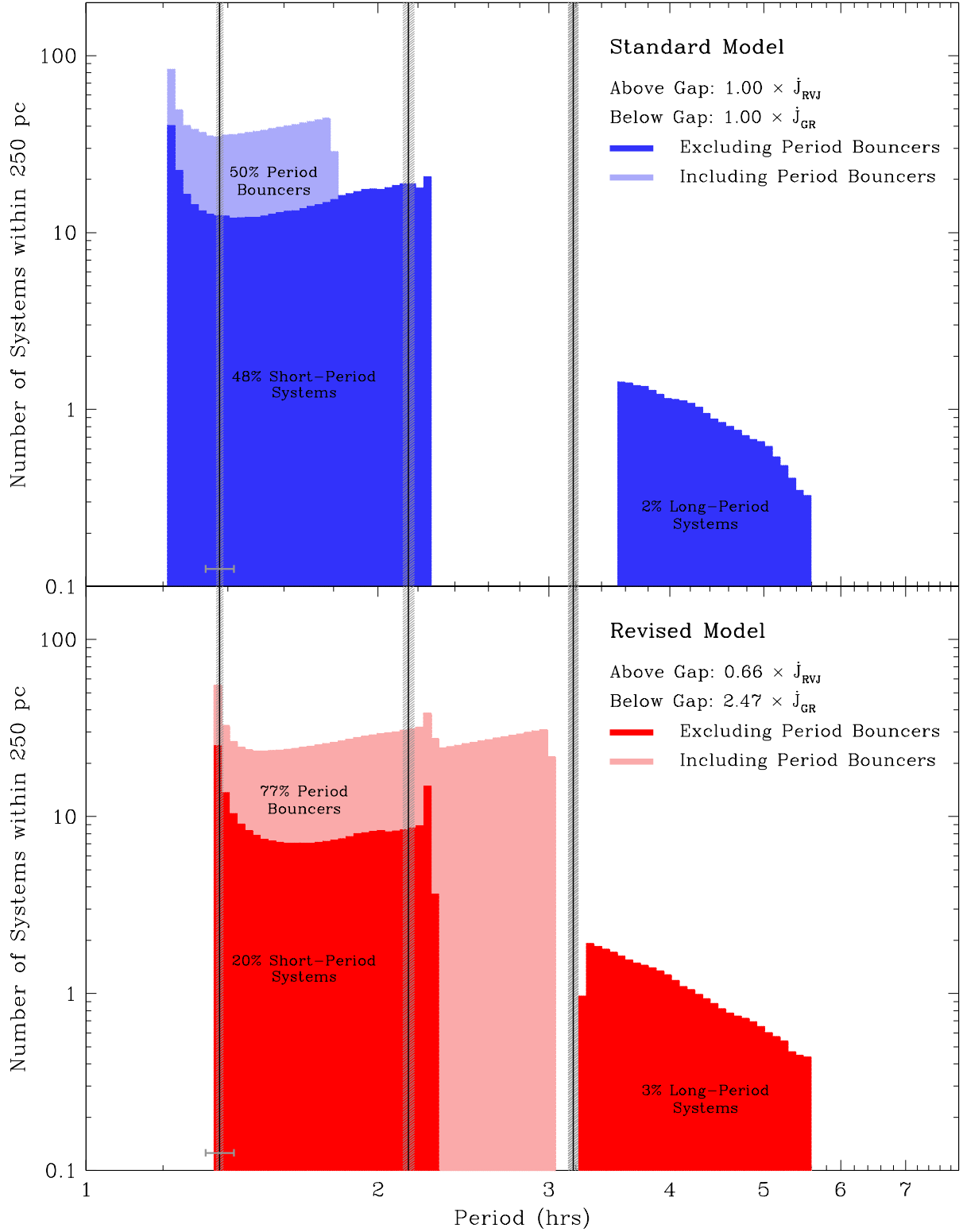


Figure 20. Approximate period distributions calculated for the standard model ($f_{GR} = f_{MB} = 1$; the blue-shaded histogram in the top panel) and for the revised best-fit model ($f_{GR} = 2.47$, $f_{MB} = 0.66$; the red-shaded histogram in the bottom panel). The contributions of period bouncers to the overall distributions are shown separately by light shaded regions. The vertical lines show the observed locations of the minimum period (as estimated from the recently discovered period spike [Gänsicke et al. 2009]), and of the lower and upper edges of the period gap (K06). The grey shaded regions around these lines are the errors on these quantities. The error bars shown near the bottom of each panel on top of the P_{min} estimate show the intrinsic FWHM of the period spike. Note that these predicted period distributions are highly approximate and purely illustrative. In particular, they assume that all CVs are born at $P_{orb} \simeq 6$ hrs above the gap (see text for details).

count in such comparisons (Pretorius et al. 2007a). Perhaps more importantly, our distributions ignore the fact that CVs are expected to be borne with a wide range of ages and orbital periods (de Kool 1992; Politano 1996). In fact, the CV birthrate distribution itself will be different for different evolution tracks, since the rate at which detached systems are driven into contact depends on the adopted AML rates. However, our approximate theoretical distributions are nevertheless useful. First, their very simplicity makes them easy to interpret and thus helps to build intuition. Second, *differential* comparisons between competing models are likely to be less affected by our simplifications than direct comparisons to observational data. Third, the qualitative impact of relaxing our most restrictive assumptions is generally easy to predict.

With these points in mind, what do the predicted period distributions tell us? Perhaps most importantly, the predicted ratio of long-period to short-period, pre-bounce CVs ($f_{l:s}$) is indeed higher in the best-fit model ($f_{l:s} = 0.125$) than in the standard model ($f_{l:s} = 0.042$), by a factor of 3.0. This is in reasonable agreement with the naive expectation that this ratio should reflect the change in the relative AML normalizations between the two models ($2.47/0.65 = 3.8$). The agreement is not perfect, because rescaling \dot{J}_{MB} and \dot{J}_{GR} is not exactly equivalent to rescaling \dot{P}_{orb} . In any case, this predicted factor of 3 increase in the relative abundance of long-period CVs should be fairly robust. This is promising, as just such a factor may be required to reconcile theory with observations (Pretorius & Knigge 2008b).

7.3.3. Normalization and Space Densities

The normalization we have adopted for our period distributions yields quite reasonable numbers. For example, Table 10 shows that the best-fit (standard) model predicts $\simeq 3$ ($\simeq 2$) long-period and $\simeq 16$ ($\simeq 35$) short-period, pre-bounce CVs within 100 pc. Observationally, there are two known long-period, non-magnetic nova-like systems with $P_{orb} \lesssim 6$ hrs that *might* fall within this volume: IX Vel (Perryman et al. 1997; Linnell et al. 2007) and V3885 Sgr (Perryman et al. 1997; Linnell et al. 2009). Both have $d \simeq 100$ pc as measured by Hipparcos. Only two other nova-likes are comparably bright, and neither is likely to be as close. For reference, those objects are RW Sex (Beuermann et al. 1992; Perryman et al. 1997; Linnell et al. 2010) and TT Ari (Gänsicke et al. 1999). Amongst the long-period dwarf novae with $P_{orb} < 6$ hrs, only the famous U Gem is likely to lie within $d < 100$ pc (Harrison et al. 2000; Beuermann 2006). All three of these objects are 9^{th} - 10^{th} magnitude objects (in the case of U Gem, this is the magnitude at the peak of an outburst). So one might hope that this small sample of nearby long-period CVs is reasonably complete. On the short-period side, the recent compilation of Patterson (2009) includes 6 short-period dwarf novae with estimated distances of $d \leq 100$ pc. However, these systems can be much fainter and may erupt infrequently, so incompleteness may be a serious issue here. Given all the uncertainties that affect the predicted and observed numbers, we will not attempt to draw conclusions about the relative merits of the two models on this basis. However, a more general point *can* be made with some confidence: it would clearly be hard to rec-

oncile either model with space densities at the high end of theoretical predictions, i.e. $\rho_{cv} \gtrsim 10^{-4} \text{ pc}^{-3}$ (de Kool 1992). This qualitative conclusion agrees quite well with the quantitative estimate $\rho_{cv} = 1.1_{-0.7}^{+2.3} \times 10^{-5} \text{ pc}^{-3}$ derived by Pretorius et al. (2007b) from a small, but purely flux-limited, X-ray-selected sample.

7.3.4. The Shapes of the Period Distribution and the Spike at the Lower Gap Edge

Turning to the *shapes* of the orbital period distributions, we note that these are quite similar for both models. This similarity reflects the identical functional forms we adopted for the AML laws in the models. The two most obvious differences are the wider long-period CV distribution in the best-fit model, and the much longer maximum P_{orb} it predicts for the period bouncer distribution. The first difference arises simply because the upper gap edge is located at a shorter period in the best-fit model, the second because faster-than-GR evolution below the gap allows donors to evolve much further within t_{gal} .

A less obvious, but interesting difference is the period spike seen at the lower edge of the period gap in the best-fit model. This arises for essentially same reason as the period spike at P_{min} . As explained in Section 6.2, a system emerging from the period gap is expected to briefly evolve to longer periods, as the donor adjusts itself the mass loss it suddenly experiences, before settling down onto the standard evolution track that takes it to shorter periods and, ultimately, P_{min} . As a result, $\dot{P}_{orb} = 0$ at the upper limit of the period flag. Both the period flag itself and the associated local minimum in $|\dot{P}_{orb}|$ are nicely visible in Figure 11. Just as for the period spike at P_{min} , we might therefore expect the upper limit of the period flag to be marked by a local maximum in the CV period distribution.

The real question, however, is why this second period spike is so obvious in the best-fit model, but effectively absent in the standard model. The answer turns out to be linked to fundamental stellar physics. As discussed in Section 2.2.2, Stehle et al. (1996) showed that the time it takes a donor to adjust its radius following the (re)-establishment of mass loss is $\tau_{per} \simeq 0.05\tau_{kh,eq}$. However, they also estimated the time it takes the system to then reach the upper limit of the period flag, which turns out to be $\tau_{flag} = \frac{2}{3\zeta_{eq}}\tau_{per} \simeq \tau_{per}$. This result implies that the amount of time a CV spends on the increasing-period branch of the period flag is, to a first approximation, fixed solely by the stellar equilibrium properties. As noted by Stehle et al. (1996), this is indeed what is seen in numerical calculations, and indeed it is what we see in our models. Once the system has passed the upper limit of the period flag, normal CV evolution on the AML time scale gradually takes over.

What does all of this mean for the predicted strength of the period spike at the lower gap edge? If $\tau_{flag} \ll \tau_{ev}$, the turn-around happens too quickly to leave its imprint on the period distribution. Conversely, if $\tau_{flag} \geq \tau_{ev}$, the time it takes to execute the period flag is at least comparable to the evolutionary time scale, so a clearly visible spike should be expected. *Thus the period spike at $P_{gap,-}$ can, in principle, be used as a direct observational tracer of the AML rate below the gap (since this is what*

determines τ_{ev}).

A key point here is that, in predicted CV populations normalized to the same total number of systems, the number of CVs contributing to the spike is purely a property of stellar properties on the MS. In particular, it is invariant under changes in the AML rate. The visibility of the spike is therefore actually driven by the numbers of CVs found in adjoining period bins, since these do depend on the local AML rates. More specifically, as the AML rate below the gap is increased, CV numbers in orbital period bins just below $P_{gap,-}$ drop and eventually reveal the spike. This is exactly what is observed in Figure 20.

In reality, the situation is considerably more complicated, of course. One issue is that the predicted strength of the spike will depend on the CV birthrate distribution. More specifically, the population of CVs born with $P_{orb} < P_{gap,-}$ will add to the “continuum” of short-period systems below the spike and reduce the spike’s visibility. Another complication is that the spike is only a measure of the *instantaneous* mass- and angular momentum-loss rate at $P_{gap,-}$, immediately following the re-establishment of contact. Given that the exact shape of the AML law is not determined very precisely by the donor mass-radius data, it may be fairly straightforward to modify the adopted shape to increase or decrease the visibility of the spike.

Is there any observational evidence for a spike at $P_{gap,-}$ in the CV period distribution? Realistically, the only CV sample currently worth checking for this is that provided by the SDSS (Szkody et al. 2002, 2003, 2004, 2005, 2006, 2007, 2009). At present, this does not appear to show evidence for such a spike (see Figure 2 of G09). However, the data is still quite sparse, and even the period gap itself remains poorly defined in the SDSS sample.

7.3.5. The Spectre of Mass-Transfer-Rate Fluctuations

One final can of worms we can’t help but open concerns the potential impact of long-term mass-transfer-rate fluctuations (Section 4) on the CV period distribution. If such fluctuations exist, they could conceivably alter the observable distribution dramatically. For example, it seems likely that the low state of any such cycles is essentially a detached phase, during which CVs are unrecognizable as such (see Section 4). Thus the observed period distribution of CVs undergoing such cycles would be that of systems caught in the high state. This distribution would therefore depend on the duty cycle of the fluctuations, i.e. the percentage of time actually spent in the high state. If this is a strong function of P_{orb} , the period distribution will be significantly modified. It is also possible that mass-transfer rate fluctuations could operate only within a certain range of donor masses (and hence orbital periods). This, too, would leave an imprint in the observed period distribution, as systems not undergoing such cycles would appear to be overabundant.

It is interesting to note here that studies of irradiation-driven mass-transfer cycles show that long-period CVs are much more susceptible to the instability producing such cycles than short-period CVs (see Section 4.2.1). Similarly, long-period CVs might be more likely to undergo nova-induced hibernation, since FAML may be less efficient in these systems (Livio et al. 1991). If mass-transfer-rate fluctuations exist, but are limited to long-

period CVs, they would tend to *reduce* the observed ratio of long-period to short-period pre-bounce systems. This would exacerbate the discrepancy with the standard model, as the observed ratio is actually too *high*. Thus mass-transfer-rate fluctuations are unlikely to be a panacea for the ailments afflicting the standard model.

8. DISCUSSION

The main result of our study is that the observed CV donor mass-radius relation seems to demand a modest, but significant revision of the standard model for CV evolution. More specifically, we have found that AML rates derived from donors below the period gap are $\simeq 2.5$ times higher than expected for pure GR driving, and that donor-based AML rates above the gap are $\simeq 1.5$ times smaller than in the standard RVJ $\gamma = 3$ model for MB. Allowing for these modifications produces a much improved match to the donor mass-radius data, predicts a minimum period in agreement with observations and might explain why long-period CVs are much more abundant in observed CV samples than expected in the standard model. These are nice returns for a relatively small price.

In this section, we will try to tie up a few remaining loose ends. First, we will discuss our results in the light of two recent studies that have come to rather different conclusions regarding CV evolution. Next, we will explore the sensitivity of our results to the assumed offset in radius between “standard” stellar models and observations of non-interacting stars, which may be due to magnetic activity and rapid rotation (see Section 5.2.1). This is arguably the main area of uncertainty in our method. We will then briefly consider other limitations and biases of our approach, and finally discuss whether enhanced AML below the gap is *physically* plausible.

8.1. A Comparison to Littlefair et al. (2008)

L08 carried out detailed eclipse analyses for a set of eight short-period CVs. Interestingly, they found that the donors in their sample were inflated by $\simeq 10\%$ relative to equal-mass MS stars. This agrees with our results (and L08’s measurements are, in fact, included in our mass-radius data base). However, L08 also estimated the effective temperatures of the accreting WDs in their CV sample and calculated the corresponding long-term accretion rates (see Section 6.4; Townsley & Bildsten 2002, 2003, 2004). They argue that these are broadly consistent with purely GR-driven AML losses, but not with substantially higher AML loss rates.

A comparison of the WD temperatures predicted by our model sequences to the observational data has already been presented in Figure 16 and briefly discussed in Section 6.4. Here, we therefore focus only on the subset of data points included in L08. These points are shown in green in Figure 16, and those systems with sub-stellar donors are additionally marked by open diamonds. At first glance, our revised model would seem to provide quite a good match to this subset of the data; if anything, it slightly underpredicts the effective temperatures of the three longest-period systems. By contrast, the standard model does not seem to match any of the data points.

However, this comparison is quite sensitive to the mismatch between the WD mass assumed in our models

($M_1 = 0.75 M_\odot$) and the typical WD mass in the L08 sample (the unweighted mean and dispersion is $\langle M_1 \rangle = 0.87 \pm 0.06 M_\odot$). Thus, for a fairer comparison, the model curves would need to be shifted upwards by slightly less than half the error bar shown in the top left corner of the plot. This would clearly improve the match to the standard model considerably, in line with the findings of L08.

Would such a shift also destroy the agreement between the revised model and the data? Based on Figure 16, we don't think so. In fact, an upward shift would bring the three longest-period objects in the sample into *better* agreement with the model, yet would still likely provide an adequate match to the shorter-period objects as well. Why then did L08 find that enhanced angular momentum loss models cannot work? Inspection of their Figure 5 suggests that the culprit is the particular *type* of model they chose to test. Their enhanced-AML model of choice invokes CAML via a circumbinary disk (Taam & Spruit 2001; Dubus et al. 2002; Taam et al. 2003; Willems et al. 2005). This happens to produce an almost constant, and rather high, \dot{M}_2 for systems that have evolved beyond P_{min} . This is indeed inconsistent with the data. However, in our scaled-GR model, \dot{M}_2 drops sharply in systems evolving through the minimum period (see Figure 11), producing a wide range of low mass-transfer rates in CVs with periods close to P_{min} . The systems argued by L08 to be inconsistent with enhanced-AML are all located in this P_{orb} regime. Even allowing for the expected offset due to the assumed WD mass, our revised model is likely to cover the observed accretion rates fairly well. We therefore do not think that there is a conflict between L08's data and our revised model, even without invoking the possibility that WD-based temperatures may not faithfully track the secular mass-transfer rates (Sections 4 and 6.4).

8.2. A Comparison to Sirotkin & Kim (2010)

A second recent study of the evolution of short-period CVs has been carried out by Sirotkin & Kim (2010, hereafter SK10). Like us, they attempt to infer $\dot{M}_2(P_{orb})$ from the observed donor mass-radius relation. More specifically, they adopt the broken-power-law approximation to the $\dot{M}_2 - R_2$ relationship from K06 and use a simplified analytical description of the donor response to mass loss to infer the corresponding mass-loss rate. Their results contrast with ours in two ways. First, they find considerably higher mass-loss rates than we do at essentially all orbital periods (compare their Figure 5 to our Figure 11). Second, despite this, SK10 argue that their inferred mass-loss rates are consistent with purely GR-driven AML.

There are quite a few important differences between our donor-based reconstruction of the $\dot{M}_2(P_{orb})$ relation and theirs. For example, since the period spike had not yet been discovered at the time, the value for P_{min} adopted in the K06 $\dot{M}_2 - R_2$ relationship is probably incorrect. Moreover, the broken-power-law approximation itself is, of course, only that – an approximation. In reality, ζ presumably varies smoothly along the CV evolution track (see e.g. Figure 10). Also, the impact of mass-loss history on the donor radii (see Section 2.2.2) is ignored in SK10's treatment. Last, but not least, where we use

state-of-the-art stellar models to describe the donor response to mass loss, SK10 use a simplified analytical description of the donor. The latter is definitely useful qualitatively, and helps to develop intuition, but it is not obvious to us whether (or to what degree) it is quantitatively reliable. It should be acknowledged, however, that their method did succeed in reproducing the $\dot{M}_2(P_{orb})$ relationship along a self-consistent donor sequence calculated by Kolb & Baraffe (1999) to within $\simeq 30\% - 40\%$, by using the numerical $\dot{M}_2 - R_2$ relationship along this sequence as input.

However, in spite of all these technical differences, we suspect that the main reason for the higher mass-transfer rates inferred by SK10 is that they did not correct for either tidal/rotational deformation (Section 5.2.2) or for other non-ML-related donor bloating (Section 5.2.1). As we have seen, the former amounts to $\simeq 4.5\%$ for short-period CVs, the latter to $\simeq 1.5\%$. The combined $\simeq 6\%$ non-ML-related bloating is a non-negligible fraction of the total observed donor inflation below the period gap. Figure 21 – which is discussed in more detail below – suggests that this may be expected to produce a factor of $\simeq 2$ difference in the inferred mass-transfer rates. This probably accounts for much of the difference between our inferred \dot{M}_2 estimates and theirs.

What is more puzzling to us is SK10's finding that their very high inferred mass-transfer rates are consistent with purely GR-driven AML. As far as we know, no other recent study of CV evolution has predicted such high rates for pure GR-driven evolution (e.g. Kolb 1993; Howell et al. 1997; Kolb & Baraffe 1999; Howell et al. 2001; Podsiadlowski et al. 2003). For example, at $P_{orb} \simeq 2$ hrs, the mass-transfer rates inferred by SK10 are about 4-5 times higher than those on a corresponding purely GR-driven evolution track calculated with our donor models (here we have made none of the corrections discussed in Section 5.2, to ensure the comparison with SK10 is fair).

We can also turn this argument around. If we adopt the broken-power-law mass-radius relationship of K06 – which is also the basis of SK10's method – and then use Equation 1 with $\dot{J}_{sys} = \dot{J}_{GR}$, as given in Equation 9, we obtain an estimate of $\dot{M}_{GR} \simeq 4 - 5 \times 10^{-11} M_\odot \text{yr}^{-1}$ near $P_{orb} \simeq 2$ hrs. This is again 4-5 times smaller than the mass-transfer rates estimated by SK10 in this regime. We thus do not understand how the mass-transfer rates estimated by SK10 can be consistent with pure GR driving.

8.3. Sensitivity to Non-Mass-Loss-Related Donor Bloating

How sensitive are our results to the particular non-ML-related bloating we have assumed? This question is explored quantitatively in Figure 21, where we plot the best-fit estimates of f_{GR} and f_{MB} as a function of the assumed non-ML-related donor bloating factor. Note that this factor is *in addition* to the bloating factor associated with tidal and rotational deformation, since the latter is relatively well understood and should always be applied.

Figure 21 shows that consistency with the standard model would require non-ML-related bloating at a level

²⁹ However, see the discussion of the discrepant results by Landin et al. (2009) in Section 5.2.2.

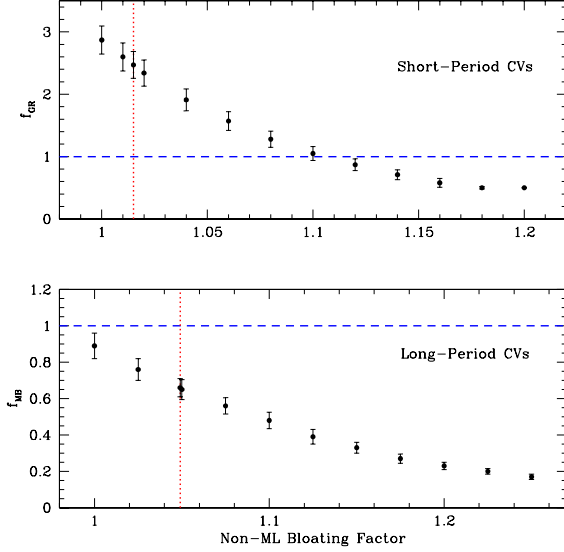


Figure 21. The sensitivity of the inferred angular-momentum-loss rates to the assumed amount of non-mass-loss-related donor bloating (in addition to that produced by tidal and rotational deformation; see Section 5.2.2). *Top panel:* The best-fit angular-momentum loss-rate amongst short-period CVs, f_{GR} , expressed as a multiple of the purely GR-driven rate, is shown as a function of the assumed bloating factor. The blue horizontal dashed line marks the standard model assumption – $f_{GR} = 1$ – and requires $\simeq 10\%$ bloating. Our actual best estimate of this bloating is 1.5%; this is marked by the red vertical dotted line and corresponds to our previously quoted estimate of $f_{GR} = 2.47 \pm 0.22$. *Bottom panel:* Same as top panel, but for long-period CVs, and with the relative angular-momentum-loss rate, f_{MB} , defined with reference to the standard RVJ recipe with $\gamma = 3$. Here, the standard model – $f_{MB} = 1$ – would require no bloating at all. Our best estimate of the bloating factor in this regime is 4.9%, which corresponds to our previously adopted $f_{MB} = 0.66 \pm 0.05$.

of $\simeq 10\%$ in fully convective donors below the gap and $\simeq 0\%$ in partially radiative donors above. The former number is higher than suggested by our analysis of the data in Figure 6, while the latter is lower. Thus *some* movement in the standard model parameters towards our revised model seems hard to avoid.

In our default models, we correct for a 1.5% (4.9%) radius offset between stellar models and actual stars in the fully convective (partially radiative) regime. As discussed in Section 5.2.1, the actual offset seen in Figure 6 is 4.5% (7.9%), but we follow Morales et al. (2010) in allowing for a $\simeq 3\%$ star-spot-induced bias in the observationally inferred radii. If we correct for the *full* offsets, we obtain $f_{GR} = 1.82 \pm 0.17$ and $f_{MB} = 0.55 \pm 0.05$. Figure 21 also confirms that the potential impact of irradiation-driven bloating ($\lesssim 1 - 2\%$ below the gap and $\lesssim 3\%$ above; see Section 5.2.3) is modest.

Overall then, we feel that the $M_2 - R_2$ data provides fairly strong evidence for a departure from the standard model, even allowing for the systematic biases and uncertainties associated with non-ML-induced donor inflation. In particular, it seems difficult to make purely GR-driven AML below the gap consistent with the data without pushing the systematics discussed above (and perhaps also those in Section 8.4 below) to their limits and in the same direction.

8.4. Other Biases and Limitations

We have already explored most of the assumptions and limitations of our method in exhaustive (exhausting?) detail, so here we will only consider a few additional issues that have not yet been covered elsewhere.

First, it is important to understand that the exact functional forms we have adopted for AML in our fully self-consistent models are necessarily arbitrary to some degree. By this we do not just mean that the detailed form is not perfectly constrained by the data, or that a wider exploration of models predicting different shapes for $\dot{M}_2(P_{orb})$ might have yielded an equally good or better fit to the data. (Both of these statements are true, however.) Rather, we mean that donor radii are sensitive only to the form and normalization of $\dot{M}(M_2)$, whereas physical AML recipes can depend on all binary parameters (M_1 , M_2 , R_2 , P_{orb} , a). In a semi-detached setting, these parameters are related by the period-density relation and Kepler’s third law. Thus we cannot expect to cleanly isolate the dependence of \dot{J}_{sys} on each individual parameter in this setting. The important point to remember is that *all AML recipes that produce similar runs of $\dot{M}_2(M_2)$ will produce virtually identical donor mass-radius relationships*.

Second, we have adopted a unique WD mass of $M_1 = 0.75 M_\odot$ in all of our modelling. If this turns out not to be representative, our results will necessarily be biased. Moreover, the sample of CVs for which we have donor masses and radii does, of course, include systems with a range of WD masses. Thus fitting a single model to all these data is not really quite self-consistent.

Fortunately, neither of these issues is too serious. At fixed M_2 , the mass-transfer rate depends on M_1 roughly as $\dot{M}_{2,GR} \propto M_1^{0.6-0.7}$ and $\dot{M}_{2,RVJ} \propto M_1^{-(0.9-1.7)}$ in our scaled-GR and scaled-RVJ models, respectively. As discussed in K06, the dispersion in observed WD masses in CVs is roughly 20%. At fixed M_2 , this therefore corresponds to an expected dispersion in the mass-loss rates of about 10% - 15% below the gap and 15% - 35% above. The effect of WD mass on the minimum period is also weak. Paczynski & Sienkiewicz (1983) show that this P_{min} scales approximately as $P_{min} \propto (M_1 + M_2)^{0.1}$. Thus an upward shift in the mean WD mass from $0.75 M_\odot$ to $0.80 M_\odot$, for example (c.f. last paragraph of Section 3), would only move P_{min} by $\simeq 0.5$ min. Nevertheless, the $\simeq 20\%$ dispersion in observed WD masses (P05, K06) is large enough to smear the period spike by $\simeq 3.2$ min (FWHM). For comparison, the *actual* FWHM of the period spike in the SDSS sample has been estimated to be 5.7 ± 1.7 min (G09). Thus WD mass dispersion alone is likely to account for at least a significant fraction of the observed spike width.³⁰

Third, we have assumed throughout that CV donors start their life as semi-detached stars on the zero-age MS (ZAMS). This may seem like a poor approximation, but Podsiadlowski et al. (2003) have shown that significantly evolved donors (with central Hydrogen fractions

³⁰ The quoted dispersion in WD masses corresponds to the *standard deviation* (σ) of the observed mass distribution. In order to estimate the FWHM of the corresponding shift in P_{min} we have used the conversion $\text{FWHM} = 2.3548\sigma$, which is appropriate for a Gaussian distribution.

of $X_c < 0.4$) only begin to dominate the CV population above periods of $\simeq 5$ hrs. This is in line with the CV birthrate distributions calculated by de Kool (1992) and Politano (1996), which show that long-period CVs typically have ages $\lesssim 1$ Gyr at the onset of mass-transfer. Even for a solar-mass secondary, this amounts to only $\simeq 10\%$ of its MS life time. CVs born in or below the gap can be considerably older, but at the relevant masses ($\lesssim 0.35 M_\odot$), even the age of the Galactic disk is only a fraction of the MS life time. Once mass transfer starts, the secondary's state of nuclear evolution is essentially frozen. Thus the assumption that the CV population below 5 hrs is dominated by unevolved systems with initially ZAMS donors should be quite good.

However, there might be one interesting exception to this statement. CV born within the last $\simeq 5$ Gyr with donors in the mass range $0.25 M_\odot \lesssim M_2 \lesssim 0.35 M_\odot$ – *i.e. most of the CVs born inside the period gap*. The BCAH98 models suggest that the secondary stars in such systems will be slightly, but significantly, inflated relative to their ZAMS radius (by $\simeq 1\% - 4\%$). The calculations by Politano (1996) and de Kool (1992) suggest that such systems might contribute $\simeq 20\% - 30\%$ to the present-day CV population.

8.5. Is Enhanced AML below the Gap Plausible?

As noted in Section 2.3.1, the assumption that MB stops when the donor loses its radiative core was originally rooted in the idea that the magnetic fields in low-mass stars are generated by dynamo action in the tachocline (the boundary between the radiative core and the overlying convection zone; e.g. MacGregor & Charbonneau 1997; Charbonneau & MacGregor 1997). If so, then stars without a radiative core – which do not possess a tachocline – would be incapable of generating significant magnetic fields. Consequently, there would be no magnetically channelled stellar winds in fully convective stars, and no magnetic braking.

At some level, we have known for a long time that these arguments cannot be entirely correct. After all, fully convective stars do display all aspects of stellar activity, from variability to emission line, ultraviolet, X-ray and radio emission (e.g. Giampapa & Liebert 1986; Stern et al. 1994; Linsky et al. 1995; Hodgkin et al. 1995; Fleming et al. 1995; Delfosse et al. 1998). Thus there is little question that fully convective stars are capable of generating significant magnetic fields. Given only this information, one might begin to wonder if there is any change in the magnetic field across the fully convective boundary at all.

Thankfully, there is at least some observational support for this key idea. Broadly speaking, there is evidence for systematic changes in both magnetic field strength and topology with spectral type (e.g. Reiners & Basri 2008, 2009, 2010; Donati et al. 2008; Morin et al. 2010). It is tempting to interpret these changes as signalling a switch from an interface dynamo anchored in the tachocline of partially radiative stars to a turbulent dynamo in fully convective ones. It should be noted, however, that the existing data already point to considerably more complex behaviour than a simple switch.

From the point of view of CV evolution, the big question is, of course, whether and how *magnetic braking* changes across the fully convective boundary. There is

certainly *some* evidence for this as well (see, for example, Figs. 9 and 10 in Reiners & Basri 2008). A particularly nice series of studies in this context is that by Barnes (2003, 2007). He showed that data on stellar rotation in open clusters showed evidence for two distinct spin-down sequences: the so-called I-sequence (“I” for interface) and the so-called C-sequence (“C” for convective). Partially radiative stars are born on the C-sequence, but then evolve onto the I-sequence, where they spin down according to a standard Skumanich-type law, with $\dot{J} \propto \Omega^3$. Fully convective stars remain on the C-sequence throughout their lives. Spin-down on the C-sequence is slower than on the I-sequence, but still significant.

This semi-empirical picture suggests an obvious application to CVs. Above the period gap, donors have (mostly? – see discussion in Section 7.2) joined the I-sequences and are being braked by a standard Skumanich-type MB law. This is consistent with our finding that this type of braking law provides a good fit to the mass-radius data for long-period CVs. As CVs approach the gap, the donors undergo a switch from an interface dynamo to a turbulent one, before ultimately joining the C-sequence. Since MB is weaker on the C-sequence, this amounts to a disruption of AML and produces the period gap. The transition from the I-sequence to the C-sequences may not be instantaneous – the opposite transition in isolated stars apparently takes a few $\times 10^8$ yrs (Barnes 2003). The transition may therefore not be entirely uneventful, and this might have something to do with the huge spread in WD-based accretion rates in the 3 hr - 4 hr period range (which is also the location where the peculiar SW Sex stars are preferentially located, e.g. Rodríguez-Gil et al. 2007). The scenario sketched above is similar, though not identical, to the double-dynamo model proposed over a decade ago by Zangrilli et al. (1997).

In any case, it remains to be seen whether the braking rates predicted for the I- and C-sequences by Barnes (2003, 2007) and Barnes & Kim (2010) are quantitatively consistent with the AML rates we have inferred for long- and short-period CVs, respectively. So far, we have only carried out some very preliminary investigations along these lines, which have not been too promising. However, we plan to carry out more detailed tests in the near future.

9. SUMMARY

We have used state-of-the-art stellar models to reconstruct the evolutionary track followed by cataclysmic variables from the observed properties of their donor stars. Along the way, we have updated the semi-empirical donor sequence of K06 and also reviewed the close connection between the evolution of CVs and the properties of their secondaries. Our main results and conclusions are as follows.

1. Mass transfer in CVs is thought to be driven by systemic angular momentum losses, on a time scale, τ_{ev} , that is comparable to the thermal time scale of the secondary star. As a result, the donor is driven slightly out of thermal equilibrium and has a larger radius than an isolated star of equal mass. The degree of donor inflation increases with increasing

- \dot{M}_2 and can therefore be used as a tracer of the secular mass-transfer rate.
2. We provide an update of the semi-empirical donor sequence presented in K06, in which the donor mass-radius relationship is approximated as a broken power law (Figure 4 and Table 2. The update is necessary mainly to include some new observational data and to take into account the recent discovery of the period spike (G09). The original and updated sequences both confirm that CV donors are indeed larger than equal-mass MS stars. This is true both above and below the period gap. The gap itself corresponds to a discontinuity in the mass-radius relation, which is in line with the idea that the period gap is produced by a sudden reduction in the prevailing angular-momentum-loss rate.
 3. The angular-momentum-loss rates predicted by a variety of commonly used magnetic braking recipes differ enormously, both in magnitude and the form of their dependence on binary parameters (Figure 2). These differences are not only found between “classic” and “saturated” recipes, but even between conceptually similar ones. A more reliable description of magnetic braking is therefore desperately needed to improve our understanding of binary evolution, in general, and CV evolution, specifically.
 4. The time scale on which the donor adjusts its radius to the prevailing mass-loss rate, τ_{adj} , is $\simeq 5\%$ of its equilibrium thermal time scale. So long as τ_{adj} is very short compared to τ_{ev} , the donor radius traces the “instantaneous” mass-loss rate (averaged over the last few τ_{adj}). However, τ_{ev} becomes comparable to τ_{adj} at critical times in a CV’s evolution (e.g. near the upper edge of the period gap and on passage through the minimum period). Thus, in practice, donor radii do retain some sensitivity to their previous secular mass loss history (Figure 1).
 5. If CVs undergo long-term mass-transfer-rate fluctuations, these are likely to take place on time scales of $\tau_{var} \sim 10^4 - 10^9$ yrs (Figure 5). Such fluctuations would confound most attempts to estimate the secular mass-transfer rates in CVs. In particular, even the thermal time scale of the accreted layer on the WD primary is far shorter than τ_{var} . Thus the quiescent effective temperatures of WDs in CVs would track these variations, albeit with reduced amplitude.
 6. Mass-transfer-rate estimates derived from the mass-loss-induced bloating of the donor stars in CVs are reasonably likely to be valid even in the presence of such fluctuations. This is partly because the radius adjustment time scale is long, and partly because the donor swelling due to irradiation – one of the possible drivers of mass-transfer cycles – is only expected to be $\sim 1\%$.
 7. Based on a new compilation of observational data for non-interacting low-mass stars, stellar models appear to underestimate the radii of fully convective stars by $4.5\% \pm 0.5\%$ and those of partially radiative stars by $7.9\% \pm 1.2\%$ (Figure 6). Moreover, there is no compelling evidence for significant intrinsic scatter in the observed radii for fully convective stars, whereas a significant 5% dispersion is seen among partially radiative stars. Approximately 3% of the discrepancy between models and observations is likely to be an artefact of the eclipse modelling from which most observational radii are derived. The remaining offsets are probably due to star spots and/or a reduction in convective efficiency associated with fast rotation or magnetic fields.
 8. Tidal and rotational distortions cause Roche-lobe-filling stars to be larger than isolated, spherical stars, even in the absence of mass loss (Figure 7). The size of this effect depends on the effective polytropic index of the star (and hence on the stellar mass) and also weakly on mass ratio. Below the period gap, the bloating associated with tidal and rotational distortions is $\simeq 4.5\%$; above the gap, it reaches $\simeq 6.8\%$ at $P_{orb} \simeq 5.6$ hrs ($M_2 = 0.6M_\odot$).
 9. Irradiation can also lead to non-ML-related swelling of the donor star, but the size of this effect is expected to be relative modest in CVs: $< 1 - 2\%$ below the period gap and $< 3\%$ above (Figure 8; see also discussion in Section 5.2.3).
 10. Taking the corrections described in points (7) and (8) above into account, we model the observed donor mass-radius relationship (as presented in P05 and K06) using self-consistent, state-of-the-art models of mass-losing stars. For simplicity, we assume that the mass transfer in our models is driven by two simple AML recipes: a scaled version of the standard gravitational radiation loss rate below the gap, and a scaled version of the Rappaport et al. (1983) MB law with $\gamma = 3$ above the gap. With suitable normalization parameters, f_{GR} and f_{MB} , these recipes provide acceptable matches to the observed data and make it easy to assess the evidence for deviations from the standard model of CV evolution, in which $f_{GR} = f_{MB} = 1$. The best fit to the mass-radius data is obtained for $f_{GR} = 2.47 \pm 0.22$ (below that gap) and $f_{MB} = 0.66 \pm 0.05$ (above the gap), where the quoted uncertainties are purely statistical. This revised model matches the observations significantly better than the standard model (Figure 9).
 11. Our revised model predicts a location for the minimum period that is in excellent agreement with the observed location of the period spike, $P_{min} \simeq 82$ min (Figure 14). Even allowing for donor bloating unrelated to mass loss – see points (7) and (8) above – the standard model predicts a significantly shorter P_{min} . The revised model also predicts the correct location for the upper edge of the period gap, $P_{gap,+}$, while the standard model predicts a significantly longer value. Both standard and revised models are consistent with the observed location of the lower gap edge, $P_{gap,-}$, since this is primarily determined by the equilibrium properties of main sequence stars.

12. Both standard and revised models predict donor spectral types that are in good agreement with observations (Figure 15). The same is true for both the original and updated broken-power-law donor sequences. Ordinary main sequence stars would predict significantly earlier spectral types at fixed orbital period.
13. We have used the method of Townsley & Bildsten (2003, 2004) to predict the effective temperatures of the accreting WD along both standard and revised evolution tracks. A naive comparison to the observed data compiled by TG09 (Figure 16) suggests that, if anything, an even higher value of f_{GR} than adopted in our revised model would provide a better fit to the data. However, there are several possible biases and problems that may make such a comparison unreliable. In particular, the predicted effective temperatures are quite sensitive to the assumed WD mass. The issue noted in point (5) above may also be a concern, particularly above the period gap.
14. The predicted near-infrared absolute magnitudes of CV donors generally trace the lower envelope of observed absolute magnitudes for systems with well-determined parallax distances (Figure 17). This is true for all the sequences we consider (standard, revised and broken power law). Any of these sequences can therefore be used to set a firm lower limit on the distance to a CV, given only a single-epoch measurement of its apparent magnitude in the near-IR. However, the offset between the predicted and observed magnitudes indicates that the donors only contribute $\simeq 20\% - 30\%$ to the total near-IR flux of CVs. Distance *estimates* (as opposed to lower limits) obtained by correcting for this offset are uncertain by at least a factor of $\simeq 2$.
15. We have carried out a comparison of the mass-transfer rates along the standard and revised model sequences to the critical rate for the thermal disk instability that is thought to be responsible for dwarf nova eruptions (Figure 19). Below the gap, both models predict mass-transfer rates well below the critical rate and thus firmly in the unstable regime. This is consistent with the observations that nearly all CVs below the period gap are dwarf novae. However, above the period gap, the mass-transfer rates predicted by both sequences decline faster with orbital period than the critical rate. The curves cross near $\simeq 5$ hrs in both cases, thus naively predicting that stable nova-like CVs should only become the dominant CV population at periods longer than this. By contrast, observations show that the dwarf-nova fraction reaches a minimum at the upper edge of the period gap and then gradually *rises* towards longer periods (Figure 18). The origin and severity of this discrepancy are not clear at this point. Long-term mass-transfer cycles offer one possible explanation.
16. Based on *highly approximate* predicted orbital period distributions for the standard and revised sequences, we show that the revised model predicts roughly $3\times$ more long-period CVs, relative to short-period, pre-bounce CVs (Figure 20 and Table 10). This may be enough to resolve a long-standing discrepancy between the standard model and observations (Pretorius et al. 2007a; Pretorius & Knigge 2008a,b). The faster evolution below the gap in the revised model also predicts that a higher fraction of CVs should be “period bouncers”, i.e. systems that have already evolved beyond the minimum period. For an assumed space density of $\rho \simeq 2 \times 10^{-5} \text{ pc}^{-3}$, the predicted numbers of (especially long-period) CVs within 100 pc are in good agreement with observations. Much higher space densities would predict too many very bright and nearby CVs.
17. We draw attention to a peculiar feature in the period distribution at the lower edge of the period gap (Figure 20). The re-establishment of mass transfer causes CVs to execute a loop (the so-called “period flag”) in the $P_{orb} - \dot{M}_2$ plane at this point. Since $\dot{P}_{orb} = 0$ during the evolution across the flag, one might expect a local maximum in the predicted period distribution at this point. It can be shown that the visibility of this local maximum increases with increasing \dot{M}_2 below the gap. In the standard model, this local maximum is not visible in the predicted period distribution, but in the revised model, it might be. As yet, there is no observational evidence for an accumulation of systems near the lower edge of the gap, although none of the existing CV samples are really suitable for testing this prediction.
18. Our result that $f_{GR} > 1$ contrasts with the study by L08, who have argued that enhanced angular momentum loss below the gap is inconsistent with the WD temperatures in their sample of eclipsing CVs. However, their findings appear to be applicable only to the particular *type* of enhanced angular momentum loss they assumed (CAML associated with a circumbinary disk). This predicts relatively constant and high \dot{M}_2 for period bouncers, whereas \dot{M}_2 drops off steeply in this regime in our simple scaled-GR model. Based on a direct comparison (Figure 16), our revised model does not seem to be in conflict with the data presented in L08.
19. An independent attempt to infer $\dot{M}_2(P_{orb})$ for short-period CVs from the observed donor mass-radius relation has recently been carried out by SK10. They estimate higher mass-transfer rates than we do (compare their Figure 5 to our Figure 11), but argue that these rates are nevertheless compatible with purely GR-driven angular momentum losses. There are numerous technical differences between their approach and ours, but we believe the main reason for the differences between the inferred mass-transfer rates is that SK10 did not correct for donor bloating unrelated to mass loss (points (7) and (8) above). However, we do not understand how the very high rates they infer could be driven by GR alone.

20. We consider the physical plausibility that fully convective donors below the period gap should experience residual magnetic braking. Observations of non-interacting stars certainly prove that they are capable of generating substantial magnetic fields. Whether they can also produce MB strong enough to be consistent with our revised model for CV evolution remains to be seen. Recent developments in the study of isolated low-mass stars may make it possible to test this hypothesis in the near future.
21. In order to facilitate the use of our results, we make all of the donor and evolution sequences we have constructed available in electronically readable form. More specifically, our broken-power-law donor sequence provides all of the stellar and photometric properties describing CV secondary stars as a function of orbital period (Table 2). The full self-consistent CV evolution sequences – both standard and revised – provide the same, plus a complete set of all other binary parameters that are relevant to CV evolution (3-8).

We are extremely grateful to Jean-Marie Hameury for providing us with an extended version of Table 2 in Hameury & Ritter (1997), to Fedir Sirotkin for supplying the fit coefficients listed in Table 1, and to Boris Gänsicke for sharing with us some of the results described in G09 prior to their publication. We would also like to thank Juhan Frank, Boris Gänsicke, Natasha Ivanova, Woong-Tae Kim, Ulrich Kolb, Natalia Landin, Stuart Littlefair, Retha Pretorius, Hans Ritter, Alison Sills, Fedir Sirotkin, Dean Townsley and Brian Warner for helpful discussions and much-needed advice. We also gratefully acknowledge financial support via grants to JP from the National Science Foundation (AST-0908363) and the Mount Cuba Astronomical Foundation.

REFERENCES

- Andronov, N., Pinsonneault, M., & Sills, A. 2003, *ApJ*, 582, 358
- Araujo-Betancor, S., Gänsicke, B. T., Long, K. S., Beuermann, K., de Martino, D., Sion, E. M., & Szkody, P. 2005, *ApJ*, 622, 589
- Araujo-Betancor, S., et al. 2003, *ApJ*, 583, 437
- Baraffe, I., Chabrier, G., Allard, F., & Hauschildt, P. H. 1998, *A&A*, 337, 403
- . 2002, *A&A*, 382, 563
- Baraffe, I., Chabrier, G., Barman, T. S., Allard, F., & Hauschildt, P. H. 2003, *A&A*, 402, 701
- Baraffe, I., & Kolb, U. 2000, *MNRAS*, 318, 354
- Barker, J., & Kolb, U. 2003, *MNRAS*, 340, 623
- Barnes, S. A. 2003, *ApJ*, 586, 464
- . 2007, *ApJ*, 669, 1167
- . 2010, *ApJ*, 722, 222
- Barnes, S. A., & Kim, Y. 2010, *ApJ*, 721, 675
- Basri, G. 2009, in *American Institute of Physics Conference Series*, Vol. 1094, American Institute of Physics Conference Series, ed. E. Stempels, 206–215
- Beatty, T. G., et al. 2007, *ApJ*, 663, 573
- Becker, A. C., et al. 2008, *MNRAS*, 386, 416
- Berger, E., et al. 2009, *ApJ*, 695, 310
- Bessell, M. S. 1990, *PASP*, 102, 1181
- Beuermann, K. 2006, *A&A*, 460, 783
- Beuermann, K., Baraffe, I., & Hauschildt, P. 1999, *A&A*, 348, 524
- Beuermann, K., Baraffe, I., Kolb, U., & Weichhold, M. 1998, *A&A*, 339, 518
- Beuermann, K., & Reinsch, K. 2008, *A&A*, 480, 199
- Beuermann, K., Stasiewski, U., & Schwöpe, A. D. 1992, *A&A*, 256, 433
- Bitner, M. A., Robinson, E. L., & Behr, B. B. 2007, *ApJ*, 662, 564
- Blake, C. H., Torres, G., Bloom, J. S., & Gaudi, B. S. 2008, *ApJ*, 684, 635
- Buat-Ménard, V., Hameury, J., & Lasota, J. 2001, *A&A*, 369, 925
- Büning, A., & Ritter, H. 2004, *A&A*, 423, 281
- Çakırlı, Ö., İbanoğlu, C., & Güngör, C. 2009, *New Astronomy*, 14, 496
- Cannizzo, J. K., & Pudritz, R. E. 1988, *ApJ*, 327, 840
- Chabrier, G., & Baraffe, I. 1997, *A&A*, 327, 1039
- . 2000, *ARA&A*, 38, 337
- Chabrier, G., Baraffe, I., Allard, F., & Hauschildt, P. 2000, *ApJ*, 542, 464
- Chabrier, G., Baraffe, I., Leconte, J., Gallardo, J., & Barman, T. 2009, in *American Institute of Physics Conference Series*, Vol. 1094, American Institute of Physics Conference Series, ed. E. Stempels, 102–111
- Chabrier, G., Gallardo, J., & Baraffe, I. 2007, *A&A*, 472, L17
- Charbonneau, P., & MacGregor, K. B. 1997, *ApJ*, 486, 502
- de Kool, M. 1992, *A&A*, 261, 188
- Delfosse, X., Forveille, T., Perrier, C., & Mayor, M. 1998, *A&A*, 331, 581
- Demory, B., et al. 2009, *A&A*, 505, 205
- Devor, J., et al. 2008, *ApJ*, 687, 1253
- Donati, J., & Landstreet, J. D. 2009, *ARA&A*, 47, 333
- Donati, J., et al. 2008, *MNRAS*, 390, 545
- Dubus, G., Taam, R. E., & Spruit, H. C. 2002, *ApJ*, 569, 395
- Duerbeck, H. W. 1992, in *Astronomical Society of the Pacific Conference Series*, Vol. 29, Cataclysmic Variable Stars, ed. N. Vogt, 379–
- Eggleton, P. P. 1983, *ApJ*, 268, 368
- Elias, J. H., Frogel, J. A., Matthews, K., & Neugebauer, G. 1982a, *AJ*, 87, 1893
- . 1982b, *AJ*, 87, 1029
- Fleming, T. A., Schmitt, J. H. M. M., & Giampapa, M. S. 1995, *ApJ*, 450, 401
- Gänsicke, B. T., Sion, E. M., Beuermann, K., Fabian, D., Cheng, F. H., & Krautter, J. 1999, *A&A*, 347, 178
- Gänsicke, B. T., et al. 2009, *MNRAS*, 397, 2170
- Giampapa, M. S., & Liebert, J. 1986, *ApJ*, 305, 784
- Hameury, J., Menou, K., Dubus, G., Lasota, J., & Hure, J. 1998, *MNRAS*, 298, 1048
- Hameury, J., & Ritter, H. 1997, *A&AS*, 123, 273
- Hameury, J. M., King, A. R., & Lasota, J. P. 1989, *MNRAS*, 237, 39
- Hameury, J. M., King, A. R., Lasota, J. P., & Ritter, H. 1988, *MNRAS*, 231, 535
- Harrison, T. E., McNamara, B. J., Szkody, P., & Gilliland, R. L. 2000, *AJ*, 120, 2649
- Harrop-Allin, M. K., & Warner, B. 1996, *MNRAS*, 279, 219
- Hartman, J. D., Bakos, G. Á., Noyes, R. W., Sipőcz, B., Kovács, G., Mazeh, T., Shporer, A., & Pál, A. 2009, *ArXiv e-prints*
- Hauschildt, P. H., Allard, F., & Baron, E. 1999, *ApJ*, 512, 377
- Hessman, F. V., Gänsicke, B. T., & Mattei, J. A. 2000, *A&A*, 361, 952
- Hodgkin, S. T., Jameson, R. F., & Steele, I. A. 1995, *MNRAS*, 274, 869
- Holberg, J. B., & Bergeron, P. 2006, *AJ*, 132, 1221
- Howell, S. B., Ciardi, D. R., Dhillon, V. S., & Skidmore, W. 2000, *ApJ*, 530, 904
- Howell, S. B., Gänsicke, B. T., Szkody, P., & Sion, E. M. 2002, *ApJ*, 575, 419
- Howell, S. B., Nelson, L. A., & Rappaport, S. 2001, *ApJ*, 550, 897
- Howell, S. B., Rappaport, S., & Politano, M. 1997, *MNRAS*, 287, 929
- Huélamo, N., et al. 2009, *A&A*, 503, 873
- Hussain, G. A. J. 2004, *Astronomische Nachrichten*, 325, 216
- Irwin, J., Hodgkin, S., Aigrain, S., Hebb, L., Bouvier, J., Clarke, C., Moraux, E., & Bramich, D. M. 2007, *MNRAS*, 377, 741
- Ivanova, N., & Kalogera, V. 2006, *ApJ*, 636, 985
- Ivanova, N., & Taam, R. E. 2003, *ApJ*, 599, 516
- Kafka, S., & Honeycutt, R. K. 2005, *AJ*, 130, 742
- Kawaler, S. D. 1988, *ApJ*, 333, 236
- Keppens, R., MacGregor, K. B., & Charbonneau, P. 1995, *A&A*, 294, 469
- King, A. R. 2000, *New Astronomy Reviews*, 44, 167
- King, A. R., & Cannizzo, J. K. 1998, *ApJ*, 499, 348
- King, A. R., Frank, J., Kolb, U., & Ritter, H. 1995, *ApJ*, 444, L37
- . 1996, *ApJ*, 467, 761
- King, A. R., & Kolb, U. 1995, *ApJ*, 439, 330
- King, A. R., & Schenker, K. 2002, in *Astronomical Society of the Pacific Conference Series*, Vol. 261, The Physics of Cataclysmic Variables and Related Objects, ed. B. T. Gänsicke, K. Beuermann, & K. Reinsch, 233–
- Kippenhahn, R., & Thomas, H. 1970, in *IAU Colloq. 4: Stellar Rotation*, ed. A. Slettebak, 20–
- Knigge, C. 2006, *MNRAS*, 373, 484

- Knigge, C., Long, K. S., Hoard, D. W., Szkody, P., & Dhillon, V. S. 2000, *ApJ*, 539, L49
- Kolb, U. 1993, *A&A*, 271, L49
- Kolb, U., & Baraffe, I. 1999, *MNRAS*, 309, 1034
- . 2000, *New Astronomy Reviews*, 44, 99
- Kolb, U., King, A. R., & Baraffe, I. 2001a, *MNRAS*, 321, 544
- Kolb, U., Rappaport, S., Schenker, K., & Howell, S. 2001b, *ApJ*, 563, 958
- Kolb, U., & Ritter, H. 1992, *A&A*, 254, 213
- Lai, D., Rasio, F. A., & Shapiro, S. L. 1994, *ApJ*, 423, 344
- Landin, N. R., Mendes, L. T. S., & Vaz, L. P. R. 2009, *A&A*, 494, 209
- Lasota, J. 2001, *New Astronomy Reviews*, 45, 449
- Li, J. 1999, *MNRAS*, 302, 203
- Linnell, A. P., Godon, P., Hubeny, I., Sion, E. M., & Szkody, P. 2007, *ApJ*, 662, 1204
- . 2010, *ApJ*, 719, 271
- Linnell, A. P., Godon, P., Hubeny, I., Sion, E. M., Szkody, P., & Barrett, P. E. 2009, *ApJ*, 703, 1839
- Linsky, J., & Saar, S. 1987, in *Lecture Notes in Physics*, Berlin Springer Verlag, Vol. 291, Cool Stars, Stellar Systems and the Sun, ed. J. L. Linsky & R. E. Stencel, 44–
- Linsky, J. L., Wood, B. E., Brown, A., Giampapa, M. S., & Ambruster, C. 1995, *ApJ*, 455, 670
- Littlefair, S. P., Dhillon, V. S., Marsh, T. R., Gänsicke, B. T., Baraffe, I., & Watson, C. A. 2007, *MNRAS*, 381, 827
- Littlefair, S. P., Dhillon, V. S., Marsh, T. R., Gänsicke, B. T., Southworth, J., Baraffe, I., Watson, C. A., & Copperwheat, C. 2008, *MNRAS*, 388, 1582
- Livio, M., Govarie, A., & Ritter, H. 1991, *A&A*, 246, 84
- Livio, M., & Pringle, J. E. 1994, *ApJ*, 427, 956
- Livio, M., & Shara, M. M. 1987, *ApJ*, 319, 819
- Long, K. S., Gänsicke, B. T., Knigge, C., Froning, C. S., & Monard, B. 2009, *ApJ*, 697, 1512
- López-Morales, M. 2007, *ApJ*, 660, 732
- López-Morales, M., Orosz, J. A., Shaw, J. S., Havelka, L., Arevalo, M. J., McIntyre, T., & Lazaro, C. 2006, *ArXiv Astrophysics e-prints*
- López-Morales, M., & Shaw, J. S. 2007, in *Astronomical Society of the Pacific Conference Series*, Vol. 362, The Seventh Pacific Rim Conference on Stellar Astrophysics, ed. Y. W. Kang, H.-W. Lee, K.-C. Leung, & K.-S. Cheng, 26–
- MacDonald, J. 1986, *ApJ*, 305, 251
- MacGregor, K. B., & Charbonneau, P. 1997, *ApJ*, 486, 484
- Martin, R. G., Livio, M., & Schaefer, B. E. 2010, *ArXiv e-prints*
- Maxted, P. F. L., Marsh, T. R., Morales-Rueda, L., Barstow, M. A., Dobbie, P. D., Schreiber, M. R., Dhillon, V. S., & Brinkworth, C. S. 2004, *MNRAS*, 355, 1143
- Maxted, P. F. L., O'Donoghue, D., Morales-Rueda, L., Napiwotzki, R., & Smalley, B. 2007, *MNRAS*, 376, 919
- McCormick, P., & Frank, J. 1998, *ApJ*, 500, 923
- McDermott, P. N., & Taam, R. E. 1989, *ApJ*, 342, 1019
- Mestel, L. 1968, *MNRAS*, 138, 359
- Mestel, L., & Spruit, H. C. 1987, *MNRAS*, 226, 57
- Morales, J. C., Gallardo, J., Ribas, I., Jordi, C., Baraffe, I., & Chabrier, G. 2010, *ApJ*, 718, 502
- Morales, J. C., Torres, G., Marschall, L. A., & Brehm, W. 2009a, *ApJ*, 707, 671
- Morales, J. C., et al. 2009b, *ApJ*, 691, 1400
- Morin, J., Donati, J., Petit, P., Delfosse, X., Forveille, T., & Jardine, M. M. 2010, *MNRAS*, 407, 2269
- Naylor, T., Charles, P. A., Mukai, K., & Evans, A. 1992, *MNRAS*, 258, 449
- O'Brien, M. S., Bond, H. E., & Sion, E. M. 2001, *ApJ*, 563, 971
- O'Donoghue, D., Koen, C., Kilkeny, D., Stobie, R. S., Koester, D., Bessell, M. S., Hambly, N., & MacGillivray, H. 2003, *MNRAS*, 345, 506
- Osaki, Y. 1996, *PASP*, 108, 39
- Osaki, Y., & Meyer, F. 2003, *A&A*, 401, 325
- . 2004, *A&A*, 428, L17
- Paczynski, B. 1967, *acta*, 17, 287
- . 1971, *ARA&A*, 9, 183
- Paczynski, B., & Sienkiewicz, R. 1983, *ApJ*, 268, 825
- Parsons, S. G., Marsh, T. R., Copperwheat, C. M., Dhillon, V. S., Littlefair, S. P., Gänsicke, B. T., & Hickman, R. 2010, *MNRAS*, 402, 2591
- Patterson, J. 1984, *ApJS*, 54, 443
- . 1998, *PASP*, 110, 1132
- . 2009, *ArXiv e-prints*
- Patterson, J., Thorstensen, J. R., & Knigge, C. 2008, *PASP*, 120, 510
- Patterson, J., et al. 2002, *PASP*, 114, 721
- . 2005, *PASP*, 117, 1204
- Perryman, M. A. C., et al. 1997, *A&A*, 323, L49
- Pizzolato, N., Maggio, A., Micela, G., Sciortino, S., & Ventura, P. 2003, *A&A*, 397, 147
- Podsiadlowski, P., Han, Z., & Rappaport, S. 2003, *MNRAS*, 340, 1214
- Politano, M. 1996, *ApJ*, 465, 338
- . 2004, *ApJ*, 604, 817
- Pretorius, M. L., & Knigge, C. 2008a, *MNRAS*, 385, 1471
- . 2008b, *MNRAS*, 385, 1485
- Pretorius, M. L., Knigge, C., & Kolb, U. 2007a, *MNRAS*, 374, 1495
- Pretorius, M. L., Knigge, C., O'Donoghue, D., Henry, J. P., Gioia, I. M., & Mullis, C. R. 2007b, *MNRAS*, 382, 1279
- Rappaport, S., Joss, P. C., & Webbink, R. F. 1982, *ApJ*, 254, 616
- Rappaport, S., Verbunt, F., & Joss, P. C. 1983, *ApJ*, 275, 713
- Reiners, A. 2009, in *IAU Symposium*, Vol. 259, IAU Symposium, 339–344
- Reiners, A., & Basri, G. 2008, *ApJ*, 684, 1390
- . 2009, *A&A*, 496, 787
- . 2010, *ApJ*, 710, 924
- Renvoizé, V., Baraffe, I., Kolb, U., & Ritter, H. 2002, *A&A*, 389, 485
- Ribas, I. 2006, *Ap&SS*, 304, 89
- Ritter, H. 1988, *A&A*, 202, 93
- Ritter, H., & Kolb, U. 1992, *A&A*, 259, 159
- . 2003, *A&A*, 404, 301
- Ritter, H., Zhang, Z., & Kolb, U. 1995, in *Astrophysics and Space Science Library*, Vol. 205, Cataclysmic Variables, ed. A. Bianchini, M. della Valle, & M. Orio, 479–
- Ritter, H., Zhang, Z., & Kolb, U. 1996, in *IAU Symposium*, Vol. 165, Compact Stars in Binaries, ed. J. van Paradijs, E. P. J. van den Heuvel, & E. Kuulkers, 65–71
- Ritter, H., Zhang, Z., & Kolb, U. 2000, *A&A*, 360, 969
- Rodríguez-Gil, P., et al. 2007, *MNRAS*, 377, 1747
- Schaefer, B. E., & Patterson, J. 1983, *ApJ*, 268, 710
- Schenker, K., Kolb, U., & Ritter, H. 1998, *MNRAS*, 297, 633
- Schmidtobreick, L., Tappert, C., Bianchini, A., & Mennickent, R. E. 2005, *A&A*, 432, 199
- Schreiber, M. R., & Gänsicke, B. T. 2002, *A&A*, 382, 124
- Schreiber, M. R., & Lasota, J. 2007, *A&A*, 473, 897
- Shafter, A. W. 1992, *ApJ*, 394, 268
- Shara, M. M. 1989, *PASP*, 101, 5
- Shara, M. M., Livio, M., Moffat, A. F. J., & Orio, M. 1986, *ApJ*, 311, 163
- Shkolnik, E., Liu, M. C., Reid, I. N., Hebb, L., Cameron, A. C., Torres, C. A., & Wilson, D. M. 2008, *ApJ*, 682, 1248
- Sills, A., Pinsonneault, M. H., & Terndrup, D. M. 2000, *ApJ*, 534, 335
- Sirotkin, F. V., & Kim, W. 2009, *ApJ*, 698, 715
- . 2010, *ApJ*, 721, 1356
- Skumanich, A. 1972, *ApJ*, 171, 565
- Smak, J. 2004a, *acta*, 54, 221
- . 2004b, *acta*, 54, 181
- . 2004c, *acta*, 54, 429
- Smith, M. A. 1979, *PASP*, 91, 737
- Somers, M. W., Mukai, K., & Naylor, T. 1996, *MNRAS*, 278, 845
- Spruit, H. C., & Ritter, H. 1983, *A&A*, 124, 267
- Stauffer, J. R., & Hartmann, L. W. 1987, *ApJ*, 318, 337
- Steehls, D. 2004, *Astronomische Nachrichten*, 325, 185
- Stehle, R., King, A., & Rudge, C. 2001, *MNRAS*, 323, 584
- Stehle, R., Kolb, U., & Ritter, H. 1997, *A&A*, 320, 136
- Stehle, R., Ritter, H., & Kolb, U. 1996, *MNRAS*, 279, 581
- Stern, R. A., Schmitt, J. H. M. M., Pye, J. P., Hodgkin, S. T., Stauffer, J. R., & Simon, T. 1994, *ApJ*, 427, 808
- Szkody, P., et al. 2002, *AJ*, 123, 430
- . 2003, *AJ*, 126, 1499
- . 2004, *AJ*, 128, 1882
- . 2005, *AJ*, 129, 2386
- . 2006, *AJ*, 131, 973
- . 2007, *AJ*, 134, 185
- . 2009, *AJ*, 137, 4011
- Taam, R. E., Sandquist, E. L., & Dubus, G. 2003, *ApJ*, 592, 1124
- Taam, R. E., & Spruit, H. C. 2001, *ApJ*, 561, 329
- Thomas, N. L., Naylor, T., & Norton, A. J. 2008, *A&A*, 483, 547
- Thorstensen, J. R., Peters, C. S., & Skinner, J. N. 2010, *ArXiv e-prints*
- Townsley, D. M., & Bildsten, L. 2002, *ApJ*, 565, L35
- . 2003, *ApJ*, 596, L227
- . 2004, *ApJ*, 600, 390
- . 2005, *ApJ*, 628, 395
- Townsley, D. M., & Gänsicke, B. T. 2009, *ApJ*, 693, 1007
- Uryu, K., & Eriguchi, Y. 1999, *MNRAS*, 303, 329
- Vaccaro, T. R., Rudkin, M., Kawka, A., Vennes, S., Oswalt, T. D., Silver, I., Wood, M., & Smith, J. A. 2007, *ApJ*, 661, 1112
- Verbunt, F. 1984, *MNRAS*, 209, 227
- Verbunt, F., & Zwaan, C. 1981, *A&A*, 100, L7
- Vida, K., Oláh, K., Kóvári, Z., Korhonen, H., Bartus, J., Hurta, Z., & Posztobányi, K. 2009, *A&A*, 504, 1021
- Vogt, N. 1990, *ApJ*, 356, 609
- Warner, B. 1987, *MNRAS*, 227, 23

- . 2006, *Astronomy and Geophysics*, 47, 010000
- Watson, C. A., Dhillon, V. S., & Shahbaz, T. 2006, *MNRAS*, 368, 637
- Watson, C. A., Steeghs, D., Dhillon, V. S., & Shahbaz, T. 2007a, *Astronomische Nachrichten*, 328, 813
- Watson, C. A., Steeghs, D., Shahbaz, T., & Dhillon, V. S. 2007b, *MNRAS*, 382, 1105
- Webb, N. A., Naylor, T., & Jeffries, R. D. 2002, *ApJ*, 568, L45
- Webbink, R. F. 1976, *ApJ*, 209, 829
- Webbink, R. F., & Wickramasinghe, D. T. 2002, *MNRAS*, 335, 1
- Weber, E. J., & Davis, Jr., L. 1967, *ApJ*, 148, 217
- Weight, A., Evans, A., Naylor, T., Wood, J. H., & Bode, M. F. 1994, *MNRAS*, 266, 761
- Willems, B., Kolb, U., Sandquist, E. L., Taam, R. E., & Dubus, G. 2005, *ApJ*, 635, 1263
- Wood, J. H., & Horne, K. 1990, *MNRAS*, 242, 606
- Wu, K., Wickramasinghe, D. T., & Warner, B. 1995a, *pasa*, 12, 60
- Wu, K., Wickramasinghe, D. T., & Warner, B. 1995b, in *Astrophysics and Space Science Library*, Vol. 205, *Cataclysmic Variables*, ed. A. Bianchini, M. della Valle, & M. Orio, 315–+
- Zangrilli, L., Tout, C. A., & Bianchini, A. 1997, *MNRAS*, 289, 59

Table 3
Binary and evolution parameters along the standard model track.

$M_1(M_\odot)$	$M_2(M_\odot)$	$P_{orb}(hr)$	$a(R_\odot)$	$\log J$	$\log \dot{J}_{sys}$	$\log \dot{J}_{GR}$	$\log \dot{J}_{CAML}$	$\log \dot{M}_2$	$\log \dot{P}_{orb}$	$\log t[yr]$
0.75	0.040	1.3939157	0.583	50.193	32.923	32.923	30.448	-11.077	1.648e-14	9.85600
0.75	0.045	1.3192333	0.563	50.235	33.080	33.080	30.690	-10.930	1.525e-14	9.82339
0.75	0.050	1.2695493	0.550	50.274	33.208	33.208	30.896	-10.806	1.447e-14	9.79791
0.75	0.055	1.2358468	0.542	50.311	33.316	33.316	31.067	-10.712	9.841e-15	9.77726
0.75	0.060	1.2211928	0.538	50.346	33.402	33.402	31.202	-10.646	2.183e-15	9.75937
0.75	0.062	1.2200589	0.539	50.360	33.431	33.431	31.250	-10.625	-6.433e-16	9.75271
0.75	0.065	1.2225936	0.540	50.380	33.469	33.469	31.314	-10.600	-5.749e-15	9.74308
0.75	0.070	1.2367626	0.545	50.413	33.520	33.520	31.409	-10.567	-1.279e-14	9.72770
0.75	0.075	1.2617622	0.554	50.445	33.558	33.558	31.486	-10.549	-2.019e-14	9.71273
0.75	0.080	1.2962487	0.565	50.476	33.585	33.585	31.553	-10.537	-2.545e-14	9.69775
0.75	0.085	1.3366576	0.578	50.506	33.605	33.605	31.614	-10.529	-2.889e-14	9.68260
0.75	0.090	1.3804350	0.591	50.535	33.620	33.620	31.673	-10.520	-3.043e-14	9.66719
0.75	0.095	1.4259075	0.606	50.562	33.632	33.632	31.724	-10.517	-3.259e-14	9.65147
0.75	0.100	1.4727480	0.620	50.588	33.642	33.642	31.775	-10.511	-3.313e-14	9.63535
0.75	0.110	1.5676297	0.649	50.637	33.658	33.658	31.869	-10.502	-3.359e-14	9.60172
0.75	0.120	1.6605382	0.677	50.681	33.672	33.672	31.954	-10.493	-3.373e-14	9.56611
0.75	0.130	1.7504148	0.704	50.722	33.685	33.685	32.035	-10.482	-3.293e-14	9.52822
0.75	0.140	1.8350365	0.729	50.759	33.698	33.698	32.116	-10.466	-3.117e-14	9.48793
0.75	0.150	1.9129707	0.752	50.794	33.713	33.713	32.190	-10.451	-3.072e-14	9.44525
0.75	0.160	1.9873895	0.774	50.826	33.727	33.727	32.258	-10.441	-3.189e-14	9.39957
0.75	0.170	2.0626921	0.797	50.856	33.739	33.739	32.319	-10.429	-3.135e-14	9.34963
0.75	0.180	2.1348046	0.818	50.884	33.751	33.751	32.380	-10.417	-3.123e-14	9.29493
0.75	0.190	2.2070274	0.840	50.911	33.761	33.761	32.426	-10.416	-3.427e-14	9.23373
0.75	0.200	2.2406366	0.851	50.934	33.787	33.787	32.745	-10.135	7.110e-14	9.17150
0.75	0.200	3.5314866	1.153	51.000	35.114	33.326	33.852	-9.091	-6.723e-13	8.23972
0.75	0.250	3.8602676	1.244	51.102	35.272	33.415	34.203	-8.915	-7.986e-13	8.08974
0.75	0.300	4.1508174	1.327	51.185	35.403	33.485	34.493	-8.768	-1.010e-12	7.94344
0.75	0.350	4.4040975	1.402	51.253	35.516	33.546	34.738	-8.643	-1.388e-12	7.79551
0.75	0.400	4.6501833	1.476	51.313	35.613	33.594	34.952	-8.522	-1.642e-12	7.63661
0.75	0.450	4.8819269	1.546	51.365	35.701	33.634	35.144	-8.412	-2.005e-12	7.45650
0.75	0.500	5.0929786	1.612	51.411	35.780	33.671	35.326	-8.306	-2.467e-12	7.23612
0.75	0.550	5.3192987	1.681	51.453	35.854	33.699	35.470	-8.219	-3.283e-12	6.90486
0.75	0.600	5.6150965	1.765	51.493	35.914	33.708	35.586	-8.167	-4.884e-12	5.00000

Note. — Unless otherwise stated, all physical quantities are given in cgs units. The sequence provided here is abbreviated. A more complete sequence sampled at higher resolution and providing additional information is available in electronic form.

Table 4
Binary and evolution parameters along the revised (optimal) model track.

$M_1(M_\odot)$	$M_2(M_\odot)$	$P_{orb}(hr)$	$a(R_\odot)$	$\log J$	$\log \dot{J}_{sys}$	$\log \dot{J}_{GR}$	$\log \dot{J}_{CAML}$	$\log \dot{M}_2$	$\log \dot{P}_{orb}$	$\log t[\text{yrs}]$
0.750	0.040	1.4987458	0.612	50.203	33.243	32.850	30.747	-10.789	2.635e-14	9.52767
0.750	0.045	1.4370365	0.596	50.248	33.386	32.993	30.981	-10.650	2.508e-14	9.49134
0.750	0.050	1.3951191	0.586	50.288	33.505	33.113	31.177	-10.539	2.039e-14	9.46222
0.750	0.055	1.3713966	0.581	50.326	33.604	33.211	31.339	-10.453	1.127e-14	9.43766
0.750	0.060	1.3627148	0.579	50.362	33.684	33.291	31.477	-10.386	4.699e-16	9.41603
0.750	0.061	1.3626145	0.580	50.369	33.698	33.305	31.501	-10.375	-1.791e-15	9.41196
0.750	0.065	1.3665367	0.582	50.396	33.749	33.356	31.594	-10.335	-1.084e-14	9.39629
0.750	0.070	1.3809809	0.587	50.429	33.801	33.408	31.693	-10.298	-2.326e-14	9.37770
0.750	0.075	1.4046595	0.595	50.461	33.842	33.449	31.779	-10.270	-3.400e-14	9.35972
0.750	0.080	1.4345706	0.604	50.491	33.875	33.482	31.857	-10.247	-4.201e-14	9.34208
0.750	0.085	1.4687294	0.615	50.520	33.902	33.509	31.927	-10.229	-4.845e-14	9.32457
0.750	0.090	1.5058189	0.627	50.547	33.924	33.532	31.992	-10.214	-5.410e-14	9.30707
0.750	0.095	1.5453577	0.639	50.574	33.943	33.551	32.052	-10.201	-5.801e-14	9.28941
0.750	0.100	1.5861744	0.651	50.599	33.960	33.567	32.108	-10.190	-6.135e-14	9.27154
0.750	0.110	1.6698073	0.677	50.646	33.987	33.594	32.211	-10.169	-6.470e-14	9.23484
0.750	0.120	1.7537710	0.702	50.689	34.010	33.617	32.304	-10.151	-6.673e-14	9.19654
0.750	0.130	1.8356292	0.726	50.729	34.030	33.637	32.391	-10.134	-6.739e-14	9.15630
0.750	0.140	1.9129674	0.749	50.766	34.049	33.656	32.475	-10.113	-6.533e-14	9.11396
0.750	0.150	1.9860910	0.771	50.799	34.068	33.675	32.552	-10.095	-6.588e-14	9.06922
0.750	0.160	2.0578237	0.793	50.831	34.085	33.692	32.618	-10.083	-6.962e-14	9.02130
0.750	0.170	2.1300629	0.814	50.861	34.099	33.706	32.684	-10.068	-6.916e-14	8.96904
0.750	0.180	2.1996207	0.835	50.889	34.113	33.720	32.747	-10.052	-6.840e-14	8.91176
0.750	0.190	2.2614846	0.853	50.914	34.129	33.736	32.828	-10.008	-4.677e-14	8.84910
0.750	0.200	2.2406366	0.851	50.934	34.180	33.787	33.160	-9.720	2.087e-13	8.79656
0.750	0.200	3.2511822	1.091	50.988	34.974	33.410	33.716	-9.218	-4.536e-13	8.38885
0.750	0.250	3.5602183	1.179	51.090	35.131	33.497	34.060	-9.048	-5.799e-13	8.24679
0.750	0.300	3.8453095	1.261	51.174	35.259	33.563	34.343	-8.907	-7.467e-13	8.10919
0.750	0.350	4.1104217	1.339	51.244	35.368	33.616	34.581	-8.789	-1.048e-12	7.97036
0.750	0.400	4.3833222	1.419	51.304	35.461	33.654	34.784	-8.681	-1.311e-12	7.82103
0.750	0.450	4.6675438	1.501	51.358	35.542	33.680	34.961	-8.589	-1.711e-12	7.64906
0.750	0.500	4.9503757	1.582	51.407	35.614	33.700	35.129	-8.498	-2.117e-12	7.43343
0.750	0.550	5.2504943	1.667	51.451	35.681	33.712	35.269	-8.419	-2.667e-12	7.10266
0.750	0.600	5.6066878	1.764	51.493	35.736	33.710	35.386	-8.366	-3.598e-12	5.00000

Note. — Unless otherwise stated, all physical quantities are given in cgs units. The sequence provided here is abbreviated. A more complete sequence sampled at higher resolution and providing additional information is available in electronic form.

Table 5
Physical and photometric donor properties along the standard model track.

$P_{orb}(hr)$	$M_2(M_\odot)$	$R_2(M_\odot)$	$T_{eff,2}(K)$	$\log g_2$	$\log L_2$	ζ_2	M_U	M_B	M_V	M_R	M_I	M_J	M_H	M_K	SpT
1.3939	0.0400	0.098	1091	5.054	28.68	-0.015	36.29	30.29	26.00	21.51	18.56	14.62	14.73	14.68	T
1.3192	0.0450	0.098	1306	5.104	28.99	0.044	33.24	27.87	24.91	20.67	17.73	13.81	13.80	13.66	T
1.2695	0.0500	0.099	1507	5.143	29.25	0.094	31.50	26.26	23.75	19.65	16.71	13.11	13.02	12.96	T
1.2358	0.0550	0.101	1702	5.173	29.47	0.168	30.23	25.14	22.61	18.73	15.96	12.63	12.42	12.32	T
1.2212	0.0600	0.103	1910	5.194	29.68	0.275	28.95	24.61	21.42	18.36	15.95	12.43	11.69	11.20	L0.3
1.2201	0.0620	0.104	1986	5.199	29.76	0.313	28.74	24.51	21.33	18.24	15.82	12.32	11.58	11.11	L0.1
1.2226	0.0650	0.105	2094	5.205	29.87	0.375	27.74	23.54	20.72	17.99	15.52	12.00	11.29	10.87	M9.7
1.2368	0.0700	0.109	2254	5.210	30.02	0.461	26.07	21.87	19.68	17.53	14.98	11.44	10.76	10.45	M9.1
1.2618	0.0750	0.113	2404	5.209	30.16	0.554	24.26	20.52	18.59	16.79	14.34	11.06	10.40	10.11	M8.0
1.2962	0.0800	0.117	2529	5.203	30.29	0.629	22.75	19.50	17.68	16.05	13.75	10.80	10.16	9.85	M7.2
1.3367	0.0850	0.122	2630	5.195	30.39	0.680	21.58	18.69	16.95	15.43	13.27	10.57	9.94	9.63	M6.8
1.3804	0.0900	0.127	2716	5.185	30.48	0.708	20.62	18.02	16.33	14.91	12.86	10.37	9.75	9.44	M6.6
1.4259	0.0950	0.132	2786	5.174	30.56	0.744	19.89	17.49	15.85	14.49	12.53	10.20	9.59	9.28	M6.3
1.4727	0.1000	0.137	2844	5.163	30.63	0.752	19.31	17.05	15.45	14.14	12.25	10.06	9.45	9.14	M6.1
1.5676	0.1100	0.148	2938	5.141	30.75	0.768	18.39	16.36	14.81	13.56	11.80	9.78	9.19	8.88	M5.8
1.6605	0.1200	0.158	3006	5.120	30.85	0.775	17.74	15.85	14.34	13.14	11.46	9.57	8.97	8.67	M5.5
1.7504	0.1300	0.168	3062	5.102	30.93	0.769	17.24	15.45	13.96	12.80	11.18	9.37	8.78	8.48	M5.2
1.8350	0.1400	0.178	3105	5.085	31.01	0.741	16.84	15.12	13.65	12.52	10.95	9.20	8.62	8.32	M5.0
1.9130	0.1500	0.187	3155	5.071	31.08	0.733	16.42	14.78	13.33	12.23	10.72	9.04	8.46	8.17	M4.8
1.9874	0.1600	0.196	3199	5.058	31.14	0.737	16.05	14.48	13.05	11.98	10.52	8.90	8.32	8.03	M4.5
2.0627	0.1700	0.205	3221	5.045	31.20	0.742	15.84	14.30	12.87	11.81	10.37	8.78	8.20	7.91	M4.4
2.1348	0.1800	0.214	3251	5.033	31.24	0.736	15.60	14.09	12.68	11.63	10.22	8.65	8.08	7.79	M4.3
2.2070	0.1900	0.223	3273	5.021	31.29	0.783	15.40	13.91	12.51	11.48	10.08	8.54	7.97	7.69	M4.1
2.2406	0.2000	0.229	3289	5.019	31.33	-0.177	15.27	13.79	12.40	11.38	9.99	8.47	7.90	7.61	M4.0
3.5315	0.2000	0.310	3296	4.756	31.59	0.636	14.48	13.09	11.76	10.74	9.35	7.80	7.22	6.94	M4.2
3.8603	0.2500	0.356	3373	4.734	31.75	0.618	13.90	12.54	11.23	10.24	8.91	7.42	6.84	6.57	M3.8
4.1508	0.3000	0.398	3428	4.715	31.88	0.609	13.47	12.12	10.83	9.87	8.56	7.12	6.54	6.28	M3.6
4.4041	0.3500	0.438	3491	4.699	31.99	0.623	13.06	11.73	10.45	9.51	8.24	6.85	6.27	6.02	M3.2
4.6502	0.4000	0.477	3548	4.683	32.10	0.636	12.72	11.38	10.11	9.20	7.96	6.61	6.03	5.79	M3.0
4.8819	0.4500	0.515	3614	4.668	32.19	0.655	12.39	11.04	9.78	8.88	7.69	6.38	5.79	5.57	M2.7
5.0930	0.5000	0.551	3690	4.654	32.29	0.650	12.07	10.71	9.44	8.57	7.43	6.17	5.57	5.36	M2.3
5.3193	0.5500	0.590	3784	4.636	32.39	0.739	11.74	10.34	9.07	8.22	7.15	5.94	5.31	5.13	M1.9
5.6151	0.6000	0.634	3899	4.612	32.51	0.855	11.38	9.92	8.66	7.84	6.84	5.68	5.04	4.89	M1.4

Note. — Unless otherwise stated, all physical quantities are given in cgs units. UBVR_I magnitudes are given on the Johnson-Cousins system (Bessell 1990), JHK are given on the CIT system (Elias et al. 1982b,a). The sequence provided here is abbreviated. A more complete sequence sampled at higher resolution and providing additional information is available in electronic form.

Table 6
Physical and photometric donor properties along the revised (optimal) model track.

$P_{orb}(hr)$	$M_2(M_\odot)$	$R_2(M_\odot)$	$T_{eff,2}(K)$	$\log g_2$	$\log L_2$	ζ_2	M_U	M_B	M_V	M_R	M_I	M_J	M_H	M_K	SpT
1.4987	0.0400	0.103	1321	5.012	29.05	0.063	32.89	27.54	24.68	20.46	17.51	13.66	13.62	13.47	T
1.4370	0.0450	0.104	1538	5.055	29.32	0.104	31.17	25.92	23.42	19.35	16.45	12.96	12.82	12.75	T
1.3951	0.0500	0.106	1738	5.088	29.55	0.158	30.26	25.44	22.48	18.94	16.35	12.79	12.23	11.88	T
1.3714	0.0550	0.108	1932	5.113	29.75	0.232	28.81	24.47	21.29	18.19	15.78	12.28	11.56	11.08	L0.0
1.3627	0.0600	0.110	2109	5.130	29.92	0.304	27.48	23.28	20.54	17.84	15.36	11.85	11.15	10.73	M9.6
1.3626	0.0610	0.111	2143	5.133	29.95	0.320	27.10	22.92	20.31	17.75	15.25	11.73	11.03	10.64	M9.5
1.3665	0.0650	0.113	2265	5.141	30.07	0.374	25.78	21.66	19.53	17.44	14.88	11.33	10.66	10.34	M9.2
1.3810	0.0700	0.117	2404	5.146	30.20	0.447	24.05	20.41	18.50	16.72	14.27	10.98	10.33	10.02	M8.1
1.4047	0.0750	0.121	2518	5.147	30.31	0.512	22.68	19.48	17.67	16.04	13.73	10.74	10.10	9.79	M7.3
1.4346	0.0800	0.125	2618	5.145	30.41	0.559	21.55	18.69	16.96	15.44	13.27	10.53	9.91	9.59	M6.9
1.4687	0.0850	0.130	2698	5.140	30.49	0.599	20.65	18.06	16.38	14.95	12.88	10.35	9.73	9.41	M6.6
1.5058	0.0900	0.135	2767	5.134	30.56	0.630	19.94	17.54	15.90	14.53	12.55	10.18	9.57	9.25	M6.4
1.5454	0.0950	0.139	2825	5.127	30.63	0.655	19.37	17.12	15.52	14.19	12.29	10.05	9.44	9.13	M6.2
1.5862	0.1000	0.144	2877	5.120	30.69	0.674	18.86	16.73	15.16	13.88	12.04	9.91	9.31	9.00	M6.0
1.6698	0.1100	0.154	2958	5.104	30.80	0.696	18.11	16.15	14.62	13.39	11.66	9.67	9.08	8.77	M5.7
1.7538	0.1200	0.164	3020	5.089	30.89	0.710	17.54	15.69	14.19	13.01	11.35	9.47	8.88	8.57	M5.4
1.8356	0.1300	0.173	3069	5.074	30.96	0.713	17.10	15.34	13.86	12.71	11.10	9.30	8.71	8.41	M5.2
1.9130	0.1400	0.183	3112	5.061	31.04	0.698	16.71	15.02	13.56	12.43	10.87	9.13	8.55	8.25	M5.0
1.9861	0.1500	0.192	3162	5.049	31.10	0.698	16.30	14.69	13.24	12.15	10.65	8.98	8.40	8.10	M4.7
2.0578	0.1600	0.201	3199	5.038	31.16	0.722	15.98	14.42	12.99	11.92	10.46	8.84	8.27	7.97	M4.5
2.1301	0.1700	0.209	3228	5.026	31.21	0.717	15.75	14.22	12.81	11.75	10.32	8.73	8.15	7.86	M4.4
2.1996	0.1800	0.218	3251	5.015	31.26	0.715	15.55	14.04	12.64	11.59	10.18	8.61	8.04	7.75	M4.3
2.2615	0.1900	0.226	3273	5.007	31.31	0.615	15.36	13.88	12.48	11.45	10.06	8.51	7.94	7.66	M4.1
2.2406	0.2000	0.229	3289	5.019	31.33	-0.240	15.27	13.79	12.40	11.38	9.99	8.47	7.90	7.61	M4.0
3.2512	0.2000	0.293	3296	4.804	31.55	0.620	14.62	13.22	11.87	10.85	9.47	7.92	7.35	7.06	M4.2
3.5602	0.2500	0.337	3373	4.781	31.70	0.629	14.03	12.66	11.34	10.35	9.02	7.54	6.96	6.69	M3.8
3.8453	0.3000	0.378	3428	4.759	31.83	0.636	13.58	12.23	10.93	9.97	8.67	7.23	6.66	6.40	M3.5
4.1104	0.3500	0.418	3491	4.739	31.95	0.660	13.16	11.83	10.54	9.60	8.34	6.95	6.38	6.13	M3.2
4.3833	0.4000	0.458	3548	4.718	32.06	0.700	12.81	11.47	10.19	9.28	8.05	6.70	6.12	5.88	M2.9
4.6675	0.4500	0.500	3614	4.694	32.17	0.749	12.45	11.10	9.83	8.94	7.75	6.45	5.86	5.64	M2.6
4.9504	0.5000	0.541	3690	4.670	32.27	0.762	12.11	10.75	9.48	8.61	7.47	6.21	5.61	5.40	M2.3
5.2505	0.5500	0.585	3793	4.643	32.39	0.839	11.74	10.33	9.07	8.22	7.15	5.95	5.32	5.15	M1.9
5.6067	0.6000	0.633	3908	4.612	32.51	0.930	11.36	9.90	8.64	7.82	6.83	5.68	5.03	4.88	M1.4

Note. — Unless otherwise stated, all physical quantities are given in cgs units. UBVR_I magnitudes are given on the Johnson-Cousins system (Bessell 1990), JHK are given on the CIT system (Elias et al. 1982b,a). The sequence provided here is abbreviated. A more complete sequence sampled at higher resolution and providing additional information is available in electronic form.

Table 7
White dwarf properties along the standard model track.

$P_{orb}(hr)$	$M_1(M_\odot)$	$R_1(10^8 \text{ cm})$	$\log g_1$	$\langle T_{eff,1}(K) \rangle$	$T_{eff,1,lo}(K)$	$T_{eff,1,hi}(K)$	$\langle \log L_1 \rangle$	M_U	M_B	M_V	M_R	M_I	M_J	M_H	M_K
1.3939	0.75	7.289	8.273	8132	7647	8647	30.22	12.96	13.63	13.37	13.20	12.99	12.90	12.72	12.76
1.3192	0.75	7.311	8.270	8852	8306	9434	30.37	12.57	13.26	13.03	12.91	12.75	12.73	12.59	12.64
1.2695	0.75	7.324	8.268	9517	8912	10162	30.50	12.27	12.96	12.75	12.66	12.55	12.59	12.48	12.55
1.2358	0.75	7.343	8.266	10064	9415	10758	30.60	12.06	12.74	12.55	12.49	12.40	12.49	12.40	12.48
1.2212	0.75	7.353	8.265	10464	9779	11197	30.66	11.91	12.59	12.40	12.37	12.31	12.43	12.34	12.43
1.2201	0.75	7.357	8.265	10594	9897	11341	30.69	11.87	12.55	12.36	12.34	12.28	12.40	12.33	12.42
1.2226	0.75	7.362	8.264	10751	10040	11514	30.71	11.82	12.50	12.32	12.29	12.24	12.38	12.31	12.40
1.2368	0.75	7.370	8.263	10966	10234	11751	30.75	11.76	12.44	12.26	12.24	12.20	12.35	12.29	12.37
1.2618	0.75	7.373	8.263	11085	10342	11882	30.77	11.72	12.41	12.23	12.21	12.18	12.33	12.28	12.36
1.2962	0.75	7.375	8.262	11165	10414	11971	30.78	11.70	12.38	12.21	12.20	12.16	12.32	12.27	12.36
1.3367	0.75	7.377	8.262	11219	10463	12030	30.79	11.68	12.37	12.19	12.19	12.15	12.31	12.27	12.35
1.3804	0.75	7.378	8.262	11280	10518	12097	30.80	11.67	12.35	12.18	12.17	12.14	12.31	12.26	12.35
1.4259	0.75	7.379	8.262	11300	10536	12120	30.80	11.66	12.35	12.17	12.17	12.14	12.30	12.26	12.35
1.4727	0.75	7.380	8.262	11341	10573	12165	30.81	11.65	12.33	12.16	12.16	12.14	12.30	12.26	12.34
1.6605	0.75	7.383	8.262	11459	10682	12293	30.83	11.61	12.30	12.13	12.14	12.12	12.28	12.24	12.33
1.7504	0.75	7.385	8.261	11528	10748	12364	30.84	11.59	12.28	12.11	12.12	12.11	12.28	12.24	12.33
1.8350	0.75	7.388	8.261	11628	10844	12469	30.85	11.57	12.26	12.09	12.11	12.09	12.27	12.23	12.32
1.9130	0.75	7.392	8.261	11723	10935	12567	30.87	11.55	12.24	12.07	12.09	12.08	12.26	12.22	12.31
1.9874	0.75	7.394	8.260	11786	10996	12634	30.88	11.53	12.23	12.06	12.08	12.07	12.25	12.21	12.31
2.0627	0.75	7.396	8.260	11863	11069	12714	30.89	11.51	12.21	12.05	12.06	12.06	12.24	12.20	12.30
2.1348	0.75	7.399	8.260	11940	11143	12794	30.90	11.49	12.19	12.03	12.05	12.05	12.24	12.20	12.29
2.2070	0.75	7.399	8.260	11947	11149	12801	30.90	11.49	12.19	12.03	12.05	12.05	12.24	12.20	12.29
2.2406	0.75	7.445	8.254	13908	13062	14808	31.17	11.14	11.86	11.75	11.82	11.86	12.09	12.07	12.17
3.5315	0.75	7.739	8.221	25581	23806	27487	32.26	9.37	10.46	10.62	10.74	10.89	11.28	11.32	11.43
3.6024	0.75	7.757	8.219	26182	24345	28158	32.30	9.29	10.40	10.57	10.69	10.84	11.23	11.28	11.39
3.8603	0.75	7.822	8.211	28579	26516	30802	32.46	9.01	10.18	10.37	10.50	10.66	11.07	11.13	11.25
4.1508	0.75	7.917	8.201	31342	29018	33853	32.63	8.74	9.94	10.16	10.30	10.47	10.89	10.95	11.08
4.4041	0.75	8.024	8.189	33935	31368	36712	32.78	8.51	9.74	9.99	10.13	10.30	10.73	10.80	10.92
4.6502	0.75	8.119	8.179	36632	33803	39697	32.93	8.32	9.58	9.84	9.98	10.16	10.60	10.67	10.79
4.8819	0.75	8.202	8.170	39294	36218	42631	33.06	8.18	9.45	9.72	9.87	10.05	10.50	10.56	10.69
5.0930	0.75	8.290	8.161	42041	38714	45654	33.18	8.06	9.34	9.62	9.77	9.95	10.40	10.46	10.59
5.3193	0.75	8.364	8.153	44370	40829	48218	33.29	7.96	9.25	9.54	9.69	9.87	10.32	10.39	10.52
5.6151	0.75	8.415	8.148	45843	42161	49846	33.35	7.91	9.20	9.49	9.64	9.82	10.28	10.35	10.47

Note. — Unless otherwise stated, all physical quantities are given in cgs units. The three effective temperatures listed correspond to the secular mean temperature ($\langle T_{eff,1} \rangle$) and the temperatures 5% ($T_{eff,1,lo}$) and 95% ($T_{eff,1,hi}$) through a given nova cycle. UBVRI magnitudes are given on the Johnson-Cousins system (Bessell 1990), JHK are given on the CIT system (Elias et al. 1982b,a). The sequence provided here is abbreviated. A more complete sequence sampled at higher resolution and providing additional information is available in electronic form.

Table 8
White dwarf properties along the revised (optimal) model track.

$P_{orb}(hr)$	$M_1(M_\odot)$	$R_1(10^8 \text{ cm})$	$\log g_1$	$< T_{eff,1}(K) >$	$T_{eff,1,lo}(K)$	$T_{eff,1,hi}(K)$	$< \log L_1 >$	M_U	M_B	M_V	M_R	M_I	M_J	M_H	M_K
1.4987	0.75	7.328	8.268	9613	9001	10267	30.51	12.23	12.92	12.72	12.63	12.52	12.57	12.46	12.54
1.4370	0.75	7.352	8.265	10440	9757	11170	30.66	11.92	12.60	12.41	12.38	12.31	12.43	12.35	12.44
1.3951	0.75	7.375	8.263	11152	10402	11956	30.78	11.70	12.39	12.21	12.20	12.17	12.32	12.27	12.36
1.3714	0.75	7.391	8.261	11710	10922	12554	30.86	11.55	12.24	12.08	12.09	12.08	12.26	12.22	12.31
1.3627	0.75	7.403	8.259	12140	11336	13001	30.93	11.45	12.15	12.00	12.02	12.03	12.22	12.18	12.28
1.3626	0.75	7.405	8.259	12210	11404	13073	30.94	11.44	12.14	11.99	12.01	12.02	12.21	12.18	12.27
1.3665	0.75	7.409	8.259	12470	11658	13340	30.98	11.39	12.10	11.94	11.98	11.99	12.19	12.16	12.25
1.3810	0.75	7.415	8.258	12716	11897	13592	31.01	11.34	12.05	11.91	11.95	11.97	12.18	12.15	12.24
1.4047	0.75	7.420	8.257	12912	12089	13791	31.04	11.31	12.02	11.88	11.93	11.95	12.17	12.14	12.23
1.4346	0.75	7.424	8.257	13075	12249	13956	31.06	11.29	12.00	11.86	11.91	11.93	12.15	12.13	12.22
1.4687	0.75	7.426	8.257	13204	12376	14086	31.08	11.26	11.98	11.85	11.90	11.92	12.14	12.12	12.21
1.5058	0.75	7.428	8.256	13312	12483	14196	31.09	11.24	11.96	11.83	11.88	11.91	12.13	12.11	12.20
1.5454	0.75	7.430	8.256	13407	12576	14292	31.10	11.23	11.94	11.82	11.87	11.91	12.13	12.11	12.20
1.5862	0.75	7.431	8.256	13489	12656	14377	31.11	11.21	11.93	11.81	11.86	11.90	12.12	12.10	12.19
1.6698	0.75	7.436	8.255	13647	12809	14540	31.14	11.18	11.91	11.79	11.85	11.89	12.11	12.09	12.18
1.7538	0.75	7.441	8.255	13785	12943	14681	31.15	11.16	11.88	11.77	11.83	11.87	12.10	12.08	12.17
1.8356	0.75	7.445	8.254	13915	13070	14816	31.17	11.13	11.86	11.75	11.82	11.86	12.09	12.07	12.16
1.9130	0.75	7.450	8.254	14079	13228	14984	31.19	11.10	11.84	11.73	11.80	11.84	12.07	12.06	12.15
1.9861	0.75	7.454	8.253	14220	13365	15130	31.21	11.08	11.81	11.71	11.78	11.83	12.06	12.05	12.14
2.0578	0.75	7.457	8.253	14315	13455	15229	31.22	11.06	11.80	11.70	11.77	11.82	12.05	12.04	12.13
2.1301	0.75	7.460	8.253	14433	13569	15353	31.24	11.03	11.78	11.68	11.76	11.81	12.05	12.03	12.13
2.1996	0.75	7.463	8.252	14561	13691	15487	31.25	11.01	11.76	11.66	11.74	11.79	12.04	12.03	12.12
2.2615	0.75	7.469	8.252	14918	14032	15861	31.29	10.94	11.70	11.62	11.70	11.76	12.01	12.00	12.09
2.2406	0.75	7.533	8.244	17532	16488	18644	31.58	10.46	11.33	11.33	11.43	11.52	11.81	11.82	11.92
3.2512	0.75	7.691	8.226	23669	22078	25375	32.12	9.60	10.65	10.77	10.89	11.03	11.40	11.43	11.54
3.5602	0.75	7.759	8.218	26281	24434	28269	32.31	9.28	10.39	10.56	10.68	10.84	11.23	11.27	11.39
3.8453	0.75	7.826	8.211	28723	26648	30961	32.47	9.00	10.16	10.36	10.49	10.65	11.06	11.12	11.24
4.1104	0.75	7.899	8.203	30926	28640	33395	32.61	8.77	9.97	10.19	10.33	10.49	10.92	10.98	11.11
4.3833	0.75	7.991	8.193	33126	30636	35818	32.74	8.58	9.80	10.04	10.18	10.35	10.78	10.85	10.97
4.6675	0.75	8.070	8.184	35116	32435	38019	32.85	8.41	9.65	9.91	10.05	10.22	10.67	10.73	10.86
4.9504	0.75	8.137	8.177	37191	34308	40316	32.96	8.29	9.55	9.82	9.96	10.13	10.58	10.64	10.77
5.2505	0.75	8.197	8.171	39118	36059	42438	33.05	8.19	9.46	9.73	9.88	10.06	10.50	10.57	10.69
5.6067	0.75	8.239	8.166	40464	37281	43918	33.11	8.12	9.40	9.67	9.82	10.00	10.45	10.51	10.64

Note. — Unless otherwise stated, all physical quantities are given in cgs units. The three effective temperatures listed correspond to the secular mean temperature ($< T_{eff,1} >$) and the temperatures 5% ($T_{eff,1,lo}$) and 95% ($T_{eff,1,hi}$) through a given nova cycle. UBVRI magnitudes are given on the Johnson-Cousins system (Bessell 1990), JHK are given on the CIT system (Elias et al. 1982b,a). The sequence provided here is abbreviated. A more complete sequence sampled at higher resolution and providing additional information is available in electronic form.

Table 9

Mean offsets between observed absolute near-IR magnitudes of CVs with trigonometric parallaxes and predicted absolute magnitudes for CV donors (see Figure 17). The dispersions around the predictions after applying these offsets are also given.

Prediction	ΔJ	σ_J	ΔH	σ_H	ΔK	σ_K
Broken-power-law donor sequence	1.61	1.34	1.36	1.22	1.26	1.15
Standard Model	1.65	1.47	1.39	1.35	1.30	1.27
Revised Model	1.63	1.38	1.37	1.27	1.27	1.19

Table 10

Statistics of the approximate period distributions shown in Figure 20. The absolute numbers quoted are for a uniform space density of $2 \times 10^{-5} \text{ pc}^{-3}$ within 100 pc.

CV Type	Standard Model	Revised Model
Numbers within 100 pc		
Active CVs	72.80	80.58
Inactive CVs in the Period Gap	11.98	3.19
Pre-Bounce Short-Period Systems	34.97	16.39
Long-Period CVs	1.46	2.05
All Pre-Bounce CVs	36.43	18.44
All Post-Bounce CVs	36.37	62.14
Percentages within the intrinsic active population		
Long-Period CVs	2.00	2.55
Pre-Bounce Short-Period CVs	48.04	20.34
Period Bouncers	49.96	77.12

APPENDIX

A. A COMPENDIUM OF MAGNETIC BRAKING RECIPES

Here, we present an overview of some of the most widely-used MB prescriptions. Note that this is not meant to be a comprehensive exploration of all AML mechanisms, or even all MB formulations, that have been proposed. In particular, we will not consider any mechanism unrelated to MB due to stellar winds, such as circumbinary disks (Taam & Spruit 2001; Dubus et al. 2002; Taam et al. 2003; Willems et al. 2005), accretion disk winds (Cannizzo & Pudritz 1988; Livio & Pringle 1994), or frictional drag associated with nova eruptions (Schenker et al. 1998).³¹ We have also not yet included some of the most recent MB recipes in the literature, such as those developed in Irwin et al. (2007) and Barnes & Kim (2010). The particular MB prescriptions we do consider were selected mainly on the basis that they have proven themselves to be popular (particularly in the CV literature) and/or are flexible (i.e. include easily tuneable free parameters that permit a convenient exploration of the viable parameter space).

A.1. *Verbunt & Zwaan (1981)*

In a hugely influential paper, Verbunt & Zwaan (1981, hereafter VZ81) pointed out that a simple extrapolation of the observed spin-down rates of solar-type stars due to MB implied an AML rate far in excess of \dot{J}_{GR} for CVs and low-mass X-ray binaries (LMXBs). The VZ81 formulation of MB has been widely used in theoretical studies of CV evolution, and it is instructive to consider its derivation.

VZ81 begin with the empirical observation due to Skumanich (1972) that the equatorial rotation speed of slowly spinning ($v_{eq,2} \lesssim 100 \text{ km s}^{-1}$) G-type MS stars declines with age, t , as

$$v_{eq,2} = 10^{14} f t^{-1/2} \text{ cm s}^{-1}, \quad (\text{A1})$$

where $f = 0.73$ according to Skumanich (1972), and $f = 1.78$ according to Smith (1979). Here and below, we retain the subscript “2” to emphasize that, in the CV setting, the stars whose properties we are considering are the secondaries. The spin angular momentum of the star can be written as

$$J_2 = I_2 \Omega = k_2^2 M_2 R_2^2 \Omega, \quad (\text{A2})$$

where I_2 is the moment of inertia of the star, k_2 is its radius of gyration ($k^2 \simeq 0.1$ for low-mass stars, although in detail it varies slightly with the stellar properties), and $\Omega = 2\pi/P_{orb}$ is the angular velocity (where we have already assumed perfect synchronization, i.e. $P_{spin,2} = P_{orb}$). Since we can also write $\Omega = v_{eq,2}/R_2$, we have

$$J_2 = k_2^2 M_2 R_2 v_{eq,2} = 10^{14} f k_2^2 M_2 R_2 t^{-1/2}. \quad (\text{A3})$$

Differentiating this with respect to t (keeping all other variables fixed) yields

$$\dot{J}_2 = -5 \times 10^{13} f k_2^2 M_2 R_2 t^{-3/2}. \quad (\text{A4})$$

The substitution

$$t^{-3/2} = \left(\frac{v_{eq,2}}{10^{14} f} \right)^3 = \left(\frac{\Omega R_2}{10^{14} f} \right)^3 \quad (\text{A5})$$

then leads to the familiar expression for the VZ81 MB law,

$$\dot{J}_{VZ} = -5 \times 10^{-29} k_2^2 f^{-2} M_2 R_2^4 \Omega^3, \quad (\text{A6})$$

where we have changed the subscript to “VZ” to allow comparison with other prescriptions later on.

We have presented the derivation of this MB recipe in some detail here in order to expose the weakness of its foundations. The key point – which was already made by Patterson (1984) – is the fact that Equation A1 was derived exclusively from observations of *slowly rotating G-type stars*. Adopting it without change for CV secondaries, which, in the period range we are mainly interested in, are extremely fast rotating M-type stars, is clearly fraught with uncertainties. In particular, even if the time dependence of Equation A1 were universal, it seems likely that its normalization would depend on the stellar properties (e.g. M_2 and R_2). In this case the braking rate would still scale as Ω^3 , but its dependence on the stellar properties could be very different. In a CV setting, this means the entire prescription is highly uncertain. After all, for a Roche-lobe-filling CV secondary, M_2 , R_2 and Ω are connected via the period-density relation (Equation 12). Thus any one of these three parameters can always be eliminated in favour of the other two.

None of this is intended as a criticism of VZ81. For their purpose of demonstrating the relevance of MB as an AML mechanism in CVs and LMXBs, the order-of-magnitude approach they adopted is entirely appropriate. Our point here is simply that neither the normalization nor the functional form of Equation A6 can be regarded as well-established.

³¹ Note that all of these alternatives are, in fact, examples of CAML (King & Kolb 1995).

A.2. *Rappaport, Verbunt & Joss (1983)*

Rappaport et al. (1983, hereafter RVJ83) carried out one of the first detailed investigations of MB-driven CV evolution. Realizing the uncertainties emphasized in the last section, they chose to parameterize the AML rate due to MB as

$$\dot{J}_{MB} = \dot{J}_{VZ} \left(\frac{R_2}{R_\odot} \right)^{\gamma-4}. \quad (\text{A7})$$

For $\gamma = 4$, this reduces to the VZ81 formulation. Other choices provide a convenient way to assess how the shape and strength of the MB law affects CV evolution. RVJ83 considered the range $0 \leq \gamma \leq 4$ and noted that varying γ within this range had rather dramatic effects on the resulting binary evolution.

A.3. *Kawaler (1988)*

A more physically motivated MB model was constructed by Kawaler (1988, hereafter K88), building on earlier theoretical work by Mestel (1968), Weber & Davis (1967) and others. Kawaler’s main contribution was to derive an approximate expression for the braking torque exerted by a stellar wind in which the key uncertainties and parameter dependencies are parameterized in a convenient way.

The AML rate in all MB models can be calculated by assuming perfect co-rotation of the wind out to the Alfvén radius, R_A (Mestel & Spruit 1987). In general, R_A can be a function of polar angle, but in the Kawaler model it is assumed to be spherical, so that

$$\dot{J}_{Kaw} = \frac{2}{3} \dot{M}_w R_2^2 \Omega \left[\left(\frac{R_A}{R_2} \right)_{radial} \right]^{n_k} \quad (\text{A8})$$

where \dot{M}_w is the mass-loss rate in the stellar wind, and R_A is to be evaluated for a purely radial field geometry. The power-law index n_k allows different field geometries to be considered, with $n_k = 2$ being a purely radial field, and $n_k = 3/7$ a purely dipolar one.

In order to determine $(R_A/R_2)_{radial}$, K88 assumes that the magnetic field of the star scales as

$$\left(\frac{B_2}{B_\odot} \right) = K_B \left(\frac{R_2}{R_\odot} \right)^{-2} \Omega^{a_k}. \quad (\text{A9})$$

Most applications of this formalism have focused on the case $a_k = 1$ (based on an observational suggestion by Linsky & Saar (1987)), for which K88 adopts $K_B^2 \simeq 4.4 \times 10^{11} \text{g cm}^{-1}$.

The final expression for the AML loss rate in the K88 picture is

$$\dot{J}_{Kaw} = -K_W \Omega^{1+4a_k n_k/3} \dot{M}_{w,14}^{1-2n_k/3} \left(\frac{R_2}{R_\odot} \right)^{2-n_k} \left(\frac{M_2}{M_\odot} \right)^{-n_k/3}, \quad (\text{A10})$$

where $\dot{M}_{w,14} = \dot{M}_w / (10^{-14} \text{M}_\odot \text{yr}^{-1})$ and

$$K_W = 2.035 \times 10^{33} \left(24.93 K_V^{-1/2} \right)^{n_k} K_B^{4n_k/3}, \quad (\text{A11})$$

with K_V defined as the ratio of the wind speed at the Alfvén radius to the escape speed there. In practice, K88 sets $K_v = 1$. In this formulation of MB, the Skumanich relation is recovered for $n_k = 1.5$ (assuming $a_k = 1$), since this yields the required $\dot{J} \propto \Omega^3$.

A.4. *Mestel & Spruit (1987)*

One of the main advantages of the K88 formulation is that it provides a convenient parameterization for the dependence of the braking rate on the magnetic field geometry inside R_A (via the parameter n_k). However, the way in which this dependence was calculated is highly approximate. For example, a predominantly dipolar field structure inside R_A implies the existence of closed field lines near the equatorial plane that cannot contribute to MB. Moreover, the size of this “dead zone” will itself depend on key parameters such as the magnetic field strength and the rotation rate. These effects cannot be captured in single-zone outflow descriptions like the K88 model.

In an attempt to overcome these limitations, Mestel & Spruit (1987, hereafter MS87) constructed a model in which the “wind zone” and “dead zone” are both treated explicitly and simultaneously. The dead zone in this picture is inside the Alfvén surface and its equatorial extent, R_d , is calculated self-consistently. The magnetic field structure is then taken to be dipolar inside a radius R_d and radial beyond this. The AML rate produced by the stellar wind in this picture is again found by assuming co-rotation out to the Alfvén surface. Allowing for an angular dependence of R_A , this yields

$$\dot{J}_{MB} = -4\pi\Omega \int_0^{\pi/2} (\rho_A v_A R_A^2) (R_A \sin \theta)^2 \sin \theta d\theta, \quad (\text{A12})$$

where ρ_A , v_A and R_A are the wind density, velocity and radius at the Alfvén surface, and θ is the polar angle ($\theta = \pi/2$ corresponds to the equatorial plane). In the MS87 scenario, this can be rewritten as (their Equation 16)

$$\dot{J}_{MS} = -4\pi\Omega \int_0^1 \rho_d v_d R_d^2 R_A^2 (1 - \mu^2) d\mu, \quad (\text{A13})$$

where ρ_d , v_d , and R_d now denote the density, velocity and radius in the wind zone, but now evaluated at $R = R_d$. The actual values of R_A and R_d can be calculated via two implicit equations (Eqs 8 and 14 in MS87).

We will not develop this derivation further here or repeat the implicit equations for R_A and R_d ; for details, the reader is referred to MS87 as well as Hameury et al. (1988); McDermott & Taam (1989); Li (1999); Ivanova & Taam (2003).³² However, two key points regarding the way in which \dot{J}_{MS} is actually calculated will be important to our discussion below. First, in order to calculate \dot{J}_{MS} , the density at the base of the wind, ρ_0 , and the magnetic field strength of the star, B_2 , are needed (this is partly because the implicit equations for R_A and R_d depend on these quantities). We follow the notation of Hameury et al. (1988) and parameterize ρ_0 as

$$\frac{\rho_0}{\rho_{0,\odot}} = \left(\frac{\Omega}{\Omega_\odot} \right)^{n_{ms}} \quad (\text{A14})$$

and B_2 as

$$\frac{B_2}{B_\odot} = \left(\frac{\Omega}{\Omega_\odot} \right)^{p_{ms}}. \quad (\text{A15})$$

Virtually all applications of the MS87 model take $p_{ms} = 1$, but different values for the power-law index n_{ms} are sometimes considered (typically $0.5 \leq n_{ms} \leq 2$).³³ Second, in evaluating \dot{J}_{MS} , several approximations are commonly made. In particular, the angular dependence of R_A is usually ignored, the equatorial value being used for all angles. As explained in MS87, this formally yields a lower limit on the AML rate, but one that should be quite close to the correct answer. We will return to this issue below in Section A.6.

A.5. Andronov et al. (2003)

One potential problem with AML prescriptions that scale as Ω^3 is that they are unable to explain the observed spin-down rates of young stars in clusters. In particular, prescriptions in which \dot{J} depends so steeply on Ω predict that rapid rotators are braked extremely efficiently and should therefore not be observed. By contrast, very rapidly rotating stars have been found in many open clusters (e.g. Stauffer & Hartmann 1987). In order to explain these observations, Sills et al. (2000) modified the K88 prescription in a way that makes the dependence of \dot{J} on Ω much shallower at high rotation rates. Andronov et al. (2003, hereafter APS03) then pointed out that adopting this modified prescription would have a significant impact on CV evolution.

The Sills et al. (2000) MB recipe that was adopted by APS03 is given by

$$\dot{J}_{APS} = -K_w \left(\frac{R_2}{R_\odot} \right) \left(\frac{M_\odot}{M_2} \right) \begin{cases} \Omega^3 & \text{for } \Omega \leq \Omega_{crit} \\ \Omega \Omega_{crit}^2 & \text{for } \Omega > \Omega_{crit} \end{cases}. \quad (\text{A16})$$

Here, $K_w = 2.7 \times 10^{47} \text{ g cm}^2 \text{ s}$, and we have intentionally used the same symbol for this normalization factor as for that in the K88 prescription. This is because, in the limit $\Omega < \Omega_{crit}$, the APS03 prescription reduces to the default K88 MB law ($a_K = 1$, $n_K = 1.5$, $\dot{M}_{w,14} = 1$ and $K_V = 1$). In principle, the critical angular velocity Ω_{crit} depends on the stellar properties, but this is irrelevant for CV donors, since they all spin well above Ω_{crit} .

As we shall see, the APS03 braking law produces extremely low braking rates. These would not suffice to drive donors significantly out of thermal equilibrium above the period gap and, if correct, would thus require a fundamental revision of CV evolution theory. It is therefore worth noting that Barnes (2003, 2007) has suggested a different interpretation for the open cluster rotation data. In Barnes's picture, all stars above the fully convective boundary eventually settle on a $\dot{J} \propto \Omega^3$ spin-down sequence (which Barnes dubs the "I-sequence"), consistent with the Skumanich (1972) relationship. However, stars do not reach this sequence at a fixed time, so that the fastest rotators in a given young cluster will always be those object that have not yet settled on the I-sequence.

A.6. Ivanova & Taam (2003)

The last MB prescription we will consider is that due to Ivanova & Taam (2003, hereafter IT03). Taking the MS87 model as their starting point, their goal was to identify an optimal value for n_{ms} ³⁴ by assuming that the X-ray luminosity of the star, $L_{x,2}$, is generated by the dead zone and then requiring that the dependence of $L_{x,2}$ on Ω should

³² However, note that, as pointed out by McDermott & Taam (1989) and Li (1999), the numerical coefficient given in MS87 for the quantity χl_d (1.45×10^{-4} ; their Equation 12) is incorrect and should instead read 1.1×10^{-4} . As a result, the numerical constant 7.25×10^{-5} appearing in Equation 4 of Hameury et al. (1988) is also incorrect and should read 5.5×10^{-5} .

³³ In order to avoid confusion, we note that MS87 use the power law index n differently in their paper.

³⁴ Note that IT03 use the symbol p for this (not to be confused with our definition of p_{ms} in Section A.4).

match the observations. The specific dependence they aimed to reproduce was $L_{x,2} \propto \Omega^2$ at low $\Omega/\Omega_\odot \lesssim 2 - 12$ and $L_{x,2} \propto \Omega^0$ for higher rotation speeds (Pizzolato et al. 2003). According to their calculations, this behaviour could be matched within the MS87 framework by taking $n_{ms} \simeq 0.6$.

Crucially, IT03 found that the dependence of \dot{J}_{MS} on Ω turns over at fast rotation speeds, becoming substantially flatter than the roughly $\dot{J} \propto \Omega^3$ Skumanich-like relation they obtained at low rotation speeds. In fact, they obtained this behaviour for essentially *all* values of n_{ms} in the range $0 < n_{ms} < 1$. This is somewhat surprising at first sight, since neither MS87, nor Hameury et al. (1988), nor McDermott & Taam (1989), nor we found such a flattening in their implementations of the MS87 picture. On the other hand, Keppens et al. (1995) also found a flattening in \dot{J} with Ω in their implementation of a Weber-Davis magnetic wind model (from $\dot{J} \propto \Omega^3$ at low rotation rates to $\Omega^3 \propto \Omega^2$ at high rates). Moreover, Natasha Ivanova (private communication) has suggested to us that the discrepancy between MS87 and IT03 may reflect different ways of estimating conditions at the Alfvén surface (specifically whether one connects them to the physical parameters within the dead zone or at the stellar surface). Pursuing this is beyond the scope of the present paper.

For our purposes here, it is possible to avoid this issue completely by simply considering the analytical approximation for \dot{J} suggested by IT03. This is

$$\dot{J}_{IT} = -K_j \left(\frac{R_2}{R_\odot} \right)^4 \begin{cases} \left(\frac{\Omega}{\Omega_\odot} \right)^3 & \text{for } \Omega \leq \Omega_x \\ \frac{\Omega^{1.3} \Omega_x^{1.7}}{\Omega_\odot^3} & \text{for } \Omega > \Omega_x \end{cases} \quad (\text{A17})$$

where $K_j = 6 \times 10^{30} \text{ g cm}^2 \text{ s}^{-2}$, and we have followed Ivanova & Kalogera (2006) in dropping the scaling with coronal temperature in the formula given by IT03. This is a good approximation, since the coronal temperature is otherwise approximated by the virial temperature, which scales as $M_2 R_2^{-1}$ and is therefore almost constant along the lower MS. As with the APS03 prescription, in principle Ω_x depends on the stellar properties, but in practice all CV donors fall into the fast rotation regime, $\Omega > \Omega_x$.

B. A COMPILATION OF MASSES AND RADII FOR NON-INTERACTING LOW-MASS STARS

The starting point for our compilation was Table 1 in López-Morales (2007) and Figure 13 in Vida et al. (2009). These data sets were then further updated with several new and improved measurements taken from the recent literature. Following López-Morales (2007), we include both isolated stars and objects found in detached binary systems. Our full data base of masses and radii for non-interacting low-mass stars is listed in Table B1.

Table B1
Mass and radius measurements for non-interacting low-mass stars.

Name	$M(M_\odot)$	$\sigma_M(M_\odot)$	$R(R_\odot)$	$\sigma_R(R_\odot)$	Type ^a	Reference ^b	Comments ^c
GJ 15 A	0.4040	0.0404	0.379	0.006	S	1	
GJ 514	0.5260	0.0526	0.611	0.043	S	1	
GJ 526	0.5020	0.0502	0.493	0.033	S	1	
GJ 687	0.4010	0.0401	0.492	0.038	S	1	
GJ 752 A	0.4840	0.0484	0.526	0.032	S	1	
GJ 880	0.5860	0.0586	0.689	0.044	S	1	
GJ 205	0.631	0.031	0.702	0.063	S	1	
GJ 191	0.281	0.014	0.291	0.025	S	1	
GJ 699	0.158	0.008	0.196	0.008	S	1	
GJ 411	0.403	0.020	0.393	0.008	S	1	
GJ 380	0.670	0.033	0.605	0.020	S	1	
GJ 105 A	0.790	0.039	0.708	0.050	S	1	
YY Gem A	0.5992	0.0047	0.6191	0.0057	B	1	
YY Gem B	0.5992	0.0047	0.6191	0.0057	B	1	
CU Cnc A	0.4333	0.0017	0.4317	0.0052	B	1	
CU Cnc B	0.3980	0.0014	0.3908	0.0094	B	1	
GU Boo A	0.610	0.007	0.623	0.016	B	1	
GU Boo B	0.599	0.006	0.620	0.020	B	1	
BW3 V38 A	0.44	0.07	0.51	0.04	B	1	
BW3 V38 B	0.41	0.09	0.44	0.06	B	1	
TrES-Her0-07621 A	0.493	0.003	0.453	0.060	B	1	
TrES-Her0-07621 B	0.489	0.003	0.452	0.050	B	1	
2MASS J05162881+2607387 A	0.787	0.012	0.788	0.015	B	1	
2MASS J05162881+2607387 B	0.770	0.009	0.817	0.010	B	1	
2MASS J04463285+1901432 A	0.47	0.05	0.57	0.02	B	1	(i)
2MASS J04463285+1901432 B	0.19	0.02	0.21	0.01	B	1	(i)
UNSW-TR-2 A	0.529	0.035	0.641	0.05	B	1	
UNSW-TR-2 B	0.512	0.035	0.608	0.06	B	1	
V818 Tau B	0.7605	0.0062	0.768	0.010	B	1	
FL Lyr B	0.960	0.012	0.962	0.028	B	1	
V1061 Cyg Ab	0.9315	0.0068	0.974	0.020	B	1	
V1061 Cyg B	0.925	0.036	0.870	0.087	B	1	

Table B1 — *Continued*

Name	$M(M_{\odot})$	$\sigma_M(M_{\odot})$	$R(R_{\odot})$	$\sigma_R(R_{\odot})$	Type ^a	Reference ^b	Comments ^c
RW Lac B	0.870	0.004	0.964	0.004	B	1	
HS Aur B	0.879	0.017	0.873	0.024	B	1	
OGLE-TR-5 B	0.271	0.035	0.263	0.012	B	1	
OGLE-TR-6 B	0.359	0.025	0.393	0.018	B	1	
OGLE-TR-7 B	0.281	0.029	0.282	0.013	B	1	
OGLE-TR-18 B	0.387	0.049	0.39	0.04	B	1	
OGLE-TR-34 B	0.509	0.038	0.435	0.033	B	1	
OGLE-TR-78 B	0.243	0.015	0.24	0.013	B	1	
OGLE-TR-106 B	0.116	0.021	0.181	0.013	B	1	
OGLE-TR-120 B	0.47	0.04	0.42	0.02	B	1	
OGLE-TR-122 B	0.092	0.009	0.120	0.019	B	1	
OGLE-TR-125 B	0.209	0.033	0.211	0.027	B	1	
SDSS-MEB-1 A	0.272	0.020	0.268	0.010	B	2	
SDSS-MEB-1 B	0.240	0.022	0.248	0.0090	B	2	
NSVS01031772 A	0.5428	0.0027	0.5260	0.0028	B	3	
NSVS01031772 B	0.4982	0.0025	0.5088	0.0030	B	3	
T-Lyr1-17236 A	0.6795	0.0107	0.634	0.043	B	4	
T-Lyr1-17236 B	0.5226	0.0061	0.525	0.052	B	4	
V405 And A	0.49	0.05	0.78	0.02	B	5	(ii)
V405 And B	0.21	0.04	0.24	0.04	B	5	(ii)
2MASS J0154 A	0.66	0.03	0.64	0.08	B	6	
2MASS J0154 B	0.62	0.03	0.61	0.09	B	6	
BD -22 5866 Aa	0.5881	0.029	0.614	0.045	B	7	
BD -22 5866 Ab	0.5881	0.029	0.614	0.045	B	7	
LP-133-373 A	0.340	0.014	0.33	0.02	B	8	
LP-133-373 B	0.340	0.014	0.33	0.02	B	8	
NSVS-02502726 A	0.714	0.019	0.645	0.006	B	9	
NSVS-02502726 B	0.347	0.012	0.501	0.005	B	9	
V471 Tau B	0.93	0.07	0.96	0.04	W	10	
RXJ2130	0.555	0.023	0.534	0.017	W	11	
RR Cae B	0.1825	0.0139	0.209	0.0143	W	12	(iii)
EC 13471	0.43	0.04	0.42	0.02	W	13	(iv)
NN Ser B	0.111	0.004	0.141	0.002	W	14	(v)
RXJ0239.1 A	0.73	0.009	0.741	0.004	B	15	
RXJ0239.1 B	0.693	0.006	0.703	0.002	B	15	
GJ166A	0.877	0.044	0.770	0.021	S	16	
GJ570A	0.802	0.040	0.739	0.019	S	16	
GJ845	0.762	0.038	0.732	0.006	S	16	
GJ879	0.725	0.036	0.629	0.051	S	16	
GJ887	0.503	0.025	0.459	0.011	S	16	
GJ551	0.123	0.006	0.141	0.007	S	16	
2MASSJ0746	0.085	0.010	0.078	0.010	B	17	
HIP96515 Aa	0.59	0.03	0.64	0.01	B	18	
HIP96515 Ab	0.54	0.03	0.55	0.03	B	18	
CMDra A	0.2310	0.0009	0.2534	0.0019	B	19	
CM Dra B	0.2141	0.0010	0.2396	0.0015	B	19	(vi)
T-TR-205-013 B	0.124	0.010	0.167	0.006	B	20	
RXJ1547 A	0.2576	0.0085	0.2895	0.0068	B	21	(vii)
RXJ1547 B	0.2585	0.0080	0.2895	0.0068	B	21	(vii)
IM Vir A	0.981	0.012	1.061	0.016	B	22	
IM Vir B	0.6644	0.0048	0.681	0.013	B	22	

^a (S) = single star or star in very wide binary; (W) star in close binary with white dwarf companion; (B) star in other type of binary

^b (1) López-Morales (2007); (2) Blake et al. (2008); (3) Lopez-Morales et al. (2006); (4) Devor et al. (2008); (5) Vida et al. (2009); (6) Becker et al. (2008); (7) Shkolnik et al. (2008); (8) Vaccaro et al. (2007); (9) Çakırlı et al. (2009); (10) O'Brien et al. (2001); (11) Maxted et al. (2004); (12) Maxted et al. (2007); (13) O'Donoghue et al. (2003); (14) Parsons et al. (2010); (15) López-Morales & Shaw (2007); (16) Demory et al. (2009); (17) Berger et al. (2009); (18) Huéamo et al. (2009); (19) Morales et al. (2009b); (20) Beatty et al. (2007); (21) Hartman et al. (2009); (22) Morales et al. (2009a)

^c (i) This object is a member of a 150 Myr cluster; (ii) Mass errors estimated from Fig. 13 in Vida et al. (2009); (iii) The mass and radius given in the table correspond to the mid-points of the model-dependent parameter ranges quoted in Maxted et al. (2007); the half-range associated with the model uncertainties has been added in quadrature to the quoted formal errors; (iv) This object may be the secondary of a hibernating CV (O'Donoghue et al. 2003); we have not attempted to correct the radius for tidal/rotational deformation; (v) The radius listed in the table has been corrected for irradiation-driven bloating, as described by Parsons et al. (2010; also see Section 5.2.3); (vi) CM Dra may be a Population II object; (vii) Since the mass ratio estimated from the radial velocity curve of this binary was $q = 1.00 \pm 0.02$, Hartman et al. (2009) assumed equal radii for both binary component in obtaining their final parameter estimates.